Topics in TeV-Scale Phenomenology

David Krohn

A Dissertation
Presented to the Faculty
of Princeton University
in Candidacy for the Degree
of Doctor of Philosophy

Recommended for Acceptance
by the Department of
Physics
Adviser: Lian-Tao Wang

September 2010

Abstract

With the LHC turning on, the Tevatron running better than ever, and dark matter direct detection experiments pushing to ever higher sensitivities, we are on the cusp of a new era in particle physics. Over the next decade, these experiments will likely discover the mechanism responsible for electroweak symmetry breaking, and may well uncover the identity of particle dark matter.

This thesis addresses some topics in the phenomenology of TeV-scale physics which we may hope to probe at these experiments. Chapter 1 serves an an introduction, reviewing physics at this scale and motivating phenomenologists' excitement and expectations. Chapter 2 discusses ways to incorporate dark matter particles into a particular model of electroweak symmetry breaking, making sure that they remains stable against anomalous decays. Chapter 3 discusses an interesting class of dark matter models which would leave a striking signal at direct detection experiments. Chapter 4 discusses a new collider based probe of electroweak symmetry breaking, designed to look for models that approximate the Standard Model at the electroweak scale, but which deviate from it at higher energies. Chapter 5 discusses another collider based measurement, this one designed to measure the polarized tops one expects from the decay of certain new-physics states. Finally, chapters 6 and 7 present two new jet algorithms, useful for interpreting messy collider data and looking for signals of new physics. Chapter 8 contains the conclusions.

Acknowledgements

First, I would like to thank my adviser, Lian-Tao Wang, for introducing me to the methods and ideas of particle physics phenomenology. I'm fortunate he has a sense of humor.

Much of what I learned in graduate school was taught to be by my collaborators: Adam Falkowski, Jiji Fan, Tao Han, Pablo Mosteiro, Lisa Randall, Josh Ruderman, Jessie Shelton, Arun Thalapillil, Jesse Thaler, Itay Yavin, and Wenhan Zhu. I've benefited greatly from our work together. Itay in particular was very helpful: by sharing his office with me and patiently answering my many questions, he helped me to get my research going.

Over the years I've been lucky to interact with many talented physicists. I am grateful for the conversations I've had with Nima Arkani-Hamed, Frank Calaprice, Norman Christ, Janet Conrad, Cristiano Galbiati, Luca Grandi, Steve Gubser, Can Kilic, Igor Klebanov, Phuan Ong, Frans Pretorius, Matt Reece, Gavin Salam, Matthew Schwartz, Chris Tully, and Herman Verlinde. Surely there are others who should be on this list - I apologize to those I forgot to name.

Of course, without my fellow students, too many to name, life at Princeton wouldn't have been the same. I leave with colorful memories of health notebooks, hygiene inspectors, and thunderstorms on Corno Grande.

Finally, I'd like to thank my parents and sister for their support and encouragement, and Phyllis for making life more interesting.

To Pliny the Elder.

It is astonishing to what an extent the weakness of the mind will proceed, urged on by a little success...to give full scope to its impudence!

That harmonical proportion, which compels nature to be always consistent with itself...makes the earth one ninety-sixth part of the whole universe.

-Pliny the Elder, *The Natural History* [1]

Relation to Previously Published Work

Chapter 2 comes from ref. [2], chapter 4 from selections of ref. [3], chapter 5 from ref. [4], chapter 6 from ref. [5], and chapter 7 comes from ref. [6]. Chapter 3 is derived from work in progress with J. Ruderman and L.-T. Wang.

Contents

Chapter 1

Introduction

The Standard Model (SM) of particle physics was first proposed and analyzed over 40 years ago [7, 8, 9, 10, 11, 12]. Since that time, much progress has been made in better understanding how it works and measuring its parameters. However, aside from the discovery of non-zero neutrino masses [13], we have seen no conclusive signs that nature deviates from the model. Thus, we are left in an unsatisfactory situation: experimental evidence confirms the SM over and over again, but we still have yet to produce and measure the Higgs particle, which provides much of the plumbing necessary to keep the SM self-consistent, and we have little understanding of particle dark matter (DM), which we believe comprises over 20% of the observable universe. Moreover, the SM possesses certain theoretical traits which modern field theory tells are are less than desirable (e.g. fine tuning).

Fortunately, we are on the verge of a new era of discovery in particle physics. Many new experiments are coming online which can probe the SM at unprecedented energies, and look with incredible precision for the signatures of new particles. Over the next decade we can expect to discover the SM Higgs (or probe whatever else does its job), and it seems likely that we will detect or severely constrain particle dark matter. This thesis presents several results results in particle physics phenomenology relevant to this exciting era. In this introduction we will first review the SM and motivate some of its extensions, discuss the various tasks of the phenomenologist (building models, proposing measurements), and describe how the research presented here makes progress along these lines.

1.1 The Standard Model and its Extensions

Just about all of the experimental data in particle physics (except for the neutrino masses) can be explained within the context of the SM [14]. While there remain various anomalies, usually at the 3σ significance level, there has been no smoking gun signal of new physics. This is surprising, both because of the SM's simplicity, and because it does not address modern theoretical concerns.

The SM calls for three generations of leptons and quarks assigned an anomaly free set of charges under an $\mathrm{SU}(3) \times \mathrm{SU}(2) \times \mathrm{U}(1)$ gauge group. In addition, it posits an $\mathrm{SU}(2) \times \mathrm{U}(1)$ complex scalar doublet, the Higgs doublet H, whose potential induces it to acquire a symmetry breaking VEV. This simple setup is able to correctly describe phenomena at energies separated by many orders of magnitude.

However, many physicists are uncomfortable with the current state of affairs. The main problem is that the SM Higgs is supposed to be a fundamental scalar. Because of this, no symmetry of the theory protects the Higgs mass from loop corrections (see Fig. 1.1) cutoff by the Plank scale. Naively, these corrections are much larger than the tree-level mass assigned to the Higgs in the SM. Therefore, if the SM is really correct, then the parameters of the theory must be tuned against each other with an incredible, seemingly unnatural, precision. This concern is known as the hierarchy problem. The search for its resolution drives much of the current research in TeV-scale particle physics[1].

---

[1] Of course, the SM presents us with many other unresolved questions (the hierarchy of Yukawa couplings, the strong CP problem, etc.), but the hierarchy problem provides a strong enough moti-

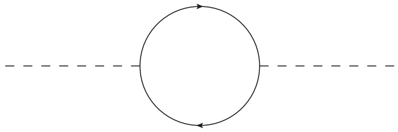

Figure 1.1: A loop correction to the SM Higgs mass.

Many solutions have been put forth which solve the hierarchy problem, with varying degrees of success. Supersymmetry [15] supposes there is a symmetry between fermions and bosons, so the chiral symmetry which protects the mass of fermions in turn protects the mass of the Higgs. Other theories suggest the Higgs mass is stable at the electroweak scale because it is the pseudo-Goldstone boson of an approximate symmetry [16, 17, 18]. Some theories even remove the Higgs altogether, breaking SU(2) × U(1) with the condensate of strongly interacting fields, in analogy to the chiral symmetry breaking of QCD [19, 20]. This is not a comprehensive list (other scenarios of electroweak symmetry breaking are discussed later in the text), and already most of the theories here have run into tension with experimental data[2]. The point one should take away is simply that most considerations of naturalness hint that the SM picture of electroweak symmetry breaking is not the full story, and most attempts to construct a more appealing theory require new physics states near the TeV scale.

Now, understanding the nature of electroweak symmetry breaking would on its own be sufficient motivation for studying physics near the TeV scale. However, we have reason to believe DM also has a mass at, or slightly above, the electroweak scale, making things even more interesting. To see why, one starts with the assumption that early on in the universe DM was in thermal equilibrium with SM fields and

---

vation by itself, so it will be our focus here.

[2] The tension between new models of electroweak symmetry breaking, which usually require states near the TeV-scale, and precision data, which excludes most new states below ~ 10 TeV, is known as the little hierarchy problem [21, 22].

the various particle species could annihilate into each other. As the universe cooled and expanded, DM continued to annihilate into SM species (with the reverse process eventually kinematically forbidden) until its density became so low that annihilation essentially stopped and the DM number density became fixed. Solving the Boltzman equations in detail for this process tells one that the product of DM's annihilation cross section and its velocity is roughly

$$\langle \sigma v \rangle \sim \mathcal{O}(10^{-9}\ \mathrm{GeV}^{-2}) \tag{1.1}$$

where

$$\langle \sigma v \rangle \approx \frac{|\mathcal{M}|^2}{32\pi m_\chi^2} \tag{1.2}$$

for m_χ the mass of the DM particle and $\mathcal{M}$ the matrix element of its dominant annihilation channel. Remarkably, from Eq. (1.2) one finds that if DM is weakly coupled then it naturally lives near the electroweak/TeV scale. This is the so called WIMP miracle. It provides a strong hint that DM is somehow tied up with electroweak symmetry breaking, and deepens the mystery of physics at the TeV-scale.

1.2 The Role of the Phenomenologist

Now, the greatest difficulty confronting science in understanding physics at the TeV scale is clearly experimental. The Tevatron, LHC, and the many DM direct detection experiments are marvels of ingenuity. They do the hard work. However, experimental data must be interpreted and synthesized to wring out the signs of new physics. This is the responsibility the phenomenologist.

In general, phenomenology adopts a two-pronged bottom-up approach to understanding physics. Part of the time phenomenologists make models, conjuring up new particles and couplings either because they make a model more palatable, or because they help explain a new signal (and, sometimes, they do both). The rest of the time phenomenologists propose experimental measurements which could lead to signs of new physics. These might, for instance, take the form of selection cuts to isolate interesting events at colliders, or they might entail looking for specific recoil spectra at direct detection experiments.

With the LHC already collecting data, the Tevatron driving the SM Higgs into ever smaller mass windows, satellite experiments reporting excesses, and DM direct detection experiments excluding a growing region of parameter space, we are entering a era which will require phenomenologists muster all the aforementioned skills. It promises to be a lot of fun.

1.3 Overview of Research Presented in this Thesis

The research presented in this thesis touches upon many of the topics presented in the preceding pages. To reiterate, the main concerns of particle physics at the TeV scale include understanding the nature of electroweak symmetry breaking (i.e. finding the Higgs or whatever else does its job), and discovering particle dark matter. The principle responsibilities of the phenomenologist include model building and proposing experimental measurements.

The research presented here begins, in chapter 2, with a study on embedding DM in a particular model of electroweak symmetry breaking. The model at hand is a *little Higgs* [23, 24] model. These models basically take the idea of a pseudo-Goldstone Higgs, but they use a special symmetry-breaking group structure to push any new physics states to the $\sim$ 10 TeV scale, so there is less conflict with precision data. Many realizations of the little Higgs mechanism rely on what is basically a scaled up version of QCD: just as QCD confines to break the approximate $\mathrm{SU}(3) \times \mathrm{SU}(3)$ symmetry of the light quarks, these little Higgs models use a new set of fermions charged under a strong gauge group whose confinement breaks part of the symmetry of the theory. Now, it was realized that the group structure of some little Higgs models contains an unbroken $\mathbb{Z}_2$ symmetry, and that fields odd under this party are naively stable against decays. Thus they would be natural candidates for particle DM. However, one must be careful because the symmetries of this theory are realized through the transformations of fermion fields, and while fermions may exhibit a symmetry *classically*, the symmetry can be broken *quantum mechanically*. Indeed, at a classical level QCD has a parity, but it is broken by quantum effects[3]. If quantum effects break the $\mathbb{Z}_2$ symmetry of a little Higgs theory then states odd under that symmetry will no loner be stable against decays and can no longer be considered candidates for DM. Chapter 2 studies under what circumstances little Higgs theories constructed out of strongly coupled fermions can be endowed with a $\mathbb{Z}_2$ parity *unbroken* by quantum effects, allowing them to accommodate a DM candidate.

Chapter 3 also focuses on DM models, but with an eye toward new recoil spectra which could show up at direct detection experiments. To understand why this is interesting, it is useful to consider recent efforts in DM model building. As discussed in Sec. 1.1, we have good reason to believe DM is weakly coupled and has a mass at the electroweak/TeV-scale. Turning DM annihilation diagrams on their side, one finds that they describe the elastic scattering of DM off of ordinary SM matter. This is the motivation for using sensitive direct detection measurements to search for DM, and has been the standard paradigm for ~ 30 years. However, over the last 5 to 10 years, various experimental hints from direct detection experiments have suggested that this scenario is too naive. These anomalies can be explained if one supposes DM scatters inelastically [25, 26], transitioning to a different state as it collides with SM particles. Furthermore, satellite data hints that DM couples preferentially to light leptons, suggesting it decays/annihilates through a GeV-scale dark-sector [27, 28].

---

[3] These effects give rise to, for instance, the $\pi_0 \rightarrow \gamma\gamma$ decay.

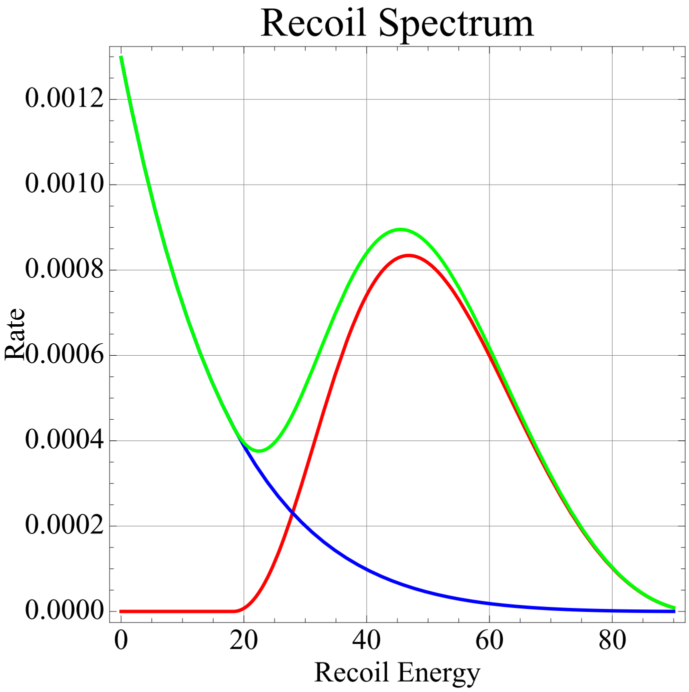

Figure 1.2: Sample DM direct detection recoil spectrum showing elastic scattering (blue), inelastic scattering (red), and a combination of the two (green).

Remarkably, the mass splittings between DM states in this scenario are at just the scale ($\sim$ 100 keV) one would expect if the splittings came from the dynamics of a GeV-scale hidden sector. In these scenarios DM's recoil spectrum becomes modified, turning on only at a finite recoil energy, rather than exhibiting scattering at all energies (contrast the red and blue curves of Fig. 1.2). Now, most of these inelastic DM theories focus on scattering mediated by GeV-scale states, simply assigning DM a TeV-scale tree-level mass. Yet, given that they are at the same scale, one suspects that the mass scale of electroweak symmetry breaking is non-trivially related to the DM mass. In chapter 3 we discuss a class of models which makes this connection, using the VEV of a scalar to set the mass scale in the Higgs sector, and for DM. Remarkably, we find that in such a scenario the elastic scattering rate can be comparable to the inelastic rate, yielding a distinct recoil spectrum (see the green curve of Fig. 1.2) visible at the next generation of direct detection experiments.

Chapter 4 switches gears from dark matter and focuses more on electroweak symmetry breaking. The motivation for the research presented in this chapter is the observation that all the constraints from precision data hint that we will discover a particle which looks very much like the SM Higgs. Now, the particle we find at the LHC/Tevatron may not be the SM Higgs. It could, for instance, be a composite state from dynamics above the TeV scale. However, should we discover such a particle and measure its quantum numbers and couplings, they would probably be very close to those of the SM Higgs, and given the messy environment of the LHC it would be difficult for physicists to claim they have seen unambiguous signs of phenomena beyond the SM based on, say, a 20% discrepancy in a particular Higgs decay channel. This is a problem, because without any additional handle we would have to wait for experiments to directly produce new physics states, and these could be out of the reach of our most powerful colliders. Chapter 4 proposes a new measurement designed to detect new phenomena from beyond the SM physics which could subtly alter the couplings of the Higgs to gauge bosons. In particular, we propose measuring the shape of the angular distribution calculated from the decay products of gauge bosons produced in vector boson fusion. Because it measures a shape, rather than a rate, this measurement is not susceptible to the large experimental uncertainties which normally accompany the measurement of Higgs couplings. Unless we see more obvious signs of new physics, this sort of measurement might our best shot at understanding electroweak symmetry breaking using collider data.

Chapter 5 continues along these lines, proposing another collider measurement relevant to the investigation of electroweak symmetry breaking. Here the starting point is the top quark. In most new-physics models of electroweak symmetry breaking the top quark is accorded special treatment. This makes intuitive sense: the top has a large $\mathcal{O}(1)$ coupling to the SM Higgs, so models which somehow replace the Higgs usually include large couplings between the top and the new-physics states which take its place. Furthermore, new-physics models often come with chiral couplings, so exotic new states might preferentially couple to tops of a particular handedness. Now, the top is special for another reason aside from its prominent role in physics beyond the SM: because the top is so heavy it has a very short lifetime, and it decays before hadronization can wash away information about its handedness. By measuring the top decay products one can recover information about a top's handedness, and in turn infer its coupling to new physics. Chapter 5 proposes such a collider-based measurement focusing on the very energetic tops we expect from the decay of heavy new physics states.

Finally, chapters 6 and 7 discuss a more general tool useful in collider physics: the jet algorithm. To appreciate the utility of jet algorithms, it is important to understand that what one observes in a collider, and how this is used to extract physical parameters. Most of the time physicists calculate scattering amplitudes between a small, finite number of particles (e.g. $gg \to gg$). While, in principle, one could keep going to higher multiplicities, these become suppressed by higher powers of the coupling constant, and are eventually negligible. However, a subtlety arises when one considers higher particle multiplicities where additional states are taken to be collinear with existing states and/or soft. In this scenario, there is no longer a systematic suppression of the amplitudes for diagrams at higher multiplicities. Physically, this means that the amplitude one calculates in, for instance, a $2 \to 2$ process, is roughly correct as long as one takes a blurred view of the final state, grouping collinear and soft particles together to approximate the two final states one can calculate. These groups of particles are known as *jets*. In practice, the grouping procedure mentioned above can be quite complicated. Often it is unclear how radiation should be summed in a detector, and which final states should be associated with which finite parton configurations. Jet algorithms provide a systematic, well defined, grouping procedure, allowing one to compare measured data to calculation and partially mitigate these uncertainties.

Chapter 6 presents one such algorithm designed to exploit the hierarchy of scales in an event to better group the measured radiation into jets. The basic idea behind the algorithm presented in this chapter is that in a hard scattering event the radiation emitted by final state particles tends to be much harder (i.e. it has a higher transverse energy) than the radiation emitted from the initial states and from other, softer collisions happening at the same time in the detector. While most jet algorithms cluster using an angular measure to group radiation, this algorithm also tries to reduce the soft radiation contaminating a jet by removing the parts of a jet which seems to come from physics at a lower energy scale.

Chapter 7 takes another, complementary, approach to improving jet clustering. As will be discussed in the chapter, most jet algorithms cluster radiation by angular distances, measured in a coordinate system designed to account for the fact that the center of mass of the hard scattering is not fixed at a hardon collider. While such a coordinate system is necessary to ensure measurements do not reflect the initial conditions of the scattering, they make it difficult to select the appropriate angular size of a jet. The algorithm presented in this chapter attempts to choose the appropriate angular size of each jet more judiciously, based on the kinematics of the event at hand. Through a more accurate choice of jet size the algorithm is able to improve jet reconstruction, and extend the reach of hadron colliders in uncovering new physics.

Chapter 2

Anomalies in Fermionic UV Completions of Little Higgs Models

We consider fermionic UV completions of little Higgs models and their associated T-parity-violating anomalous vertices. In particular, we investigate strategies to avoid such parity-violating anomalies. We show that it is unlikely a QCD-like UV completion could be used to implement a model with anomaly-free global symmetry groups. This is because the vacuum state is unlikely to achieve the necessary alignment. However, we will see that certain multi-link moose models, although anomalous, possess a modified form of T-parity that leads to a stable particle. Finally, we briefly discuss a discriminant for detecting anomalous decays at colliders.

2.1 Introduction

Little Higgs [23] theories are accorded pride of place among composite models of electroweak (EW) symmetry breaking. These models solve the 'little' hierarchy problem and are not immediately ruled out by precision EW measurements. Continuous advances in model building [29, 30] have given rise to a parity (T-parity, analogous to R-parity in SUSY) that helps little Higgs theories better satisfy precision EW data by excluding many dangerous tree level interactions. Another welcome consequence of such a parity is the presence of a stable dark matter candidate in the spectrum, the lightest T-odd particle (LTP). A recent set of papers [31, 32] have shown that quantum anomalies violate T-parity by the inclusion of Wess-Zumino-Witten [33, 34] terms in the full lagrangian. While these terms are suppressed, and therefore do not introduce problems with precision data, they render the LTP unstable. One may wonder how generic this instability is in little Higgs models. Is it possible to find UV completions of little Higgs models where the stability of the LTP is not spoiled by anomaly terms? In this short paper we consider several possible means of achieving this.

In section 2.2 we investigate the conditions under which WZW anomalies may be completely removed from a little Higgs theory. The quantized nature of the WZW term leads one to hope that through some discrete choice of model parameters this can be achieved. We begin with models based on anomaly-free global symmetries. Here we find that in QCD-like UV completions of such models the condensing fermions cannot achieve the desired symmetry breaking pattern due to problems of vacuum alignment. In addition, we consider moose models and their WZW terms for distinct choices of link direction. We find that these models will always have anomalous terms, although these may possess a parity.

The parity of anomalous terms in multi-link moose models is the focus of section 2.3. Here we discuss the parity of WZW terms as a relabeling symmetry of the UV theory. We consider this parity in the context of a Minimal Moose [35] like model and show that it can lead to a stable LTP.

Finally, in our appendix we discuss a simple way by which the anomalous vertices can be distinguished at the Large Hadron Collider (LHC). Here we also summarize some results relevant to computing WZW vertices.

2.2 The problem with T-parity

Hill and Hill [31, 32] recently pointed out that T-parity is violated in little Higgs theories by WZW terms [33, 34]. They convincingly show that such terms will be present in most little Higgs theories discussed in the literature if one imagines a QCD-like UV completion. In what follows, we explore how general this conclusion is and what sort of structures may give rise to a theory free of WZW terms.

2.2.1 Linear UV completions

The most straightforward way to avoid anomalous vertices in a coset model is to UV complete the theory into a linear sigma model of fundamental scalars. WZW vertices arise because of anomalies from condensing fermions; remove the fermions and you remove the anomalies. However, such an approach reintroduces the hierarchy problem composite Higgs theories were created to solve. It is possible to avoid this problem by utilizing a supersymmetric linear sigma model as detailed in Ref. [36]

2.2.2 Anomaly free groups

Another way to avoid WZW terms is to consider a little Higgs theory with global symmetries that are manifestly anomaly free. Indeed, models based on the $SO(N)$ and $Sp(N)$ groups have been developed [37, 38], some of which have tree level T-parity, and a fermionic UV completion of one such model has been carried out [39]. While it is possible to use fermions to implement the UV global symmetry of these theories, whether or not the vacuum will realize the IR coset remains a question of vacuum alignment. *In what follows we aim to convince the reader that with a QCD-like theory the vacuum will not align itself into the necessary pattern.*

For simplicity, consider the coset space $SO_L(N) \times SO_R(N)/SO_D(N)$. The global symmetry of this group is anomaly free; if one could realize this symmetry with fermions then T-parity would not be foiled by anomalies. Here the $L \times R$ structure is needed in order to implement a form of T-parity exchanging $L \leftrightarrow R$. A QCD-like UV completion of this model (shown in Fig. 2.1) would consist of quarks transforming as a fundamental and an anti-fundamental, respectively, under some strong gauge group (we take all the fermions to be left-handed Weyl fermions and use the L/R-subscripts to designate their position in the moose diagram). As specified, this setup will have a larger global symmetry than we desire: $SU_L(N) \times SU_R(N)$. One can try to amend the situation by introducing Majorana masses,

$$\mathcal{L} \supset \psi_L^T M^{(L)} \psi_L + \psi_R^T M^{(R)} \psi_R \tag{2.1}$$

where $M^{(L,R)}$ are proportional to the identity in flavor space (we suppress flavor indices to avoid clatter).

Figure 2.1: A simple-minded attempt to produce a chiral lagrangian with the coset $SO_L(N) \times SO_R(N)/SO_D(N)$ from a fermionic QCD-like theory is unlikely to succeed.

We would like the condensate to be $\langle \psi_L \psi_R^T \rangle \propto \mathbf{1}$ so as to break the global symmetry to the diagonal subgroup. The low energy theory is then described as usual in terms of the pion fields $U = \exp(2i\pi)$ which span the coset space. Under the global symmetries U transforms like $U \to LUR^\dagger$, as dictated by the structure of the condensate. We need to choose $M^{(L,R)} \sim \Lambda_S$ so that $SU(N)$ is strongly broken. Treating the $M^{(L,R)}$ as a set of spurions transforming as

$$M^{(L)} \to L^* M^{(L)} L^\dagger, \; M^{(R)} \to R M^{(R)} R^T \tag{2.2}$$

we see that the only mass term we can write down for the chiral lagrangian is

$$\mathcal{L}_{mass} = Tr\left(UM^{(R)}U^TM^{(L)}\right) \tag{2.3}$$

which indeed gives mass to all the pions associated with the $SU(N)$, but not the $SO(N)$ generators. Raising the mass terms, $M_{ij}^{(L,R)} \to \infty$ we decouple all the unwanted goldstones and are left with an $SO_L(N) \times SO_R(N)/SO_D(N)$ coset space.

However, there is something wrong with this picture. As $M^{(L,R)} \to \infty$ all the underlying quarks become heavy and decouple, so how is it that we still have any goldstones left? This is in odds with the persistent mass conjecture [40]: very heavy fermions cannot form a massless goldstone boson. The resolution to this apparent contradiction is that *we are dealing with the wrong goldstones because we have chosen the wrong symmetry breaking pattern.* To see this note that the condensate $\langle\psi_L\psi_R^T\rangle \neq 0$ is not the only way the vacuum can align itself. The confining strong group must be such that it allows for $\langle\psi_L\psi_L^T\rangle \neq 0$ and $\langle\psi_R\psi_R^T\rangle \neq 0$. If this were not the case we would not be able to write the Majorana mass terms to begin with. This new configuration is the correct alignment. The low energy theory then contains two pions fields $U_{L,R} = exp(2i\pi_{L,R})$ each spanning the coset $SU(N)/SO(N)$. It is possible to write a mass term for each independently,

$$\mathcal{L}_{mass} = Tr\left(U_LM^{(L)} + M^{(L)}U_L^T\right) \quad + \quad L \to R \tag{2.4}$$

The paradox is now resolved. As $M^{(L,R)} \to \infty$ our pions decouple; none are left in the spectrum. Therefore, adding Majorana masses will not get us the desired symmetry breaking pattern. Indeed, by continuity, this argument seems to imply that the addition of even a small Majorana mass term will misalign the vacuum (although the existence of a phase transition is possible).

Having put the idea of using fermion masses to achieve the desired symmetry to rest, one could consider trying to enforce an $SO(N)$ global symmetry by adding scalars with a Yukawa coupling to the confining quarks: $y\psi_L^T h\psi_L$ [1]. The Yukawa coupling, y must be very large or else we are only softly breaking the global $SU(N)$ symmetry. Unfortunately, such a setup seems problematic as well. If the scalar's mass is much heavier than Λ_S, we should integrate it out and generate a 4-fermion operator. This, however, will be suppressed and hence constitute only a soft breaking term. Keeping the scalar mass lighter than Λ_S will require fine-tuning because of the large Yukawa. This solution will not work without additional ingredients.

Alternatively (or in some sense, equivalently), we can consider 4-fermion operators,

$$\mathcal{L} \supset \frac{y^2}{M^2}\psi_L^T\psi_L\bar{\psi}_L^T\bar{\psi}_L \quad + \quad L \to R \tag{2.5}$$

Such terms possess a chiral symmetry which forbids fermion masses and the correct alignment of the vacuum seems more plausible. Once again unless we fine-tune $M \sim \Lambda_S$, this term will only lead to a soft breaking of $SU(N)$. However, in analogy with walking technicolor[41], one can imagine a strongly interacting theory which gives rise to large anomalous dimensions for such 4-fermion operators. In that case, the breaking of the global $SU(N)$ can be strong without any fine-tuning.

Both of the solutions proposed in the last two paragraphs (a finely tuned scalar or a strong theory with operators of large anomalous dimension) seem difficult to implement in standard QCD-like theories, and to the best of the authors' knowledge no realistic examples of these mechanisms are known. However, if one considers *supersymmetric* QCD-like theories, then the situation is considerably more hopeful. Indeed, one can then naturally stabilize the scalar or, alternatively, have operators with large anomalous dimensions (such as the gauge duals of fermions in the bulk of AdS). It may be interesting to construct an explicit example of such a theory.

---

[1] The scalar can also be charged under the strong group. In that case, the strong group could also be $SU(N)$.

Although we have not proven a no-go theorem, we hope we have convinced the reader of the following: it seems unlikely that a *natural, non-supersymmetric* strongly coupled theory can give rise to a chiral lagrangian with a coset space of $SO_L(N) \times SO_R(N)/SO_D(N)$. Similar considerations apply to any other global group with only real representations, e.g. $Sp(N)$ groups. A counterexample to this conclusion would constitute a very welcome addition to the model builder toolkit.

2.2.3 Anomalies in Moose Models

In light of the preceding discussion, to consider fermionic UV completions it seems natural to work with SU(N) moose models. If we ignore problems with the Higgs quartic coupling [42], such moose theories are easy to UV complete[2]. Each link becomes two Weyl fermions condensing at a high scale. If we construct these models with identical strong groups for each link, the only freedom we have in is in selecting the representation of the condensing fermions (N vs. $\bar{N}$), which in turn determines the direction of the link fields. This freedom can be used to cancel gauge anomalies, and one might hope that such arrow adjustments are sufficient to avoid the anomalies violating T-parity. However, because the WZW terms are sensitive to the global symmetries of a theory they cannot be removed through a choice of link direction.

Let us begin by by considering the action of T-parity on a moose model. In a

---

[2] The problem of generating a large quartic coupling in such theories is by no means simple. In [42], the author cogently argues that one will not generate a sufficiently large quartic in theories based on deconstruction. The solution offered in [43] relies on having large number of sites and the authors find that the EW scale is parametrically $v^2 \sim f^2/N^2$, where $f \sim 1$ TeV is the "pion" decay constant and N^2 is the total number of sites (two extra dimensions). However, this scaling is essentially the same (albeit in one additional extra dimension) as the one worked out in the original little Higgs paper [23]. In such constructions, with d extra dimensions, the EW scale is given by $v^2 \sim f^2/N^d$. Therefore, adding extra dimensions does not help much because parametrically $v^2 \sim f^2/(\text{total \# of sites})$ and in realistic models the number of sites is $\sim \mathcal{O}(1)$. Other ways of generating a large quartic include large Yukawa coupling to matter [35] or integrating out a heavy scalar with cubic coupling to the higgs [44].

coset space with the structure G/H, and Lie algebras defined as

$$\text{Lie}(H) = h,\ \text{Lie}(G) = h + k, \tag{2.6}$$

a theory with WZW terms over a symmetric space (one where the commutator of two elements in k lies in h) can be split into parity eigenstates as detailed in [45]. This parity is defined as the transformation,

$$\pi \to -\pi,\ A_h \to A_h,\ A_k \to -A_k \tag{2.7}$$

Moreover, in models where $G = \text{SU}(N) \times \text{SU}(N)$, all WZW terms have negative parity under this transformation [45]. We can therefore say that this parity takes

$$\mathcal{L}_{\text{WZW}}(\pi, A_h, A_k) \to -\mathcal{L}_{\text{WZW}}(\pi, A_h, A_k) \tag{2.8}$$

Now, for illustration purposes, consider an SU(3) moose model such as the one considered in ref. [35] but with only two links for simplicity. This is shown in Fig. 2.2. We gauge the SU(2) × U(1) subgroup of each SU(3) where SU(2) sits in the upper-left hand corner and U(1) corresponds to the T_8 generator. We can schematically write the Lagrangian for this [3] as

$$\mathcal{L} \sim \mathcal{L}_{\text{kin}}(\pi_1, A) + \mathcal{L}_{\text{kin}}(\pi_2, A) + \mathcal{L}_{\text{WZW}}(\pi_1, A) + \mathcal{L}_{\text{WZW}}(\pi_2, A) \tag{2.9}$$

where $\pi_{1,2}$ are the pions associated with the two links and A are the gauge fields, $A_{L,R}$

---

[3] The relative sign between the WZW terms is crucial. It can be derived by noting that the two π fields transform oppositely under the left and right groups, and that the gauged groups here are anomaly free. We thank Hsin-Chia Cheng for pointing out a sign error in an earlier draft of this paper that lead to the wrong conclusion regarding the existence of an LTP.

on the left and right sites. The usual definition of T-parity takes

$$U_{1/2} \to \Omega U_{1/2}^{\dagger}\Omega,\ A_{L/R} \to A_{R/L} \tag{2.10}$$

where

$$\Omega = \begin{pmatrix} 1 & 0 & 0 \\ 0 & 1 & 0 \\ 0 & 0 & -1 \end{pmatrix} \tag{2.11}$$

and we have labeled the Goldstones either d (for block-diagonal) or h (because some combination of these will become the Higgs):

$$U = e^{2i\pi/f_\pi},\ \pi \to \left(\begin{array}{c|c} d & h \\ \hline h^{\dagger} & d \end{array}\right) \tag{2.12}$$

T-parity takes $\mathcal{L}_{\text{kin}}$ to itself. However, as we have just seen, in an $\mathrm{SU}(3)\times\mathrm{SU}(3)/\,\mathrm{SU}(3)$ model the WZW terms flip their sign under the action of T-parity,

$$\mathcal{L}_{\text{WZW}}(\pi, A_L, A_R) \overset{\text{T-Parity}}{\longrightarrow} -\mathcal{L}_{\text{WZW}}(\pi, A_L, A_R) \tag{2.13}$$

An example of this is found in the famous ‘Cheshire Cat’ term with five pion fields that goes to minus itself under $\pi \to -\pi$. Thus, as pointed out by Hill and Hill [31, 32], such terms violate T-parity as defined in Eq. (2.10), independent of the direction of the arrows on the links. This happens because reversing the direction of our links can cancel gauge anomalies, but cannot remove the global anomalies associated with WZW terms. As can be seen in Fig. 2.2, there are anomalous global symmetries present in moose models.

Despite this conclusion, the existence of WZW terms does not necessarily forbid a parity of the theory. As we shall see in the next section, when the two links have opposite orientation, a modification of T-parity remains intact and ensures a stable particle.

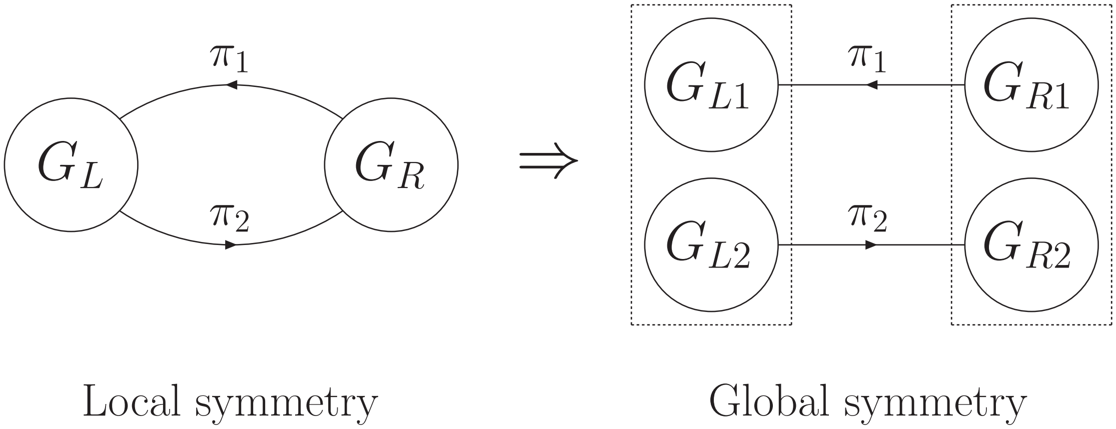

Figure 2.2: The symmetries of the two link moose

2.3 WZW Terms in Multilink Moose Models

There is, however, more to the story of anomalies in multi-link moose models. Although these models contain WZW terms, *when we include multiple links placed in opposite directions we find a parity of the WZW sector!* A theory with this parity has interesting phenomenological implications, the most striking of which is that the LTP is stable. We will begin by describing the parity of WZW terms defined for symmetric spaces, and then show how an extended version T-parity acts to ensure a stable LTP. The example we consider is the two-link model from the previous section, but our arguments can be generalized to physical models with four or more links.

2.3.1 T-parity

We can now exploit the previously defined parity in our multilink moose model to define a new T-parity under which the full theory is invariant. In this case the direction of the link fields is important. As a simplified example, consider a theory of two links positioned in opposite directions. This theory will have the following kinetic terms,

$$\begin{aligned}\mathcal{L}_{\text{kin}}(\pi_1,\pi_2,A) &= f_\pi^2\,\text{Tr}\left|\partial U_1 - iA_{L}U_1 + iU_1A_{R}\right|^2 \\ &+ f_\pi^2\,\text{Tr}\left|\partial U_2 - iA_{R}U_2 + iU_2A_{L}\right|^2\end{aligned} \tag{2.14}$$

Defining the vector and axial combinations,

$$A_{V/A} = \frac{1}{\sqrt{2}}\big(A_L \pm A_R\big) \tag{2.15}$$

we can write the kinetic term as,

$$\begin{aligned}\mathcal{L}_{\text{kin}}(\pi_1,\pi_2,A) &= f_\pi^2\,\text{Tr}\left|\partial U_1 - \frac{i}{\sqrt{2}}\big[A_V,U_1\big] - \frac{i}{\sqrt{2}}\big\{A_A,U_1\big\}\right|^2 \\ &+ f_\pi^2\,\text{Tr}\left|\partial U_2 - \frac{i}{\sqrt{2}}\big[A_V,U_2\big] + \frac{i}{\sqrt{2}}\big\{A_A,U_2\big\}\right|^2\end{aligned} \tag{2.16}$$

We identify the antisymmetric pions

$$\pi_A = \frac{1}{\sqrt{2}}(\pi_1 - \pi_2) = \left(\begin{array}{c|c} d_A & h_A \\ \hline h_A^\dagger & d_A \end{array}\right) \tag{2.17}$$

as the light pions whose mass is protected by collective symmetry breaking. The d_A are eaten by the axial gauge-fields and h_A serves as the SM's higgs doublet.

Now, we define T-parity as,

$$U_{1/2} \to \Omega U_{2/1}\Omega,\ \ A_{L/R} \to A_{R/L} \tag{2.18}$$

Under this parity, the WZW terms transform into themselves,

$$\begin{aligned} & \mathcal{L}_{\text{WZW}}(\pi_1,\ A_L,\ A_R) + \mathcal{L}_{\text{WZW}}(\pi_2,\ A_R,\ A_L) \\ \xrightarrow{T-parity} \quad & \mathcal{L}_{\text{WZW}}(\pi_2,\ A_R,\ A_L) + \mathcal{L}_{\text{WZW}}(\pi_1,\ A_L,\ A_R) \end{aligned} \tag{2.19}$$

so the entire WZW sector is left invariant. This parity guarantees the stability of an LTP. Under this parity, the would be SM Higgs field h_A, as well as the heavy pion d_S, are even. The Higgs' partner, h_S is odd and if lighter than the heavy gauge fields, can serve as the LTP. Otherwise, the lightest of the heavy guage-fields is the LTP.

This modified T-parity can be easily generalized to the more realistic four-link moose models that include plaquette operators. To see this it is instructive to consider the UV perspective of such a theory. The extended version of T-parity we have discussed manifests itself as a relabeling symmetry of the full Lagrangian. A relabeling of condensing fermions and gauge fields in the UV tells us that a relabeling of Goldstones and gauge bosons must be possible in the IR, guaranteeing the preservation of some form of discrete parity. A forthcoming paper will discuss a more realistic scenario with plaquette operators, along with the issues one encounters when one includes SM fermions.

2.4 Conclusions

We have investigated both the conditions for, and phenomenology of, WZW terms in little Higgs models with T-parity. One way to preserve T-parity is through a linear UV completion of the chiral lagrangian into a theory with fundamental scalars (which would likely necessitate supersymmetry). In this paper we explored the possibility of a QCD-like UV completion free of anomalies. We found that unless one resorts to non-standard fermionic UV completions with supersymmetry, or operators with large anomalous dimensions, it is unlikely that anomalous terms can be avoided. Even in moose models with multiple links WZW anomalies cannot be removed. However, in models with multiple links the WZW terms do possess a slight modification of T-parity shared by the entire Lagrangian which permits a stable LTP.

Chapter 3

Semielastic Dark Matter

3.1 Introduction

By now, there is overwhelming evidence supporting the existence of particle dark matter (DM)[1]. Many models of DM have been constructed, most of which incorporate DM into a superstructure added on top of the SM (e.g. the LSP in the MSSM). However, recent efforts[2] to give dark matter a more intricate phenomenology have called for a separate *dark sector*, composed of new gauge groups and light (GeV-scale) degrees of freedom.

Most of these models employing a dark sector focus on the connection between DM and the SM mediated by light fields. If this was the entire story it would be somewhat surprising, because it does not explain the EW/TeV mass scale for DM which relic abundance calculations (i.e. the WIMP miracle) have led us to expect. Here we will consider the simplest mechanism to naturally generate the electroweak/TeV scale in SM and for the DM particles: a singlet which couples to the SM-Higgs/DM fields and get a TeV-scale VEV[3]. *We will see that such a scenario can yield a remarkable,*

---

[1] See Ref. [46, 47] for comprehensive reviews and references

[2] See, for instance, Refs. [25, 48, 27, 28, 49, 50, 51, 52, 53].

[3] Models which connect DM to the visible sector via such a singlet were considered in Refs. [54, 55, 56, 57].

distinct recoil spectrum, visible at the next generation of direct detection experiments.

This paper is structured as follows. In Sec. 3.2 we will introduce an explicit NMSSM-like model realizing the scenario we propose. Sec. 3.3 contains a discussion of the constrains imposed on the model from considerations of relic density. In Sec. 3.4 we discuss the masses and couplings of the model in various limits, and present a benchmark point [4]. Sec. 3.5 contains our conclusions.

3.2 Model

Here we will provide an explicit realization of the scenario described in the introduction. We will take as our starting point the NMSSM [58, 59, 60], where a singlet S couples to the two Higgs multiplets of the MSSM and whose VEV set the size of the μ-term. To this we will add an additional singlet coupling to a pair of fields charged under a dark U(1) field, along with a light dark-sector similar to that of Ref. [51].

3.2.1 Fields and Potential

In detail, the relevant terms in the superpotential for our scenario are

$$W \supset \lambda S H_d \cdot H_u + \eta S \Psi \Psi_c + \frac{1}{3}\kappa S^3 + \rho N R R_c + \frac{1}{\Lambda}\Psi^2 R_c^2 \tag{3.1}$$

where H_d and H_u are the two Higgs doublet fields, S is the NMSSM singlet, Ψ and Ψ_c will compose our DM candidate, R and R_c are GeV-scale dark-sector Higgs fields, and N is a GeV-scale singlet[5]. Here the non-remormalizable term is necessary to generate a small splitting between the DM mass eigenstates. The relevant soft terms

---

[4] The reader is cautioned that these results are preliminary.

[5] As discussed in Ref. [51], N is necessary to marry of fermionic states in the dark-sector so that there are no massless degrees of freedom.

are

$$V_{\text{soft}} \supset \sum_i m_i^2 |\Phi_i|^2 + \left(\lambda A_\lambda S H_d \cdot H_u + \eta A_\eta S \Psi \Psi_c + \frac{1}{3}\kappa A_\kappa S^3 + \rho A_\rho N R R_c + \text{h.c.}\right). \tag{3.2}$$

We will assign R, R_c, Ψ, and Ψ_c, a unit charge under a dark U(1) gauge group[6]. As discussed in Ref. [50], assuming a kinetic mixing of the form

$$\mathcal{L} \supset -\frac{\epsilon}{2} \int d^2\theta W_Y W_u \tag{3.3}$$

for W_Y and W_d the hypercharge and dark supersymmetric field strengths, one finds that the dark-D terms contribute

$$V_D \supset \frac{1}{2}\left[g_D\left(|\Psi|^2 - |\Psi_c|^2 + |R|^2 - |R_c|^2\right) + \xi\right]^2 \tag{3.4}$$

where

$$\xi = \epsilon \langle D_Y \rangle = \epsilon \left(-\frac{g' v_{EW}^2 \cos 2\beta}{4} + \xi_Y\right) \tag{3.5}$$

is an effective FI term induced by the supersymmetric kinetic mixing and ξ_Y is the hypercharge FI term.

3.2.2 Masses

Upon minimizing the dark-sector potential one finds R_c develops a VEV

$$\langle R_c \rangle = \sqrt{\frac{2}{g_d}\left(\xi - \frac{m_{R_c}^2}{g_d}\right)} = v_r \tag{3.6}$$

---

[6] The relative sign of the charge for each field is fixed by demanding Eq. (3.1) remain gauge invariant.

where g_d is the dark gauge coupling. This higgses the dark photon, giving it a mass

$$m_{\gamma_d} = g_d v_r. \tag{3.7}$$

The other light dark-sector states also live at the GeV-scale. While their precise masses will not affect the phenomenology we study, we note that there can be $\mathcal{O}(1)$ corrections to the masses coming from the SM SUSY breaking mediated to the dark-sector by the singlet and the Ψ fields. We discuss these corrections in Appendix H.

Turning to the TeV-scale fields Ψ and Ψ_c, one finds two fermionic states separated by a small splitting

$$m = \frac{\eta v_s}{\sqrt{2}}\left(1 \pm \frac{v_r^2}{2\Lambda}\right). \tag{3.8}$$

In what follows we will assume that the supersymmetry breaking soft terms relevant to the behavior of Ψ and Ψ_c (A_η, m_Ψ^2, and $m_{\Psi_c}^2$) are small compared to their supersymmetric counterparts. Under this assumption, the four scalar degrees of freedom divide into two sets above and below Eq. (3.8) separated by a relatively large splitting

$$m^2 = \eta\left[\frac{v_s^2}{2}(\eta \pm \kappa) \mp \frac{\lambda}{4} v_{EW}^2 \sin(2\beta)\right] \tag{3.9}$$

where v_s is the singlet VEV, while within each set there is a smaller splitting

$$\delta m^2 = \sqrt{2}\eta \frac{v_s v_r^2}{\Lambda} \tag{3.10}$$

where v_r is the VEV of the dark Higgs. In what follows, we will label the scalar mass eigenstates χ_i for $i : 0 \rightarrow 3$ in order of ascending mass.

3.3 Relic Abundance Constraints

Demanding that this model reproduce the observed relic abundance of dark matter places strong constraints on the different couplings and VEVs. In what follows we will use that

$$\langle \sigma v \rangle \approx \frac{|\mathcal{M}|^2}{32\pi m_\chi^2} \tag{3.11}$$

where $\langle \sigma v \rangle$ is taken to be

$$\langle \sigma v \rangle \approx 3 \times 10^{-26} \frac{\mathrm{cm}^3}{\mathrm{s}} \approx 2.5 \times 10^{-9}\ \mathrm{GeV}^{-2}. \tag{3.12}$$

Here we will only consider contributions to annihilation from the $\chi_0 \chi_0$ initial state. Of course, since χ_0 and χ_1 are split by a small mass, a more calculation of relic abundance would account for these additional channels. However, no major new final states become accessible/enhanced when considering this channel (or any other channel with other TeV-scale initial states), so the estimates presented below should still be correct to within $\mathcal{O}(1)$ factors.

Singlet VEV

If dark matter is to be at the TeV scale then, barring some conspiracy, it is kinematically allowed to annihilate into all the scalars and pseudoscalars of the Higgs sector. Assuming all of these are light compared to m_χ, one finds

$$\langle \sigma v \rangle_{\mathrm{scalars}} \gtrsim \frac{1}{8\pi} \left(\frac{5 m_\chi}{v_s^2} \right)^2 + \frac{\lambda^4}{4\pi m_\chi^2} \tag{3.13}$$

and

$$\langle \sigma v \rangle_{\mathrm{pseudos}} \gtrsim \frac{1}{8\pi} \left(\frac{m_\chi}{v_s^2} \right)^2 + \frac{\lambda^4}{4\pi m_\chi^2}. \tag{3.14}$$

Constraints on the annihilation into protons tell us we must have a relatively low ($\lesssim 1/3$) annihilation rate into higgses, so we find

$$v_s \gtrsim 6 \text{ TeV} \left(\frac{m_\chi}{1 \text{ TeV}}\right)^{1/2}. \tag{3.15}$$

Note that, even if the real-scalar singlet state was beyond the kinematic decay threshold we would still be forced to live with a large v_s because of the constraints from the decay into pseudoscalars (Eq. 3.14). This would tell us

$$v_s \gtrsim 2.5 \text{ TeV} \left(\frac{m_\chi}{1 \text{ TeV}}\right)^{1/2} \tag{3.16}$$

Finally, we note that while there are constraints on λ, they are far less severe:

$$\lambda \lesssim 0.6 \left(\frac{m_\chi}{1 \text{ TeV}}\right)^{1/2} \tag{3.17}$$

Splitting

The non-renormalizable operator used to generate the small splitting leads to

$$\mathcal{L} \supset \frac{m_\chi \delta m_\chi}{2v_r^2} \chi_0^2 r_c^2 \tag{3.18}$$

which contributes

$$\langle \sigma v \rangle \sim \frac{(\delta m_\chi)^2}{8\pi v_r^4}. \tag{3.19}$$

Therefore, we find a non-trivial constraint on the mass splitting between our dark matter states:

$$\frac{\delta m_\chi}{v_r^2} \lesssim 10^{-4} \text{ GeV}^{-1} \to \left(\frac{\delta m_\chi}{100 \text{ keV}}\right)\left(\frac{1 \text{ GeV}}{v_r}\right)^2 \lesssim 1 \tag{3.20}$$

Dark gauge coupling

Finally, when we account for the annihilation rate due to the dark gauge coupling we find

$$\langle \sigma v \rangle \sim \frac{g_d^4}{8\pi m_\chi^2} \tag{3.21}$$

so

$$\left(\frac{g_d}{0.5}\right)^2 \left(\frac{1\ \mathrm{TeV}}{m_\chi}\right) \lesssim 1 \tag{3.22}$$

3.4 Masses and Couplings

It is convenient to study this model in a limit where it becomes amenable to analytic approximations. One finds that regardless of whether one starts in a PQ or R-symmetric[7] limit the result is the same: if the model is to yield an acceptable electroweak symmetry breaking vacuum with a large v_s and exhibit a recoil spectra visible at the next round of direct detection experiments it must possess a small λ, κ. Furthermore, unless the elastic scattering is mediated by the singlet, it will be difficult to see. Under these assumptions one finds

$$\sigma_{\mathrm{el}} \approx 1.2 \cdot 10^{-34}\ \mathrm{cm}^2 \left(\frac{m_\chi}{v_s}\right)^2 \left(\frac{1\ \mathrm{GeV}^4}{m_s^4}\right) \max\left[g_H \alpha_{H,s}, g_h \alpha_{h,s}\right]^2 \tag{3.23}$$

where

$$g_H = 1.2 \tan\beta - 0.5 \cot\beta,\ \ g_h = 1.7 \tag{3.24}$$

and

$$\alpha_{h,s} \approx \frac{2\lambda v_w \left(\lambda - \kappa \sin(2\beta)\right)}{\kappa \left(4\kappa v_s + \sqrt{2} A_\kappa\right)} \tag{3.25}$$

$$\alpha_{H,s} \approx \frac{-2\lambda v_w \cos(2\beta)}{\sqrt{2} A_\kappa + 4\kappa v_s + 2\lambda v_s / \sin(2\beta)} \tag{3.26}$$

---

[7] See [61, 62, 63, 64, 65, 66, 67, 68] for more detailed discussions of the NMSSM in these limits.

The masses of the CP-even Higgs states are, at lowest order,

$$m_h^2 \approx m_z^2 \cos^2(2\beta) \tag{3.27}$$

$$m_s^2 \approx 2\kappa^2 v_s^2 + \frac{1}{\sqrt{2}}\kappa A_\kappa v_s \tag{3.28}$$

and

$$m_H^2 \approx \frac{v_s}{\sin(2\beta)}\left(\kappa\lambda v_s + \sqrt{2}\lambda A_\lambda\right) \tag{3.29}$$

It is important to note that while Eq. (3.24) might suggest that the coupling of the singlet to nucleons can be freely adjusted through the choice of $\tan\beta$, one finds from Eq. (3.26) that this reduces the H/S mixing by a corresponding amount, and in fact the coupling cannot be made arbitrarily large.

3.4.1 Benchmark Point

Using the relations from above, the astrophysical/nuclear parameters of Refs. [69, 70, 71, 72] and setting $\lambda = 2.5 \cdot 10^{-2}$, $\kappa = 6 \cdot 10^{-3}$, $\tan\beta = 15$, $g_d = 0.35$, $\eta = 0.2$, and $\epsilon = 10^{-5}$, one arrives at a scenario with $m_s \approx 21$ GeV, light enough to mediate a significant amount of elastic scattering. The recoil spectrum resulting from this choice of parameters is shown in Fig. 3.1.

3.5 Conclusions

Here we have presented results from a scenario which naturally extends the latest generation of DM models, which focus on scattering mediated by GeV scale hidden states, to include a mechanism for introducing the TeV scale into each sector. We found that this simple extension results in a qualitatively new, distinct recoil spectrum visible at the next generation of direct detection experiments. While still preliminary, these results seem quite promising, and may provide a smoking gun signature for the

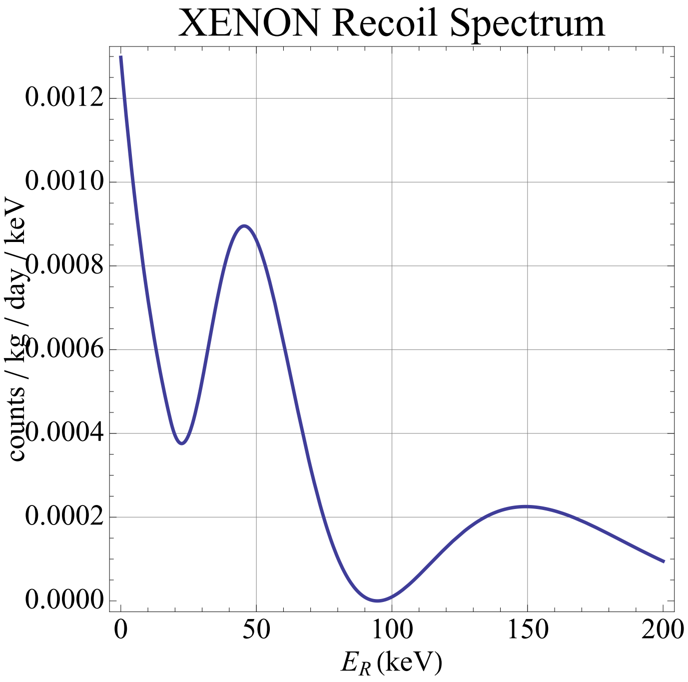

Figure 3.1: Benchmark recoil spectrum visible at XENON100.

presence of light dark-sectors.

Chapter 4

New Physics Signals in Longitudinal Gauge Boson Scattering at the LHC

We introduce a novel technique designed to look for signatures of new physics in vector boson fusion processes at the TeV scale. This functions by measuring the polarization of the vector bosons to determine the *relative* longitudinal to transverse production. In studying this ratio we can directly probe the high energy E^2-growth of longitudinal vector boson scattering amplitudes characteristic of models with non-Standard Model (SM) interactions. We will focus on studying models parameterized by an effective Lagrangian that include a light Higgs with non-SM couplings arising from TeV scale new physics associated with the electroweak symmetry breaking, although our technique can be used in more general scenarios. We will show that this technique is stable against the large uncertainties that can result from variations in the factorization scale, improving upon previous studies that measure cross section alone.

4.1 Vector Boson Fusion as a Probe of New Physics

The Large Hadron Collider (LHC) was built to elucidate the physics behind electroweak symmetry breaking (EWSB). In a sense, it must succeed in finding some new physics because the partial wave amplitudes for $V_L V_L \to V_L V_L$ scattering,[1] calculated in the absence of a Higgs or other new physics, begin to violate unitarity at the TeV scale. Therefore, either new weakly-coupled light particles must come in to unitarize the amplitudes, or we will see new strong interactions in the electroweak sector.

While many models of EWSB have been proposed, precision experiments such as LEP seem to favor a model employing a $\mathcal{O}(100)$ GeV scalar with the quantum numbers and approximate couplings of the Standard Model (SM) Higgs [73, 74]. Many models of new physics already include such a particle, oftentimes with couplings deviating slightly from those of the SM, *e.g.* little Higgs [23] and holographic Higgs models [75]. Ideally, such models would be identified and studied at the LHC through the production of their intrinsic new particles. However, the finite energy reach and large backgrounds at the LHC could make discovering any new states very difficult.

Thus we will focus on these non-SM light Higgs scenarios, both because they are favored by precision data and because they are perhaps the most difficult to distinguish from the SM. To study these setups we will take a model-independent approach, employing an effective field theory to parameterize the effects of new physics [21, 76, 77, 78, 79, 80]. We will see that the general phenomenology of the Higgs sector is captured by the coefficients of a small number of dimension-6 operators [81, 82], only one of which is relevant to the vector boson fusion process we wish to study.

Vector boson fusion (VBF) is the process in which vector bosons radiated by initial state quarks scatter into vector bosons (see Fig. 4.1). This process is intimately tied to EWSB: just as the pion is a Nambu-Goldstone boson (NGB) and $\pi\pi$ scattering

---

[1] By V_L we denote a longitudinally polarized electroweak vector boson.

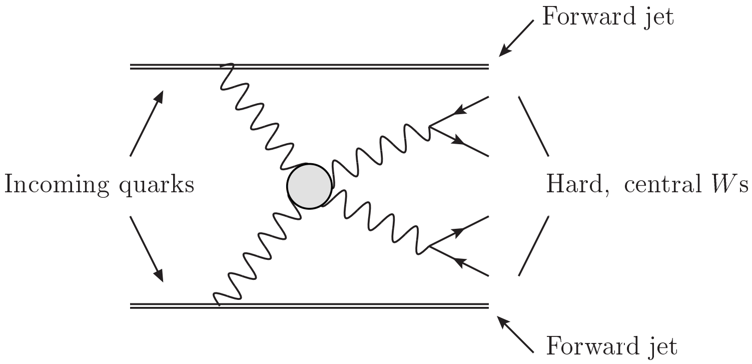

Figure 4.1: Illustration for vector boson fusion.

can be used to understand chiral symmetry breaking, at high energies longitudinally polarized vector bosons take on the behavior of the NGBs from EWSB. In the absence of a Higgs boson or other new physics responsible for the EWSB, the scattering amplitudes probed by VBF would violate perturbative unitarity [83, 84, 85, 86] at around 1 TeV (see the discussion in appendix F). Furthermore, if the Higgs boson does not have the *exact* couplings to vector bosons as predicted by the SM, then the necessary cancelations will not occur and one will still observe an E^2 growth in the amplitudes until new physics comes into play. It is by measuring this growth that we can hope to observe the effects of physics beyond the SM, even in scenarios where we only see a light Higgs-like particle [82, 87].

In this article we will introduce a novel technique designed to analyze VBF processes and observe the E^2 growth in longitudinal gauge-boson scattering amplitudes mentioned above. We will begin by introducing our notations and framework in Section 4.2. In Section 4.3 we will describe our technique designed measure the *relative* production of transverse to longitudinal modes, focusing on the fully reconstructable semi-leptonic decay of the VV system. We will demonstrate that this measurement is sensitive to anomalous Higgs-gauge couplings while at the same time being robust against the scale uncertainties that challenge cross section measurements. Section 4.4 contains our conclusions.

4.2 Theoretical Setup

In the formulation of a general effective theory of the SM-like Higgs sector [21, 76, 81] most of the operators are tightly constrained [77, 78, 79, 80] because of their otherwise excessive contributions to the electroweak observables, such as the ρ-parameter, oblique parameters, and triple gauge boson self-interactions. There are only two dimension-six operators that are genuine interactions in the Higgs sector not subject to the stringent experimental constraints,[2] $\partial^\mu(H^\dagger H)\partial_\mu(H^\dagger H)$ and $(H^\dagger H)^3$. We note that as both operators are composed from the singlet operator $H^\dagger H$ they may serve to probe not only EWSB physics, but also other physics beyond the SM. For a given theoretical framework, the coefficients of these operators may be calculable [82], and by measuring them we can hope to learn about any new physics. Even in some strongly coupled models for which these may not be calculable, the measurement of a non-zero value can give important clues to the structure of new physics. Now, the second operator above does not have derivative couplings, so its effect on the behavior of the V_L scattering amplitudes at high energies should be sub-leading [81]. We therefore focus on the former and parameterize it (following [82]) as

$$\mathcal{L} \supset \frac{c_H}{2f^2}\partial^\mu(H^\dagger H)\partial_\mu(H^\dagger H), \tag{4.1}$$

where the coefficient c_H is naturally of $\mathcal{O}(1-4\pi)$ depending on whether the underlying theory is weakly or strongly coupled, and f is the characteristic scale of new physics, typically expected to be round $4\pi v$ if the new physics is associated with EWSB.

Upon expanding around the electroweak VEV v, this operator contributes terms which add to the kinetic terms of H. After imposing canonical normalization on the fields, the result is a modification to the Higgs couplings. Ref. [82] parameterizes the

---

[2] As discussed in [88], the first of these operators can induce corrections to the oblique parameter S [89], leading to $\sim 2\sigma$ deviations in S for the range of anomalous couplings included here. However, shifts in S can be compensated for by the presence of additional heavy states. We thus believe that these parameters should still be considered viable.

resulting modified Higgs-gauge coupling in the zero-momentum limit as

$$g_{\text{eff}} = \frac{g_{\text{SM}}}{\sqrt{1 + c_H \xi}} \approx g_{\text{SM}} \left(1 - \frac{c_H}{2}\xi\right) \tag{4.2}$$

where $\xi = v^2/f^2$. This modified coupling has important phenomenological consequences because it deviates from the SM prediction. At high energies and for $|c_H\xi| \gtrsim 0.1$ [3] this modification leads to an incomplete cancelation in the amplitude for longitudinal vector boson scattering and the cross section grows as

$$\sigma(V_L V_L \to V_L V_L) \approx \left(\frac{c_H}{2}\xi\right)^2 \sigma(V_L V_L \to V_L V_L)_{\text{no}-\text{higgs}}. \tag{4.3}$$

which can be seen by considering the NGB scattering as shown in appendix F. In what follows we will study means of measuring this behavior. Note that, as discussed in appendix F, the $W_L^+ W_L^-$ scattering amplitudes calculated in this framework violate perturbative unitarity when

$$s_{WW} \approx \frac{16\pi v^2}{c_H\xi \left(1 - \frac{c_H\xi}{4(1+c_H\xi)}\right)}. \tag{4.4}$$

This is the point at which we expect new physics to come into play. In what follows we will limit our analyses to

$$\sqrt{s_{VV}} < 2 \text{ TeV}. \tag{4.5}$$

This corresponds to a coupling value $|c_H\xi| \sim 0.6$. We will take this as an upper limit for our analyses. Of course, looking beyond this energy range would be interesting and should be attempted at the LHC, but any deviation from the SM expectation would no longer carry the same effective Lagrangian interpretation. Also, note that for larger couplings and lower scales of new physics some higher dimensional operators

---

[3] For smaller values of $|c_H\xi|$ the dominant non-SM effects enter as interference terms proportional to $c_H\xi$ rather than $(c_H\xi)^2$. Also, in this case the anomalous energy dependence of the longitudinal cross section goes as E^2 instead of E^4.

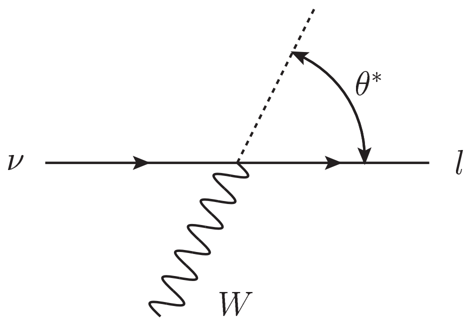

Figure 4.2: The polarization axis used to measure θ^*. Note that this is measured in the rest frame of the W, and the W direction of motion is defined with respect to the WW center of mass.

could become relevant and it would be more appropriate to think of the $c_H\xi$ used in our analysis as parameterizing a new physics form factor, rather than as the coefficient of a particular operator.

4.3 Polarization Measurements

With the uncertainties detailed above as our motivation, we propose a new technique to probe the anomalous couplings in a robust way. Our basic idea is to look for the *relative* increase in longitudinal vector boson production by comparing it to the production of transverse modes. Unlike the overall cross section, which is sensitive to the behavior of the forward jets, the relative transverse to longitudinal production rates should be stable against different scale choices because it depends only on the $VV \to VV$ scattering amplitude. To measure the polarization of a vector boson we need to reconstruct the four-momenta of its decay products and measure their distribution with respect to a polarization axis. If one chooses the polarization axis to be the gauge boson direction of motion (Fig. 4.2), then a simple spin-analysis predicts that in the V rest frame the transverse and longitudinal polarizations will be distributed as [4]

$$P_{\pm}(\cos\theta^*) = \frac{3}{8}(1 \pm \cos\theta^*)^2,\ P_L(\cos\theta^*) = \frac{3}{4}(1 - \cos^2\theta^*) \tag{4.6}$$

where θ^* denotes the angle between the parton and the gauge boson direction of motion in the gauge boson rest frame. [5]

To measure these distributions experimentally, we need to fully reconstruct the gauge boson pair center of mass and each gauge boson's direction of motion in this frame. To accomplish this we will focus on the semi-leptonic decay channel of the VV system as this allows full reconstruction of the system while minimizing the SM background by requiring leptons and missing energy. The semi-leptonic channel also significantly increases the signal event rate. For this we will rely upon jet substructure techniques to reconstruct the hadronically decaying gauge boson [90]. We will focus on studying the W^+W^- final state, although we will take into account the background from other VBF processes like $W^{\pm}W^{\pm}$ and $W^{\pm}Z$ that enter because we can not distinguish the sign of a hadronically decaying vector, nor can we always distinguish a hadronically decaying W from a Z. Later in this section we will comment on the SM $\mathcal{O}(\alpha_S^2)$ and $\mathcal{O}(\alpha_S^4)$ backgrounds.

4.3.1 Leptonic Polarization

We begin with the polarization analysis for the leptonic side of the decay. We first study the parton-level results, then we will turn on the full simulation (parton-showering and jet clustering) to see that they are largely unchanged.

Before proceeding further, we encounter a subtlety in the reconstruction of the leptonic system: While the neutrino four-momentum is constrained by the on-shell W

---

[4] Note that these distributions can be modified when cuts are placed on the individual W decay products, rather than on the W momenta.

[5] We alert the reader to the fact that θ^* is sometimes also used in the VBF literature (e.g. [90]) to refer to the angle between incoming and outgoing vector bosons.

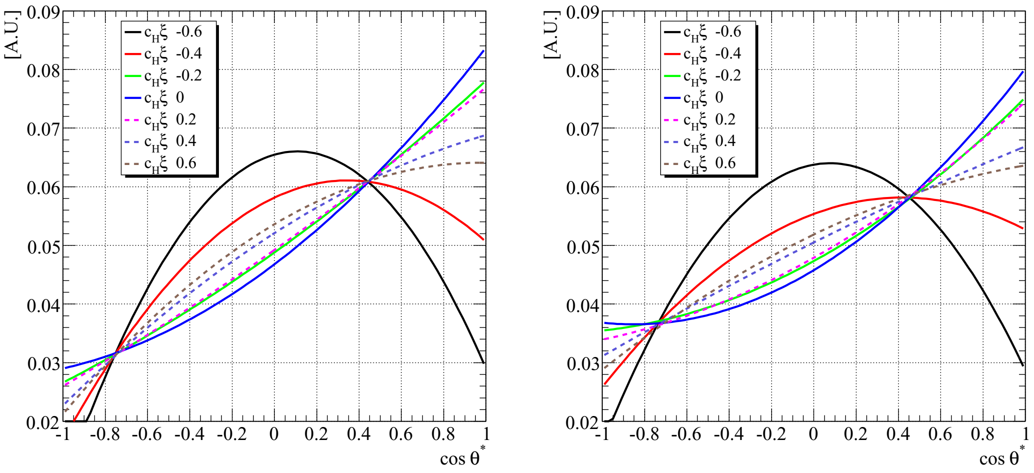

Figure 4.3: The distributions of $\cos\theta^*$ for different anomalous couplings at parton level (left) and for fully showered, hadronized, clustered, and reconstructed events (right). All distributions are normalized to the same area.

condition, it is only determined up to a discrete ambiguity. One finds two candidate four-momenta at the same azimuthal angle but separated from the charged lepton by a fixed rapidity difference. In what follows we will simply use the average $\cos\theta^*$ value from both solutions as an approximation of the true value. This is acceptable because we are working in a boosted regime where the difference in rapidity between neutrino and lepton is small, making the curvature effects from the (y, ϕ) system sub-leading. The resultant distributions are shown in Fig. 4.3, at parton level (left panel) and after the hadronization (right panel). The characteristic shapes with different couplings are quite distinctive. In Table 4.1 we compute the cross section for each anomalous coupling and fit it to the transverse and longitudinal distributions of Eq. (4.6) using

$$P(\cos\theta^*) = f_L P_L(\cos\theta^*) + f_+ P_+(\cos\theta^*) + f_- P_-(\cos\theta^*) \tag{4.7}$$

where the P are normalized probability distributions of $\cos\theta^*$ and the f are subject to the constraint $\sum f = 1$. As one can see from comparing the jet and parton level figures, the results are remarkably stable under a full simulation.

	Leptonic W		Hadronic W		
$c_H\xi$	f_L^P	f_L^J	f_L^P	f_L^J	σ [fb]
-0.6	0.71	0.70	0.71	0.55	3.38
-0.4	0.49	0.48	0.49	0.40	1.12
-0.2	0.23	0.26	0.23	0.24	0.60
0.0	0.17	0.22	0.17	0.22	0.62
0.2	0.24	0.27	0.24	0.26	0.65
0.4	0.32	0.35	0.32	0.32	0.73
0.6	0.40	0.38	0.40	0.38	0.87

Table 4.1: The fraction of longitudinally polarized vector bosons for different anomalous couplings at parton level f_L^P and jet level f_L^J, reconstructed in hadronic and leptonic decays. Also listed are the jet-level cross sections. These results are after the cuts of Table **??**.

In Figure 4.4 we plot the projected event distributions and associated statistical errors both for the SM and for an anomalous scenario with $c_H\xi = -0.4$, given 100 fb^{-1} of luminosity. The shape difference between the two samples is clearly visible. To estimate the luminosity necessary to probe a given coupling, one can use that the signal scales roughly as $(c_H\xi)^2$, as discussed before. However, the precise reach of the LHC in discerning anomalous couplings will require a more thorough accounting of background. Further, we have not made an effort to optimize the statistical power of the analysis and there are other channels that contribute to the signal, such as $W^+W^+, W^\pm Z$ and ZZ. In addition, one can extract more information from each event, as we will now see.

4.3.2 Hadronic Polarization

It is possible to further improve the discriminating power of polarization by considering both sides of the VV system together; by looking for the expected *correlation* between both states one can hope to gain additional discriminating power.

To see the correlation effect, consider Fig. 4.5, which shows the parton-level $\cos\theta^*$ distributions for both sides of the VV system in SM and non-SM scenarios. For now,

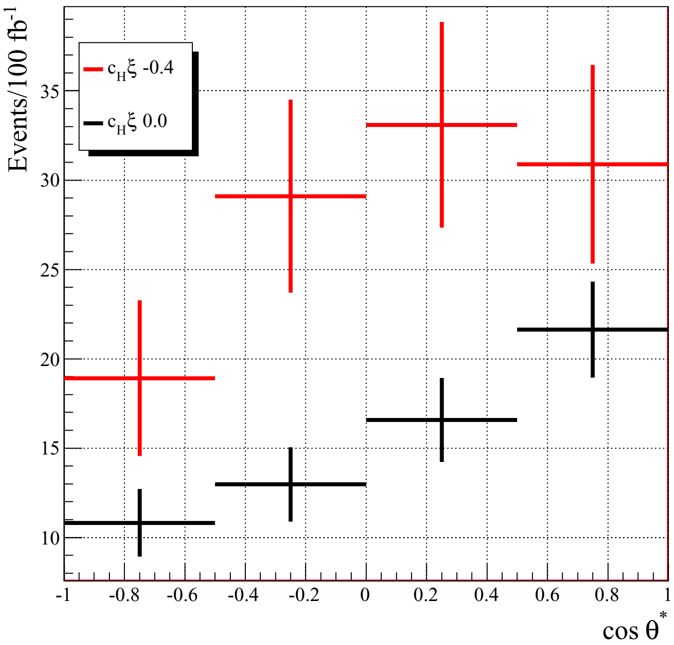

Figure 4.4: Projected distribution and associated statistical uncertainties of $\cos\theta^*$ for the leptonically decaying vector using 100 fb^{-1} of luminosity.

we plot $\cos\theta^*$ on the hadronic side for the down-type quarks. In the non-SM scenario we see a rapid rise in the central region of the plot near $\cos\theta^* \approx 0$. This indicates that the results are correlated; when we see a V_L it is likely to be accompanied by a V_L because only the V_LV_L final state sees the E^2 growth characteristic of with non-SM effects. In practice the situation is slightly more complicated because we cannot label the light quark states once they shower and hadronize (e.g. we cannot distinguish a u from a d), so the distributions we measure are symmetrized. However, the distributions still carry additional discriminating power, as one can see from the distributions in Fig. 4.3.2 and Fig. 4.7, and Table 4.1. Note that in fitting the symmetrized distributions we only fit to data from $0 < |\cos\theta^*| < 0.7$. In the regime where $|\cos\theta^*| \gtrsim 0.7$ one subject becomes very soft and the technique breaks down (although, of course, the leptonic analysis still works here).

To perform this analysis we had to look at the hadronically decaying V using

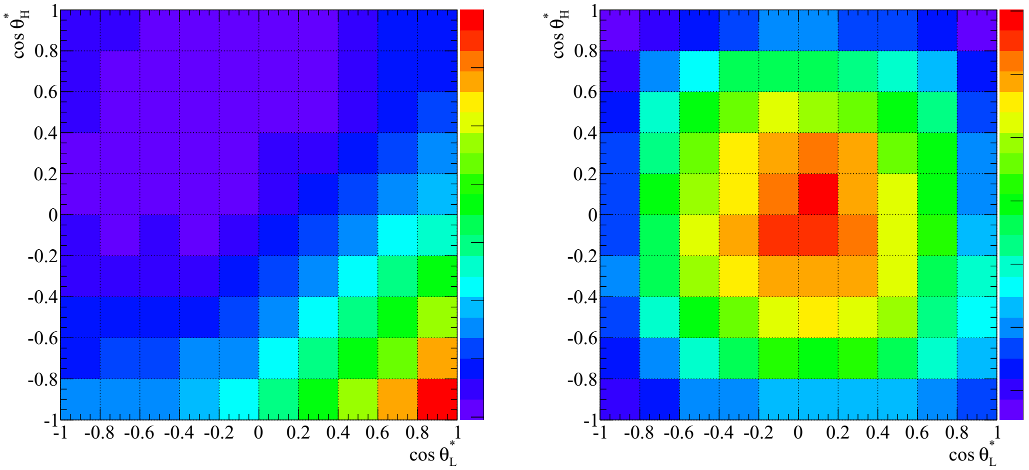

Figure 4.5: Distributions of $\cos\theta^*$ at parton-level for both sides of the VV system (labeled with subscript H and L for hadronic and leptonic decays, respectively). The plot on the left is for the Higgs with SM couplings, while the one on the right is for $c_H\xi = -0.6$. The scale is individually normalized for each plot, going from violet to red as the concentration of events increases. The scaling of the color gradient on the right side of each plot is linear.

subjet techniques (for a short overview of jet algorithms and their behavior, see appendix G). In particular, we used the k_T algorithm [91, 92] with $R = 0.25$ to cluster the constituents of each hadronically decaying gauge boson, using the two most energetic subjets (as measured in the VV center of mass frame) for our analysis. Note that rather than identifying our subjets through a C/A [93, 94] or k_T-like unwinding [95, 96], we used fixed small cones (i.e. small R). Otherwise, the subjets encompass a large area and become more susceptable to contamination from initial state radiation, multiple interactions, and event pileup. The choice of a small cone seems to result in a better reconstruction of events, especially at high values of $\cos\theta^*$ when there is a large difference in the subjet p_Ts. Furthermore, we use k_T rather than anti-k_T to form our subjets because it more accurately reconstructs the softer jet in situations where the jets are nearly collinear (see appendix G).

One important thing to consider in the subjet analysis is that the results are not as robust in going from matrix-element to parton shower as were the leptonic results;

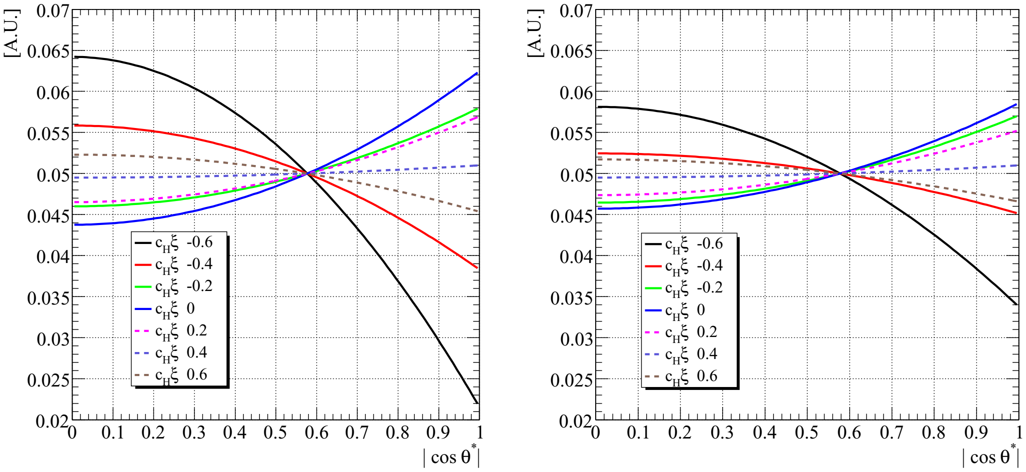

Figure 4.6: Distribution of $|\cos\theta^*|$ at different anomalous couplings for hadronically decaying Ws using parton level samples (left) and fully showered, hadronized samples (right). Note that the distributions differ more at high values of $\cos\theta^*$ because this is the region in which one jet is relatively soft.

the curves change shape (compare the parton and jet level results for both sides of the decay in Table 4.1). This is because the diffuse nature of the subjets makes them difficult to resolve when they become collinear and/or soft. We note, however, that at the LHC we can expect to calibrate subjet measurements for boosted hadronic Ws with large SM samples, and while the parton-level to jet-level results may vary, the correspondence should eventually be well understood. Thus the leptonic gauge boson analysis is likely to be the first tool used, but the hadronic analysis can be added later on.

4.4 Conclusions

In this article we have introduced a powerful new technique for identifying signs of beyond the SM physics associated with the EWSB by probing VBF processes at the LHC.

We began by motivating our decision to study models of EWSB employing a light

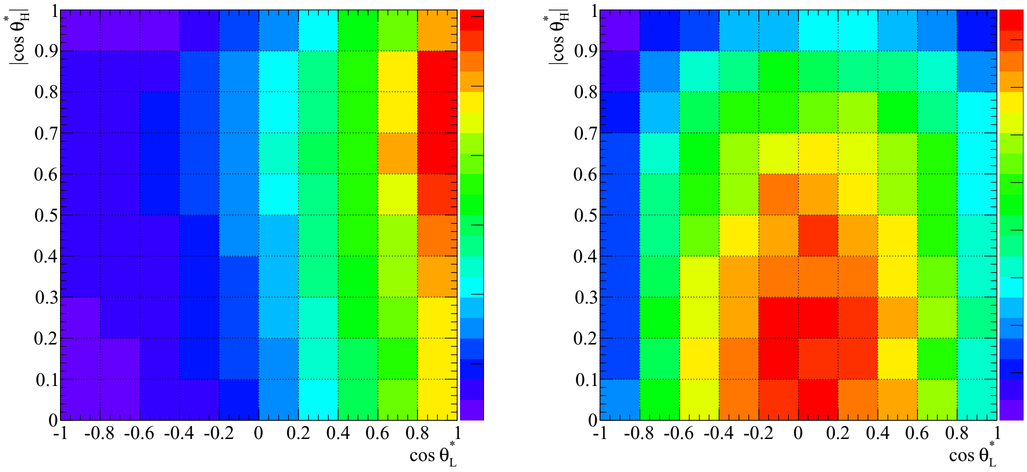

Figure 4.7: Jet-level distribution of $\cos\theta^*$ (labeled with subscript H and L for hadronic and leptonic decays, respectively) for the SM Higgs (left) and Higgs with $c_H\xi = -0.6$ (right). The scale is individually normalized for each plot, going from violet to red as the concentration of events increases. The scaling of the color gradient on the right side of each plot is linear.

Higg-like particle with couplings deviating from those of the SM. Theories with a light Higgs boson are favored by the current electroweak precision data. However, this type of model is the most difficult to distinguish from the SM, especially if the new physics particles are very heavy. However, it is also the scenario in which VBF can be most useful, because for such a scenario the amplitude for $V_LV_L \rightarrow V_LV_L$ scattering exhibits a non-SM E^2 growth until new physics comes into play.

Past analyses designed to measure this E^2 growth were reviewed and updated to account for the effects of the parton shower and jet clustering. While the cuts pioneered by these works can be very powerful in reducing the SM background, we demonstrate that there is still a significant $\mathcal{O}(100\%)$ rate uncertainty attributable to factorization scale ambiguities. Thus, we show that in the absence of higher order calculations that might give us some guidance on the correct scale treatment, rate information alone may not be sufficient to distinguish the signs of new physics.

We then propose our new technique, which uses the semi-leptonic decay mode of the VV system to fully reconstruct events and obtain the decay angle distributions for the V daughters. These distributions can be decomposed into longitudinal and transverse components, allowing us to measure the E^2 growth in scattering amplitudes associated with new physics by looking for the relative increase in longitudinal production. We demonstrate that these results are insensitive to the scale ambiguities that trouble rate measurements.

In closing, we wish to reiterate that polarization measurements of VBF final states are a powerful, robust probe of new physics associated with the EWSB. Although we have only employed them here to study light SM-like Higgs scenarios, they would be useful in more general scenarios of EWSB as long as the longitudinal gauge bosons are significantly involved. Such measurements may prove to be our best tool in understanding the physics of EWSB at the LHC.

Chapter 5

Measuring the Polarization of Boosted Hadronic Tops

We propose a new technique for measuring the polarization of hadronically decaying boosted top quarks. In particular, we apply a subjet-based technique to events where the decay products of the top are clustered within a single jet. The technique requires neither b-tagging nor W-reconstruction, and does not rely on assumptions about either the top production mechanism or the sources of missing energy in the event. We include results for various new physics scenarios made with different Monte Carlo generators to demonstrate the robustness of the technique.

5.1 Introduction

The top quark, with its large coupling to the Higgs sector, plays an important role in models of physics beyond the Standard Model. Indeed, many such models posit the existence of top partner states (e.g. the stop squark of SUSY [15] and the T' of little Higgs models [23]) or otherwise couple the top to new physics in a special way (as with KK-gluons [97]). Measuring the couplings of the top to new states is therefore essential in distinguishing the correct model of physics beyond the Standard Model.

One especially interesting aspect of these couplings is their chirality: whether or not they distinguish left- from right-handed tops. Fortunately, the large mass of the top, which makes its study so interesting for electroweak physics, makes it possible to imagine measuring the chiral couplings of the top directly. Unlike the other quarks, the top decays before hadronization, so information about its spin is transferred to the distributions of its decay products [98]. On the other hand, the large mass of the top also means that in order for the chiral couplings of tops to new physics to translate into observable top polarization signals, the tops must be significantly boosted, as chirality only becomes equivalent to helicity in the massless limit. Boosted tops are therefore a natural and interesting place to look for polarization signals.

Conventional methods for measuring the polarization of non-boosted tops begin by reconstructing the top rest frame and considering the angular distributions of its decay products in that frame, and often focus on the semi-leptonic decay mode, which can be fully reconstructed if the only missing energy in the event comes from the neutrino. Such techniques have been extended to events where the hadronic top is boosted, but the lepton from the leptonic top decay is still isolated. This isolated lepton can then be used to measure the polarization of its parent top, either by reconstructing the $t\bar{t}$ system [99] or through the shape of the lepton p_T spectrum [100].

When the top quark is highly boosted, however, requiring an isolated lepton begins to require a significant acceptance price. Moreover, while the large spin analyzing power of the lepton in standard model top decay makes it particularly useful for top polarization studies, it is also desirable to develop techniques which can measure polarization in boosted tops without the need for an isolated lepton. Being able to study polarization in boosted hadronic tops increases acceptance, and has the additional feature of *flexibility*: unlike leptonic tops, hadronic tops are fully reconstructable in events with multiple sources of missing energy. For highly boosted tops, the finite angular resolution of the detector makes complete reconstruction of the system difficult, and angular distributions in the top rest frame are no longer optimal observables.

Here we present a technique to measure the polarization of a boosted top in its hadronic decay mode using the energy fraction distribution of a particular subjet. This new method does not require high-p_T b-tagging, which is known to be challenging. We also do not require W reconstruction inside the top jet. Again, as we are considering hadronic tops, this technique measures top polarization using information from the top jet alone, independent of other objects in the event. It does not involve the reconstruction of top rest frame, or rely upon the measurement of missing momentum.

While identification of boosted hadronic tops above the QCD background is challenging, many promising approaches have been developed [101, 99, 102, 100, 103, 104, 105, 106, 96, 107, 108, 109, 110, 111, 112]. In this article we will assume that the boosted top candidates can be identified through one of these methods.

We will begin by motivating our choice of a subjet-based technique for studying the substructure of a top-jet. Then we will propose an algorithm useful for measuring the top polarization and discuss its interpretation. Finally, we will demonstrate the robustness of the algorithm by testing it in different physics scenarios with data from different parton shower models.

5.2 Looking Inside a Top Jet

Here we will discuss the different techniques used to study boosted hadronic tops. This will give us a chance to motivate our use of subjets while outlining other possibilities.

In the past, two distinct approaches have been taken to analyze top jets. One approach uses jet shape variables [108, 109, 96] to define a function on the constituents of a top jet (in practice, the constituents will be calorimeter cells), treating each constituent independently. The other approach [96, 107, 111, 112] defines a function on the subjets formed by reclustering the constituents of a larger jet. Functions then depend upon the constituent four-momenta only through the total four-momentum of the subjet they are clustered into, rather than upon each constituent four-momentum independently.

Each approach has both advantages and disadvantages. Subjets can reduce the effects of soft contamination [1] by summing together constituents so that softer particles have a proportionally smaller influence. However, care must be taken because some quantities one can form from subjets, such as invariant mass, can be extremely sensitive to calorimeter spacing and out-of-cone radiation. Fortunately, as long as one avoids these troublesome quantities a subjet-based analysis can be made fairly robust. For our algorithm below, we will only rely upon the relative hardness and separation of the subjets, both quantities which are fairly insensitive to additional soft radiation and detector effects.

Jet shape variables, because they treat each jet constituent independently, are more amenable to higher order calculations than variables defined with subjets. However, these variables can become very sensitive to the effects of contamination. As an example, consider the *planar flow* jet shape of [108], which is equivalent (up to an overall constant) to $\det S^{\perp}$ defined in [96]. The planar flow of a jet is defined as

$$\mathrm{Pf} = \frac{4\lambda_1\lambda_2}{(\lambda_1+\lambda_2)^2} \tag{5.1}$$

where $\lambda_{1,2}$ are the two eigenvalues of the matrix

$$I_w^{kl} = \sum_i w_i \frac{p_{i,k}}{w_i}\frac{p_{i,l}}{w_i} \tag{5.2}$$

---

[1] Contamination, radiation clustered within the top jet that did not arise from the top decay, can be the result of initial state radiation, multiple interactions, or wide angle emissions from other parts of the event.

where w_i is the energy and $p_{i,k}$ the kth transverse momentum component of the ith jet constituent. This quantity essentially decomposes the jet's radiation into two moments $\lambda_{1,2}$, similar to moments of inertia, so that if the jet is symmetric about its center then Pf ≈ 1. Planar flow is useful in top-quark studies because top jets are relatively symmetric about their center (corresponding to higher values of planar flow), while QCD events are dominated by a single emission (corresponding to a lower value of planar flow). Unfortunately, planar flow weights each constituent according to its transverse momenta relative to the jet axis, so that as the radius of a jet is varied soft radiation towards the edge of a jet begins to dominate and all events are skewed toward higher Pf. To demonstrate this sensitivity and how it can be reduced through the use of subjets, we have included Fig. 5.1, showing the calculation of planar flow at matrix element level, after showering, and after reclustering using subjets. The subjets are formed using the procedure described in Section 5.4 using $R = 0.7$ cones. Here one can see the large corrections to the matrix element results that are attributable to soft radiation. Of course, one can mitigate this effect by using smaller cones (the authors of [108] used $R = 0.4$), as the amount of diffuse soft radiation clustered into the top jet goes roughly as R^2, yet even in this regime the soft corrections can still be significant, especially near Pf ≈ 0.

To be sure, jet shape variables (including planar flow) are very useful and will likely play a role in boosted top chirality measurements. A simple counting exercise shows that after requiring the reconstruction of the W mass, top four-vector, and allowing for axial symmetry, there are still three remaining degrees of freedom encoded in the matrix element that can be mapped out by jet shape variables. However, to simplify the discussion and avoid complicated issues of contamination and higher-order corrections we will use the rest of the paper to focus on quantities calculated using subjets.

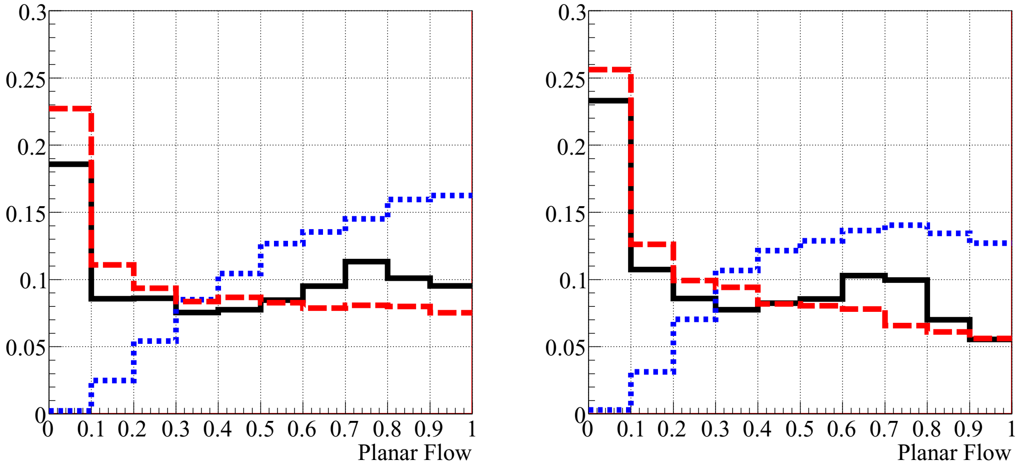

Figure 5.1: Comparison of planar flow for left-handed tops (left figure) and right-handed tops (right figure). For each set of samples we compute the planar flow using the three partonic decay products of the top (black, solid), the constituents of the showered jet (blue, dotted), and three subjets formed from the top-jet constituents (red, dashed). These events are taken from the decay of a 3 TeV Z' into two tops, where we have required the top jet's mass satisfy 140 GeV $< m_J <$ 210 GeV.

5.3 Top Polarimetry With Subjets

We will now explore methods for using subjets to measure the polarization of a collimated hadronic top. In what follows, we will assume we are working with jets tagged as tops, as discussed in [96, 108, 109, 107, 113], and subsequently decomposed into three subjets (a prescription for such a decomposition is given later).

5.3.1 Choosing a Polarimeter

One observable sensitive to the polarization of the top is the distribution of energy among the its three decay products in the lab frame. In the collinear limit, the lab-frame energy fraction of the ith subjet, $z_i = E_i/E_{\text{top}}$, depends only on the energy and angular distributions in the top rest frame, and can serve as a robust variable to measure polarization. While energy fractions are not Lorentz invariant for finite top mass, and in particular are not invariant under longitudinal boosts, frame dependence enters only at order m_t/E_t, and therefore, for highly boosted top quarks, energy fraction variables become fixed, stable quantities [2]. The question then becomes how to select the subjet to be used as a polarimeter.

The most obvious candidate for the job is the b-jet [114, 115], identified either directly through b-tagging or indirectly by first finding the light quarks from the W. However, the identification of the b and W poses some experimental difficulties. Even in isolation, the efficiency of b-tagging drops by a factor of 2–3 at high p_T while light quark rejection is degraded by roughly a factor of 3 [100, 104, 116, 117, 118]. When the b-jet is situated within a collimated top jet, the additional tracks from the neighboring light quark subjets present added complications for b-tagging algorithms.

Another possible method of identifying the b-jet is to do so indirectly, by finding the W. One approach to identifying the W is to look for two jets with an invariant mass within the W mass window. However, the subjet invariant mass distributions are distorted both by contamination from soft radiation and by imperfect subjet reconstruction, as well as by the finite size of the calorimeter. The invariant mass m_{ij} of two nearby subjets is approximately proportional to their separation in R, and for subjets whose centers are separated by $\Delta R_{ij} \lesssim 0.5$, the uncertainty associated with the calorimeter granularity $\delta R \sim 0.1$ can be significant. Distinguishing the correct W subjet pair from amongst the three choices, all of which are typically within a factor of two of each other, then becomes difficult.

Another possible strategy to identify the b-jet is to look for hard splittings within the top jet. As discussed in [96], the energy sharing of a parton branching $A \to BC$,

$$z(A \to BC) \equiv \min(E_B, E_C)/E_A, \tag{5.3}$$

discriminates between hard splittings from decays, $z \sim 0.5$, and soft splittings more

---

[2] Depending on the boost of the top quark, it might also be desirable to consider subjet p_T fractions, as the m_t/E_t corrections to the collinear limit differ for energy and p_T fractions.

characteristic of QCD, $z \sim 0$. If the W decay products were well-separated from the b-jet, one could identify the b by unwinding the clustering of the top jet until there were two subjets and tagging the b as the one with smaller z (so the W subjet would be the one with a harder splitting). Unfortunately, because the W has a mass on the same order as that of the top, the W decay products are not well-separated from the b, so upon unwinding the top jet by one step one often finds that the b-jet has been clustered with a lighter jet from the W decay.

We propose here an alternate subjet selection algorithm, based on k_T distances between subjets, which does not require either b or W identification. While the algorithm is conceptually less straightforward than those based on attempting to identify specific partons within the top jet, it yields a distinct separation between chiralities and is robust under showering and detector effects. Consider the k_T distance measure between two four-momenta i and j,

$$d_{ij} = \min(p_{Ti}^2, p_{Tj}^2) R_{ij}^2, \tag{5.4}$$

where $R_{ij}^2 = (\eta_i - \eta_j)^2 + (\phi_i - \phi_j)^2$. Of the three d_{ij} one can form from the three top subjets, consider the smallest. Our top polarimeter is the energy fraction z_K of the *harder* jet j_K in the minimum k_T distance pair. We plot the distribution of this variable at parton level for different chiralities in Fig. 5.2. The variable shows a clear distinction between right- and left-handed top quarks, with right-handed tops peaked at smaller values of z_K, and left-handed tops preferring larger values of z_K.

5.3.2 Operation of the algorithm

The success of the jet j_K selected by this algorithm as a polarimeter depends on multiple aspects of the angular and energy distributions of daughter partons in polarized top decay, which for reference are reviewed in the Appendix. In order to explain the

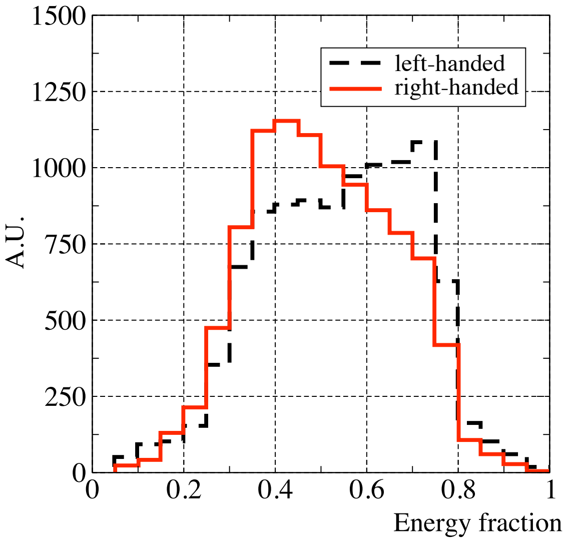

Figure 5.2: Energy fraction z_K of the parton selected by the k_T-based algorithm for different top polarizations. The events shown here correspond to tops produced from a 3 TeV resonance.

success of our polarimeter, we first consider how the algorithm functions at parton level. The identities of the partons picked out by the algorithm differ between right- and left-handed tops. In Fig. 5.3 we break down the contributions to the variable z_K by parton identity.

The anti-down quark is maximally correlated with the top spin, and thus for left-handed tops the d tends to be soft. For left-handed tops the minimum-k_T pair therefore tends to involve the d, and in such pairs the other parton (b or u) is the harder of the two. The algorithm therefore picks out first b quarks, which take a larger fraction of the top energy, and secondarily u's, with d quarks a distant third.

For right-handed tops, where the top energy is shared more equitably among the daughter partons, angular correlations play a more central role. The d-quark is now both more central and harder than predicted by pure phase space (due, again, to its maximal correlation with the top spin). Therefore in order to reconstruct the necessary invariant masses, the ΔR separation between the d and the u and b quarks must be smaller than for pure phase space, and the minimum k_T pair then tends

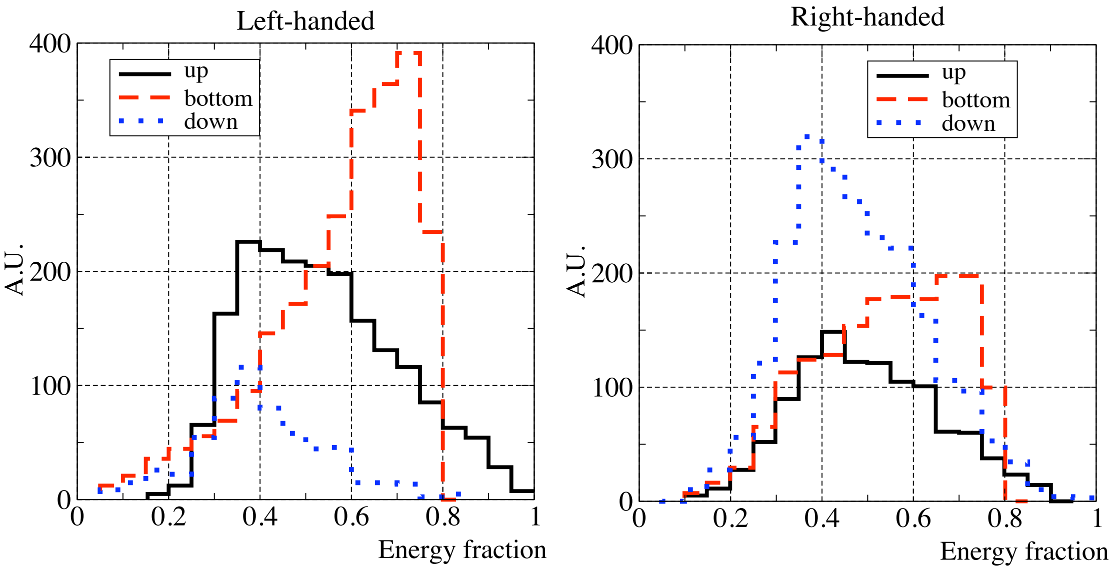

Figure 5.3: Energy fraction of the parton selected by our algorithm, broken down by parton identity. The events shown here correspond to tops produced from a 3 TeV resonance.

to involve the d. For right-handed tops, the algorithm thus dominantly selects the d-quark, as can be seen in Fig. 5.4. While the d is preferentially emitted along the top direction of motion, its energy fraction distribution nonetheless falls off at high energies, as the lab-frame d-quark energy fraction depends on the energy of the d-quark in the top rest frame as well as the angle of emission. The contribution of the b-quark to the variable z_K comes mostly from hard b's recoiling against soft transverse W's.

At high parton energy fraction z_K, the algorithm dominantly selects the hardest parton: b and u for left-handed tops, b and to a lesser extent u, d for right-handed tops. At intermediate energy fractions, the origin of the u and d partons from a common W comes to dominate. The k_T distance between the u and the d is bounded from above, as the u and the d must reconstruct the W. In events without hierarchical energy distributions, the minimum k_T distance thus tends to be between the decay products of the W. Therefore, at intermediate energy fractions, the parton selected by the algorithm is predominantly the d (for right-handed tops) or the u (for left-handed tops). This can be seen already in Fig. 5.3, and is further demonstrated in Fig. 5.4.

Finally, we note that all of these arguments are based upon the assumption that one can go from the collider coordinate system to one oriented around the top direction of motion without significant effects. This assumption does not hold exactly, because the detector geometry is not invariant under rotations around the axis defined by the top direction of motion, and because the k_T algorithm used to select the subjet j_K makes reference to the collider coordinate system through the definition of transverse momentum. Therefore, events which differ from each other only by a rotation around the top axis of motion appear differently both in the detector and in the subjet selection algorithm. Interference terms between right- and left-handed tops generically then do not completely cancel. However, as the magnitude of the interference contribution is determined by the components of the parton momenta transverse to the top momentum, these effects are of order m_t/E_t, a subleading effect for large boosts.

5.3.3 Implementation

To implement this algorithm in practice one must have a technique for finding three subjets within the top jet. The exact procedure one uses to identify the subjets is not important, but for concreteness we detail the method used in our study. One advantage of our subjet-finding technique is that it is easy to implement within the FastJet [119] framework, already used by many studies for top tagging.

The procedure is as follows:

- Cluster the event with a reasonably sized cone ($\Delta R \gtrsim 0.7$) and select a top candidate.
- Take all the cells clustered into the top candidate and recluster them using a smaller cone ($\Delta R \approx 0.2$).

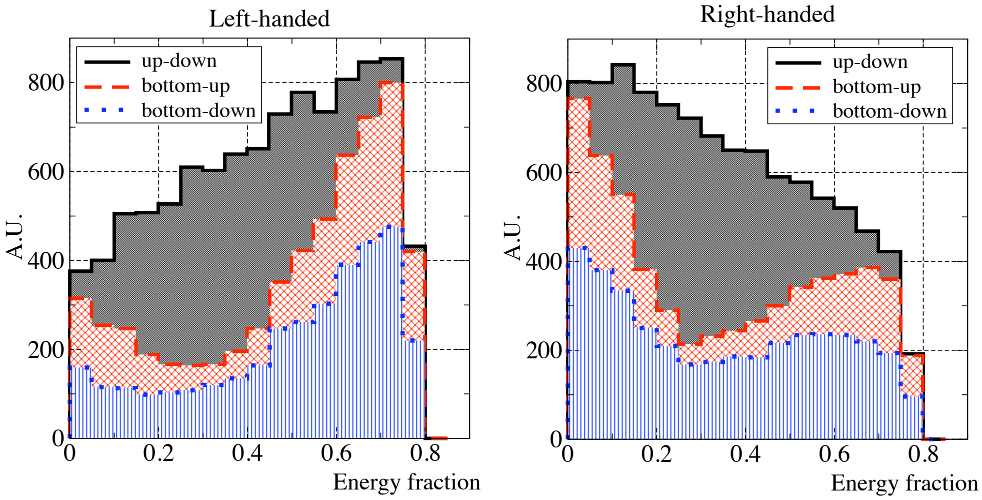

Figure 5.4: Energy fraction of the b quark, broken down according to which two partons in the event belong to the pair with minimum k_T for left-handed tops (left side) and right-handed tops (right side). Note that the contents of the plots are stacked. At high energy fractions, the W and its decay products are soft, and the minimum k_T pair tends to involve one of the W decay products together with the b. At intermediate energy fractions, the minimum k_T pair tends to be the W decay products. At small energy fractions, the b begins to appear as the softer of the two partons in the minimum k_T pair. The effect is more pronounced for right-handed tops, which have a less hierarchical distribution of energy among the three daughter partons. The events shown correspond to tops produced from a 3 TeV resonance.

- Demand that there are at least three subjets, each with a substantial amount of the jet's energy $\gtrsim 1-2\%$. If there are not, split the harder subjet by unwinding [96] it one step using the k_T algorithm, and use the two resulting daughters along with the second hardest subjet from before.

- Now use the four-momenta of the three subjets to find the pair with the smallest k_T distance measure, and compute the ratio of the energy of the more energetic jet in this minimum-k_T pair to the energy of the entire top jet.

Results using this procedure are shown in the next section.

5.4 Examples

We will now apply the subjet-based technique developed in the previous section to some realistic examples. Our goal is to show that the technique works for fully showered events clustered with finite calorimeter cells using a variety of parton shower and hadronization algorithms. It is important to note that we do not consider the shape of background QCD distributions, nor do we consider any shaping effects that might arise from the effects of top tagging. A more complete experimental study would include these effects, but due to the high discriminating power of top tagging algorithms (not to mention other aspects of the event that could be used to remove background) and their relatively high efficiency, we do not expect these effects to be significant.

In what follows, our analysis is performed on events generated at matrix element level using `MadGraph 4.4.17` [120] for physics at the LHC scale (14 TeV). Subsequent showering and hadronization is performed using `Pythia 6.4.21` [121] and `Herwig++ 2.3.2` [122]. When using Pythia, we consider parton showers generated using both virtuality (labeled as Q^2) and p_T ordered showers. Visible final state particles are grouped into 0.1×0.1 calorimeter cells before being clustered into $R = 0.7$ jets using the anti-k_T [123] algorithm. To ensure that the top decayed into visible products (and that no significant radiation was lost outside the cone) we demand that the jet mass exceed 170 GeV. We form subjets by running the anti-k_T algorithm with $R = 0.2$ on the constituents of the top jet, requiring that the third most energetic subjet carry at least 1% of the top jet energy, and splitting the hardest subjet if this condition is not satisfied.

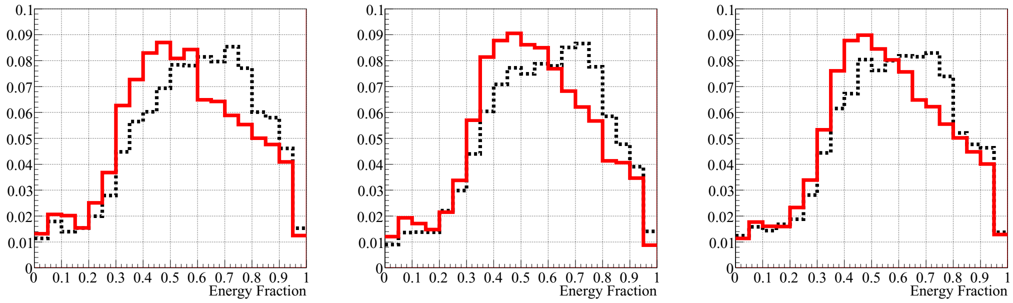

Figure 5.5: Energy fraction of the selected jet for results from (left to right) Herwig++, Pythia-6 (Q^2) and Pythia-6 (p_T). For each plot the solid red and dotted black lines come from right- and left-handed tops, respectively.

5.4.1 Tops from a resonance

We begin by studying a colored octet vector G' with a chiral coupling to the top quark. This model was chosen for simplicity, but it captures the main features of well-motivated scenarios like KK-gluon production. The process under consideration is

$$gg \to G' \to t\bar{t} \tag{5.5}$$

where $m_{G'} = 3$ TeV. The results are shown in Fig. 5.5. One can see from these distributions that the characteristic shapes from matrix element level are unchanged after parton showering and hadronization, demonstrating the robustness of our subjet selection technique.

5.4.2 Tops from cascade decays

Cascade decays of an on-shell top partner (such as a stop squark or a T') to a top plus missing energy are a standard signal of a broad class of well-motivated models. In the presence of multiple sources of missing energy, there is no longer enough information to solve for the rest frame of a leptonically-decaying top quark. Hadronic top quarks, which can be reconstructed independently of the other particles in the event, become

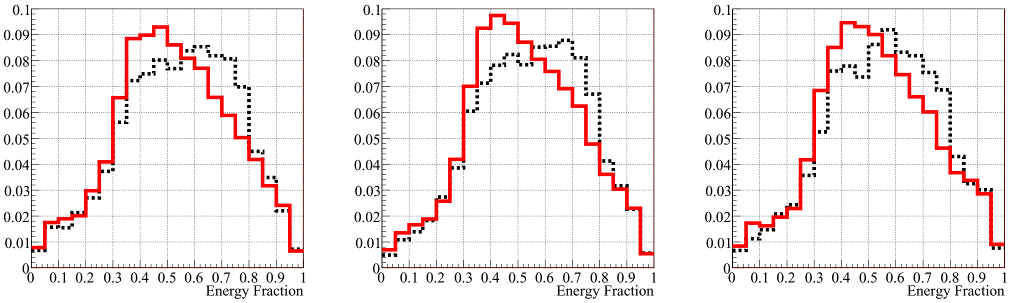

Figure 5.6: Energy fraction of the selected jet for results from (left to right) Herwig++, Pythia-6 (Q^2) and Pythia-6 (p_T). For each plot the solid red and dotted black lines come from right- and left-handed tops, respectively.

a more useful source of information.

For tops produced from an un-reconstructed parent, the observable polarization signal depends on the masses of the new physics particles through the relation of the unknown parent rest frame to the lab frame, as well as through the vertex kinematics [114]. The lack of information about the parent rest frame reduces the observable polarization signal for tops coming from a cascade decay compared to the signal from a resonance. Nonetheless, observable signals are still possible as long as the boost of the top from its parent is dominant, allowing the chiral structure of the top production vertices to be probed.

We consider a model for production of two top partner T' particles decaying into tops and sources of missing energy (labeled A^0). Our choice of spectrum has $m_{T'} = 2$ TeV and $m_{A^0} = 100$ GeV. The results of the analysis performed on the model are seen in Fig. 5.6. As for the G', the distributions agree well with the parton level results and have the same qualitative shapes regardless of the generator used.

5.5 Conclusions

We have proposed an analysis tool useful in determining the chiral structure of the top quark's coupling to new physics. Our method uses subjet-based techniques to probe scenarios where a highly boosted top decays hadronically. This tool requires no assumptions to be made about the production mechanism of the top or about the origin of missing energy in the event, and does not rely upon b-tagging or W reconstruction.

By testing our method on Monte Carlo data from multiple generators using different new physics scenarios we have indicated its robustness against the effects of parton showering and calorimeter segmentation. A more complete analysis would study the shaping of the distributions from the top tagging method using in selecting a sample, but we expect these effects to be small.

Boosted hadronic tops may provide a new window to shed light on otherwise difficult aspects of new physics at the LHC, and will certainly provide a complementary probe of physics beyond the Standard Model. Variables which can analyze the polarization of boosted hadronic tops, such as those introduced here, will fill an important slot in the analysis toolkit as we try to unravel the physics behind LHC data.

Chapter 6

Jet Trimming

Initial state radiation, multiple interactions, and event pileup can contaminate jets and degrade event reconstruction. Here we introduce a procedure, jet trimming, designed to mitigate these sources of contamination in jets initiated by light partons. This procedure is complimentary to existing methods developed for boosted heavy particles. We find that jet trimming can achieve significant improvements in event reconstruction, especially at high energy/luminosity hadron colliders like the LHC.

6.1 Introduction

Jets are collections of hadronic four-momenta used to approximate the kinematics of short distance scattering events. Since the high-energy frontier is explored by hadron colliders with color-rich final states, jets are a necessary tool to better understand the physics of the standard model and probe whatever lies beyond it. To assemble jets one must make use of jet algorithms—well-defined procedures for collecting detector tracks and calorimeter cells into jet four-momenta. Many such algorithms exist, with each exhibiting a different clustering behavior.[1] Though the choice of jet algorithm introduces some level of ambiguity in any jet-based measurement, this is

---

[1] For comprehensive reviews and relevant references see Refs. [124, 125].

still acceptable, as any infrared/collinear-safe jet algorithm will yield results that can be compared to theoretical calculations.

In general, the optimal jet algorithm for an analysis is the one which most closely reconstructs the hard scattering process. The closer the reconstruction is to the true scattering, the greater the signal significance.[2] Now, if the final states observed in a detector only arose from the products of a hard scattering, and if the jets were well-separated from each other and from the beamline, then the precise jet definition used would not matter very much. In that idealized scenario, the jets would be accurately reconstructed by any jet algorithm, as long as the algorithm clustered most of the hadrons arising from final state radiation (FSR).

In reality, however, a detector records more than just the final states from a hard scattering event. The incoming states will typically radiate before scattering, leading to copious initial state radiation (ISR). In addition, multiple parton interactions (MI) and event pileup will further contaminate the final state.[3] This is an especially prominent effect at the Large Hadron Collider (LHC) because of its high energy and luminosity. The net effect is that hadrons from ISR/MI/pileup are spatially overlapped with hadrons from FSR, complicating the jet finding procedure. Thus, there is an inevitable tradeoff. On the one hand, we would like a jet algorithm to form jets large enough to cluster all of the hard scattering decay products and account for wide angle FSR emissions. On the other hand, we are constrained in how large our jets can become by inevitable contamination from hadrons unassociated with the hard scattering.

This conflict between missing radiation and contamination is usually resolved through a judicious choice of the jet size parameter (usually the jet radius R). One can either fix the jet radius at an optimal value, or employ an algorithm designed to

---

[2] In principle, the choice of jet algorithm could also help control reducible backgrounds.

[3] A hard scattering event takes place between the partons of two colliding hadrons. Further interactions between those hadrons are called multiple interactions, while interactions between other hadrons in the colliding bunches are called pileup.

choose the optimal size on a jet-by-jet basis (e.g. the VR algorithm [6]). It is possible to go a step further and statistically account for the sources of contamination by assuming a diffuse distribution and subtracting off a fixed contribution to each jet proportional to its area [126]. However, one can take a more aggressive approach by actively working to identify and remove the radiation contaminating each jet. The basic idea behind such an approach stems from the observation that there is usually only one hard scattering per event; all other sources of radiation (ISR/MI/pileup) are likely to be much softer. By going inside a jet and removing soft radiation (through a modification of the sequential clustering procedure or through the use of subjets), reconstruction can be improved.

This idea of hierarchical radiation and its potential use in cleaning up contaminated jets has gained acceptance in the jet community. In the past, most studies focused on boosted hadronically decaying particles like the W/Z [127, 90], Higgs [95, 128], and top [112, 107, 113, 129],[4] where the procedure is optimized toward improving the jet mass resolution. The only mention that we are aware of for using such a technique outside of heavy object reconstruction is Ref. [132], in which it was observed that applying the same procedure useful in reconstructing a boosted Higgs could also help reconstruct jets from light partons.

In this paper, we present procedures specifically designed to improve the reconstruction of ordinary QCD jets arising from the showering and fragmentation of nearly massless partons (i.e. light quarks and gluons). To distinguish this from prior work on boosted heavy particles (such as jet filtering [95] and jet pruning [113]), we will call our procedures *jet trimming*. In the next section, we will further discuss the contamination of jets and try to quantify its effects. In Sec. 6.3, we will introduce jet trimming algorithms and discuss different versions of these applicable to final states in various kinematical regimes. In Sec. 6.4, we will present the results of our algo-

---

[4] See Refs. [130, 131] for some examples in supersymmetric processes.

rithms and compare them both with the untrimmed results and with earlier cleaning techniques. We will see that by using algorithms specifically designed for light parton jets we can achieve a substantial gain, beyond the improvements seen through applying the techniques developed for boosted heavy particles. Sec. 6.5 contains our conclusions.

6.2 Trimming QCD Jets

As discussed in the introduction, jet reconstruction always presents a trade off between capturing all of the radiation associated with a hard scattering while at the same time minimizing the contamination from other hadrons present in an event. Before we discuss this, let us first introduce some notation and provide some details about our study.

Throughout this paper, we will refer the typical size of a jet in terms of its characteristic radius R using distances defined on the (rapidity y, azimuth ϕ) plane: $\Delta R = \sqrt{(\Delta y)^2 + (\Delta \phi)^2}$. When referring to generic fixed-radius jets and their size (R_0), we are implicitly using the anti-k_T algorithm [123] for jet reconstruction, as this reasonably approximates the behavior of an ideal cone algorithm (for a discussion on the behavior of other algorithms in reconstruction see Ref. [132]). To generate our Monte Carlo events samples we use `Pythia 6.4.21` [121] with the default 'Tune-A' [133, 134] settings and assume a 14 TeV LHC. Our jets are clustered using `FastJet 2.4.0` [119, 135]. While the discussion here in Sec. 6.2 will not account for the effects of pileup (so as to demonstrate the irreducible, significant effects of ISR/MI contamination), we will factor in the effects of pileup for our results in Sec. 6.4, assuming a relatively modest luminosity per bunch-bunch crossing of 0.05 mb^{-1}. To approximate the effects of a real detector, we always group final state partons/hadrons into $\delta\eta \times \delta\phi = 0.1 \times 0.1$ calorimeter cells between $-3 < \eta < 3$, and assign the cells massless

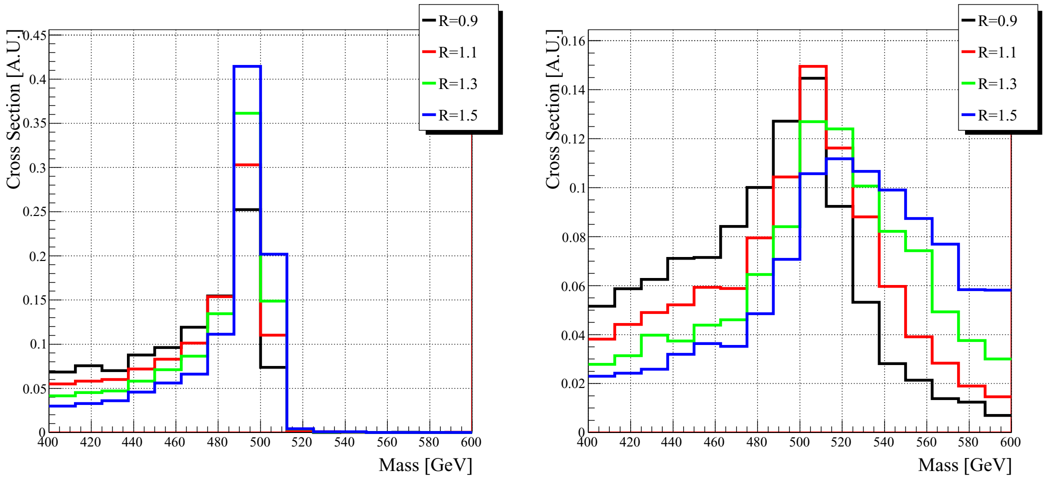

Figure 6.1: Reconstructed $m_\phi = 500$ GeV from $gg \to \phi \to gg$ dijet events with FSR only (left) and with the addition of ISR/MI (right). In the absence of ISR/MI larger jet radii are preferred, while when ISR/MI are turned on a smaller radii must be used to balance the effects of contamination.

four-momenta based on the calorimeter energy.

Finally, we note that while most aspects of particle collisions calculated in Monte Carlo programs rest on firm bases from fundamental physics, the effects of hadronizaton are only understood through phenomenological models.[5] This might seem to be cause for concern, as our results will to some extent reflect the effects of hadronization, but we expect these dependencies to be small, altering perturbatively calculated jet/subjet momenta by $\mathcal{O}(\Lambda_{\mathrm{QCD}})$. While we will operate under this assumption for the rest of the article, the validation of hadronization models will be an important task at the LHC.

6.2.1 The Effects of Contamination

In absence of ISR/MI contamination, a large R is desirable in the context of traditional jet clustering. To see why, consider the process $gg \to \phi \to gg$ where ϕ is a new color

---

[5] Hadronizaton is modeled in Pythia using the Lund model [136], which has been successful in reproducing collider data [137].

	Improvement	R_0	Γ [GeV]	M [GeV]
	$gg \to \phi \to gg$			
All cells	-	1.2	69	518
FSR cells	309%	1.5	15	501
	$q\bar{q} \to \phi \to q\bar{q}$			
All cells	-	0.8	31	505
FSR cells	189%	1.5	11	501

Table 6.1: Improvement in the resonance reconstruction measure Δ presented in Sec. 6.4 in going from standard clustering (*All cells*) to an idealized situation where we only cluster those cells within $\Delta R = 0.2$ of an cell containing more than 1 GeV of FSR (*FSR cells*). Here $m_\phi = 500$ GeV. The definitions of Γ and M appear in Eq. (6.6). Because of the larger color charge of gluons compared to quarks, there is more radiation in the $gg \to \phi \to gg$ case compared to the $q\bar{q} \to \phi \to q\bar{q}$ case, so the potential improvement is correspondingly larger.

octet scalar with a mass of 500 GeV and a narrow width.[6] In a showering Monte Carlo program without hadronization, FSR is factorized from ISR/MI, so one can study the FSR in isolation.[7] On the left side of Fig. 6.1, we show the distribution of the reconstructed ϕ mass using only FSR for various values of the anti-k_T jet radius R_0. One sees that as R_0 increases, the reconstructed invariant mass distribution approaches the narrowly peaked distribution predicted from the hard scattering.

However, when one includes the effect of contamination, larger values of R_0 can yield poorer reconstruction, as seen from the right side of Fig. 6.1. Here, the jet radius that most closely matches the desired peak position is around $R_{\max} = 1.1$, considerably smaller than what one would want to use considering FSR alone. From this one can see that an optimal jet algorithm would be one with a large overall jet radius that somehow avoids clustering in hadrons from ISR/MI (as well as pileup).

Now, there is always a minimum spatial overlap between FSR and ISR/MI from the fact that the two sources of hadrons could end up nearby in the detector. Fortu-

---

[6] The ϕ couples to gluons via the operator $\mathrm{Tr}(\phi G_{\mu\nu} G^{\mu\nu})$. For comparison, we will also consider a different color octet scalar ϕ that couples to fermions via a Yukawa coupling $\bar{q}\phi q$.

[7] With hadronization turned on, there are non-trivial correlations between FSR and ISR.

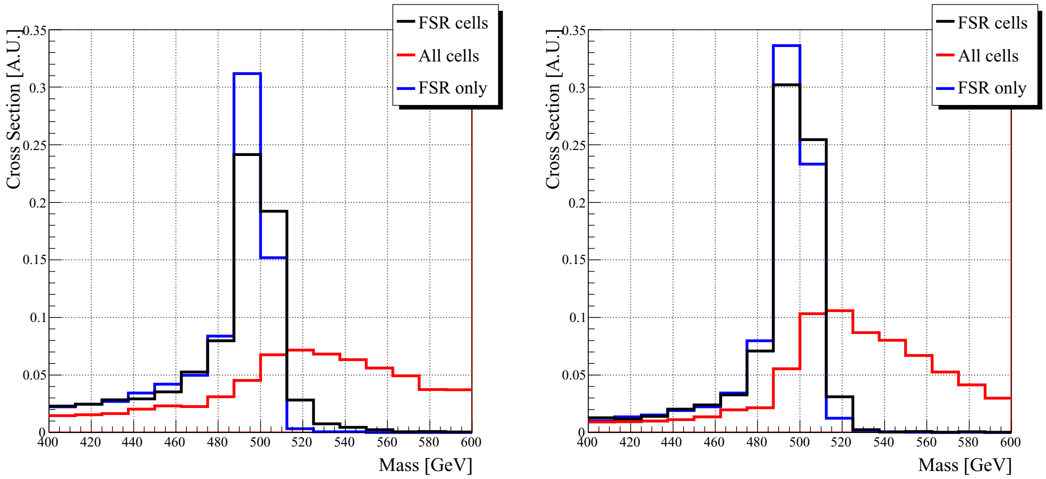

Figure 6.2: Reconstructed $m_\phi = 500$ GeV clustered with $R_0 = 1.5$ for $gg \to \phi \to gg$ (left) and $q\bar{q} \to \phi \to q\bar{q}$ (right). The blue curve shows the reconstruction from a sample without ISR/MI. The red and black curves show data from a sample with ISR/MI, where all cells are clustered (red), and where only those cells within $\Delta R = 0.2$ of an cell containing more than 1 GeV of FSR (black). The similarity between the black and blue peaks demonstrates that considerable gains in reconstruction are possible despite the irreducible overlap in radiation.

nately, this overlap is relatively small. In Fig. 6.2 we present the ϕ mass reconstructed using $R_0 = 1.5$ where only those calorimeter cells within $\Delta R = 0.2$ [8] of one containing at least 1 GeV of FSR were clustered, along with the distribution obtained without this restriction. The restricted distribution is quite close to the one where only FSR was clustered, confirming the minimum spatial overlap. By considering this sort of restriction to FSR-heavy cells, one can calculate the maximum possible reconstruction improvement in going from ordinary cones to such an idealized jet algorithm. This is shown in Table 6.1, where the improvement is measured by the reconstruction measure Δ presented in Sec. 6.4. We see potential improvements of up to 3× in reconstruction. Of course, such an idealized jet algorithm cannot exist since no physical observable can distinguish between FSR and ISR/MI, but the room for improvement is compelling.

---

[8] While at this point the choice of $\Delta R = 0.2$ is somewhat arbitrary, later in Sec. 6.4 we will see that this is a reasonable subjet radius for use in trimming.

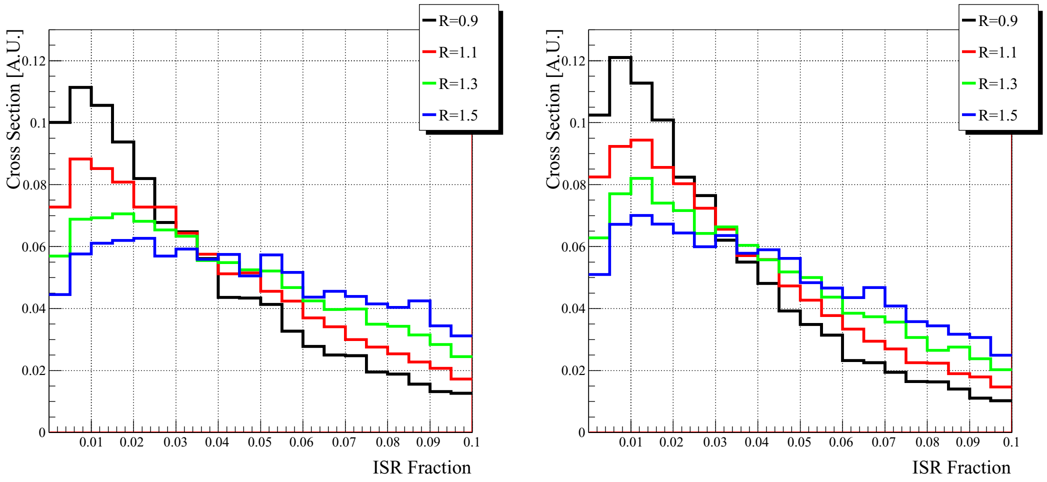

Figure 6.3: Fraction of a jet's p_T attributable to ISR/MI for $gg \to \phi \to gg$ (left) and $q\bar{q} \to \phi \to q\bar{q}$ (right).

The goal our jet trimming algorithm is to approach this ideal reconstruction as closely as possible. To do so, we need some kind of criteria to determine whether a given patch of the calorimeter is likely to contain substantial amounts of FSR. In light of the observation that ISR/MI (as well as pileup) is usually soft compared to FSR, the simplest possible criteria we have is relative transverse momentum. As shown in Fig. 6.3, in a typical jet ISR/MI makes up only $\mathcal{O}(1-5\%)$ of the jet's p_T (the contribution of pileup is a luminosity dependent question), and we saw earlier that there is minimal spatial overlap between contamination and FSR. Therefore, sources of contamination can be mitigated by simply removing patches of soft calorimeter cells.

6.2.2 QCD Jets vs. Boosted Objects

While the general idea of removing soft calorimeter cells is straightforward, a number of details remain unspecified. At minimum, one wants to consider patches of calorimeter cells by clustering them into subjets of radius $R_{\text{sub}} > \delta_{\text{cal}} = 0.1$ to remove any sensitivity of the procedure to calorimeter segmentation. Beyond that, one must specify how the subjets are to be formed, how large they will be, and what will serve as the criterion for softness. As we will argue, by choosing jet trimming parameters in a way designed to enhance the reconstruction of light parton jets, we can increase reconstruction performance beyond the current techniques designed for boosted heavy particles [127, 90, 95, 128, 112, 107, 113, 129, 130, 131].

To see how one might go about choosing trimming parameters, consider first how they would be chosen to reconstruct the jet from a boosted heavy particle. Usually such a particle decays immediately into two (e.g. the Higgs or W/Z) or three (e.g. the top) final states, each at the same characteristic p_T scale (barring a matrix element conspiracy). These states will shower into distinct hard patches in the jet (see the left panel of Fig. 6.4), so one can hope to remove contamination from the system by simply associating a subjet to each hard final state and discarding everything else. That is, one would discard all but the N_{cut} hardest subjets. Whether or not a particular subjet from a boosted heavy particle is considered soft depends upon where the subjet ranks in the subjet p_T ordering and upon how many final state partons we expect in the decay. For instance, if we are looking to reconstruct a Higgs in its decay $h \to b\bar{b}$ we would form subjets inside the initial jet and discard all but the hardest two.[9] In this context, the natural size of a subjet is also relatively clear; to treat each final state of the decay equally (as we should, since they have comparable p_Ts) we are limited to $R_{\mathrm{sub}} \lesssim R_0/2$ under the assumption that the initial jet was chosen to be just large enough to encompass the entire decay of the heavy particle.

The situation changes when we consider jets from light quarks or gluons (compare the two panels in Fig. 6.4). The first difference is that there is only one hard final state at lowest order in α_s. Softness is therefore more naturally established directly via a cut on subjet p_T rather than by restricting to a fixed number of subjets. Later we will establish different subjet p_T cuts for different kinematic regimes. The second

---

[9] Sometimes analyses allow for one subjet beyond the minimum number of tree level final states in order to capture the first emission [95], but the principle remains the same.

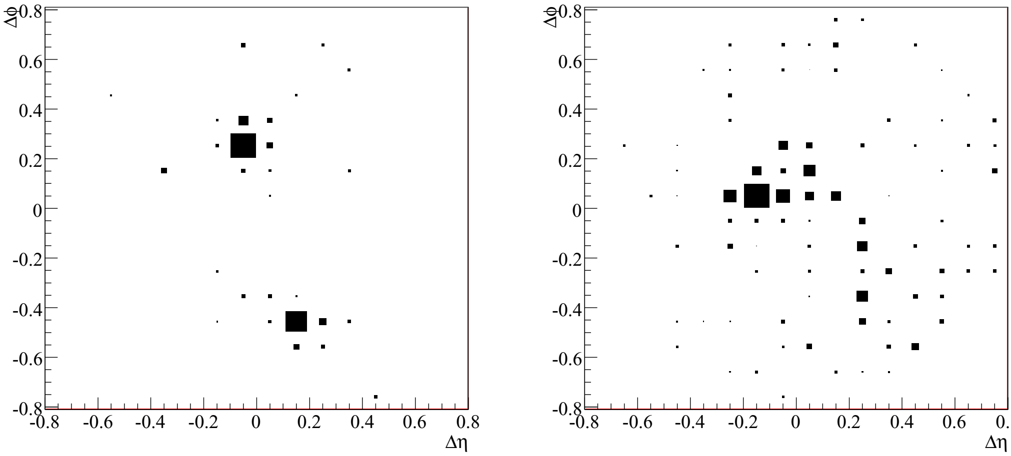

Figure 6.4: Comparison of a jet formed from the decay of a boosted heavy particle (left) with one from the showering of light flavor/gluons (right). Specifically, the left hand panel shows the jet formed from $h \to b\bar{b}$ while the right is a gluon jet. The $(x,\, y)$-axes are $(y,\, \phi)$-distances as measured from the jet center and the area of each calorimeter cell is proportional to its p_T.

difference is that there is no natural size for the subjets as this depends upon the the p_T cut for the subjets; a larger/smaller subjet size will necessitate a harder/softer subjet p_T cut. With these two differences in mind, we can now define our jet trimming procedure.

6.3 Implementation

In this section, we present an explicit algorithm implementing the jet trimming technique outlined above.[10] Our choice of algorithm is motivated primarily by simplicity and the ability to re-use existing jet finding procedures. Many more sophisticated choices could easily be imagined, but these are beyond the scope of the present work.

Since our jet trimming procedure will make use of well-known sequential recombination jet algorithms, we will briefly review how these work. Recall that in a recursive

---

[10] Our implementation is available as a plug-in to the `FastJet` package [119, 135], which is available from the authors upon request.

jet algorithm one begins with an initial set of four-momenta (these could be tracks, calorimeter cells, etc.), assigning every pair a "jet-jet distance measure" d_{ij} and every individual four-momenta a "jet-beam distance measure" d_{iB}. The distance measures relevant for our study are:[11]

$$\text{anti-}k_T\ [123]: \qquad d_{ij} = \frac{1}{\max\left[p_{Ti}^2, p_{Tj}^2\right]}\frac{R_{ij}^2}{R_0^2}, \qquad d_{iB} = \frac{1}{p_{Ti}^2}, \tag{6.1}$$

$$\text{C/A}\ [93,\ 94]: \qquad d_{ij} = \frac{R_{ij}^2}{R_0^2}, \qquad d_{iB} = 1, \tag{6.2}$$

$$k_T\ [91,\ 92]: \qquad d_{ij} = \min\left[p_{Ti}^2, p_{Tj}^2\right]\frac{R_{ij}^2}{R_0^2}, \qquad d_{iB} = p_{Ti}^2 \tag{6.3}$$

$$\text{VR}\ [6]: \qquad d_{ij} = \frac{1}{\max\left[p_{Ti}^2, p_{Tj}^2\right]}R_{ij}^2, \qquad d_{iB} = \frac{\rho^2}{p_{Ti}^4}. \tag{6.4}$$

At each step in the clustering, the smallest entry in the set of all d_{ij} and d_{iB} is identified. When a jet-jet distance is the smallest, the corresponding four-momenta are merged, while if a jet-beam distance is the smallest, then the associated four-momentum is "merged with the beam" and set aside. Here we will deal entirely with inclusive algorithms, where the recursion continues until all jets are merged with the beam, and the algorithm returns those merged jets whose p_T is greater than some minimum value.[12]

6.3.1 Jet Trimming

The jet trimming procedure we advocate is an "outside-in" algorithm, meaning that a seed jet determined through one jet finding method is reclustered using a subjet finding method. Then a softness criteria is applied to the individual subjets to determine the final trimmed jet. One could also imagine an "inside-out" algorithm, where small subjets are found first, and clustering into a larger jet, again using some kind

---

[11] For jet algorithm aficionados, we use "VR" to refer to the "AKT-VR" algorithm of Ref. [6].

[12] In an exclusive algorithm, the recursion stops when a predetermined distance measure d_{cut} is reached, at which point the unmerged jets are returned.

of softness criteria, but we will not explore that option here.

The proposed algorithm proceeds as follows:

1. Cluster all cells/tracks into jets using any clustering algorithm. The resulting jets are called the seed jets.
2. Within each seed jet, recluster the constituents using a (possibly different) jet algorithm into subjets with a characteristic radius R_{sub} smaller than that of the seed jet.
3. Consider each subjet, and discard the contributions of subjet i to the associated seed jet if $p_{Ti} < f_{\text{cut}} \cdot \Lambda_{\text{hard}}$, where f_{cut} is a fixed dimensionless parameter, and Λ_{hard} is some hard scale chosen depending upon the kinematics of the event.
4. Assemble the remaining subjets into the trimmed jet.

This procedure is illustrated in Figs. 6.5 and 6.6. The dimensionless parameter f_{cut} quantifies the expected p_T scale hierarchy between FSR and ISR/MI/pileup. In principle, this procedure could be iterated such that subjets that fail the softness criteria in one seed jet could be tested for inclusion in a different seed jet. However, this is only relevant if the original jets were effectively overlapping, or if the removal of subjets substantially changes the position of the trimmed jets relative to the original seed jets.

The precise jet definition used in step 1 is largely irrelevant for the jet trimming procedure. In Sec. 6.4, we will trim two different jet algorithms, anti-k_T [123] and VR [6], finding improvements in reconstruction with both.

The jet definition used in step 2, however, is more important as it determines how the subjets are found. We use the k_T algorithm [91, 92] rather than a Cambridge-Aachen [93, 94] or anti-k_T algorithm [123], because subjets formed by the k_T algorithm tend to better share the energy between subjets. That is, imagine that the dominant

FSR depositions in a seed jet cannot be contained within a single subjet of size R_{sub}. In such circumstances the anti-k_T algorithm, which clusters radiation from hardest to softest, will tend to create imbalanced subjets by allocating most of the energy to one subjet, making it more likely that the weaker subjet will be discarded when the softness criteria is applied. As the k_T algorithm clusters from softest to hardest, it is more likely to yield a equitable distribution of energy between the subjet that contain FSR, making them less likely to be discarded by the trimming procedure.

Finally, we must select a Λ_{hard} to set our criterion of hardness when judging a subjet's p_T. This is a non-trivial choice, as different kinematical configurations call for different scales, and the difference in reconstruction from different scale choices can be large. To illustrate this, in Sec. 6.4 we will present two possibilities for Λ_{hard}: the seed jet's p_T, and the effective mass of the event (i.e. the scalar sum of the transverse momenta: $H = \sum p_T$). While we have only considered the simplest two scale choices, it would be interesting to investigate more complicated methods to see if additional gains could be realized.

6.3.2 Comparison to Previous Methods

As argued before, most techniques useful in removing contamination from the jets of boosted heavy particles keep a fixed number N_{cut} of hard subjets. To enable an apples-to-apples comparison of f_{cut} vs. N_{cut}, we will simply take the jet trimming algorithm above, replacing step 3 with:

3. Sort the subjets according to p_T and discard the contributions of those softer than the N_{cut}-th hardest subjet.

This allows us to employ a condensed notation in discussing various trimming procedures. We can denote different algorithms by

$$\text{alg}(\{f, N\}, \{p_T, H\}), \tag{6.5}$$

where "alg" is the algorithm used to make the seed jets (here anti-k_T or VR), $\{f, N\}$ specifies whether we will trim all subjets with a p_T below $f_{\text{cut}} \cdot \Lambda_{\text{hard}}$ or include only the N_{cut} hardest subjets, and the final entry (only relevant for f_{cut} algorithms) species whether we will use the p_T of the seed jet or the effective mass of the event to set Λ_{hard}.

In addition to this fixed N_{cut} algorithm—which we believe represents the most advantageous application of previous techniques for boosted objects to the study of light parton jets—we will also include a direct implementation of an algorithm from an earlier study. We will present results using the jet filtering technique of Ref. [95] (labelled *Filtering* below) which takes a jet and only includes those constituents that fit into the two hardest C/A subjets formed from cones of size $R_0/2$.

We were also interested in testing the jet pruning procedure of Ref. [113], since it could be considered as something of a middle ground between trimming and the cleaning methods that cut on a fixed number of subjets.[13] Pruning functions by attempting to remove spurious mergings in the clustering sequence: after a seed jet is formed, its constituents are reclustered using the k_T or C/A algorithm, and if the jet algorithm attempts to merge widely separated ($\Delta R > 2R_P m_J/p_T$) four-momenta with a large p_T hierarchy ($z < z_{\text{cut}}$)[14] then the merging is rejected, and the softer of the two four-momenta deleted. Pruning is most effective at removing spurious mergings from the later stages of clustering (i.e. right before the jet is complete), which is precisely what it should do to reconstruct a boosted heavy particle.

However, in our studies on pruning light quark jets we found at best only a marginal improvement in reconstruction. This occurred when the optimized value of R_P was essentially zero, meaning that the z_{cut} criteria was being applied at every stage of the reconstruction.[15] We suspect that the reason pruning is not working well

---

[13] The implementation of pruning we tested was `FastPrune 0.3.0` [138].

[14] Here $z = \min[p_{T_a}, p_{T_b}]/p_{T_{\text{tot}}}$ for four-momenta p_a and p_b with $p_{\text{tot}} = p_a + p_b$.

[15] Because the improvements we see with pruning are small, and occur at parameters at which the procedure is uncomfortably sensitive to the calorimeter segmentation, we will not report them in

in this context is that far enough down the line in the parton shower, there is no longer a clear scale separation between FSR and contamination. So while pruning employs a relative p_T cut (as in jet trimming), it appears to be most effective when employed on a jet with a fixed, small number of hard subjets. It is an open question whether pruning techniques might be modified to successfully clean light quark jets.

6.4 Results

We now apply the above jet trimming procedure to two examples in different kinematic regimes: heavy resonance reconstruction, and a two-step decay chain. Our goal is justify the use of trimming, show that it is advantageous to use a trimming procedure specifically designed for jets from light partons, and to see how different measures of Λ_{hard} can change the reconstruction of the trimmed event. Unlike Sec. 6.2, here we will include both the effects of ISR/MI and event pileup.

In both examples, we will find that employing any sort of trimming procedure leads to an improvement in reconstruction. However, in going from an algorithm designed for boosted heavy particles to one specifically aimed at light parton jets, we can realize significant additional gains. Further, using a measure of hardness well suited to the kinematics of an event can make almost as big a difference in reconstruction as to the decision to trim in the first place.

Our results confirm our intuitions from Sec. 6.2 that trimming partially resolves the jet-size/contamination tradeoff. For the anti-k_T algorithms, the optimal R_0 value in the trimmed sample is systematically larger than the optimal R_0 value in the untrimmed sample. Similar conclusions hold for VR, with the jet size parameter ρ being larger in the trimmed samples.[16] We will find that background dijet distributions are not increased through the use of a large initial radius, and may even be

---

the next section.

[16] In VR algorithms, the radius of a jet is approximately $R \approx \rho/p_T$, where p_T is the jet's transverse momentum.

reduced in some cases. Finally, as expected, the active jet area [126] is substantially smaller in the trimmed sample.

To quantify reconstruction performance, we will fit reconstructed invariant mass distributions to a sum of two distributions (similar to what was done in Ref. [113]):

$$S(m) = \alpha \left[\frac{1 + \beta(m - M)}{(m^2 - M^2)^2 + \Gamma^2 M^2} \right], \tag{6.6}$$

$$B(m) = \delta + \gamma/m, \tag{6.7}$$

where δ and γ are restricted to be ≥ 0. Here $S(m)$ is a skewed Breit-Wigner distribution and $B(m)$ is a background-like falling distribution. We quantify signal reconstruction via the measure

$$\Delta \equiv S(M) = \frac{\alpha}{\Gamma^2 M^2}, \tag{6.8}$$

i.e. the peak height of the $S(m)$ curve. While other measures of reconstruction performance would be equally reasonable, this measure favors algorithms reconstructing a tall $S(m)$ of narrow width, and has the advantage of not introducing any arbitrary parameters beyond the fitted functional form. Note that this reconstruction measure does not attempt to reward algorithms that get the right peak position, and we will see a corresponding systematic invariant mass shift in using trimmed jets.

For simplicity of discussion, we only consider processes with initial/final state gluons. From Table 6.1, we see that improvements are certainly possible when these are replaced with light quarks, and all of our conclusions regarding the optimal trimming method will hold there as well. It is important to remember, though, that quarks have a lower effective color charge then gluons and thus produce less QCD radiation. Thus, for light quarks one expects (and we found) a diminished optimal untrimmed jet radius and a lower potential improvement achievable through trimming.

	Improvement	f_{cut}, N_{cut}	R_{sub}	R_0, ρ	Γ [GeV]	M [GeV]
anti-k_T	-	-	-	1.0^*	71	522
anti-k_T (N)	40%	5^*	0.2^*	1.5^*	62	499
anti-k_T (f, p_T)	59%	$3 \times 10^{-2*}$	0.2	1.5	52	475
anti-k_T (f, H)	61%	$1 \times 10^{-2*}$	0.2	1.5	50	478
VR	30%	-	-	200^* GeV	62	511
VR (N)	53%	5	0.2	275^* GeV	53	498
VR (f, p_T)	68%	3×10^{-2}	0.2	300^* GeV	49	475
VR (f, H)	73%	1×10^{-2}	0.2	300^* GeV	47	478
Filtering	27%	2	$R_0/2$	1.3^*	61	515

Table 6.2: Comparison of dijet resonance reconstruction using trimmed and untrimmed algorithms. The first column specifies the algorithm, the second lists the change in Δ over untrimmed anti-k_T (second row), the third lists the relevant trimming parameters, the fourth contains the subjet radius, the fifth the seed jet parameters, the sixth the fitted width, and the seventh the fitted mass. For each algorithm, we have optimized those parameters denoted by a *, while the rest have remained fixed.

Finally, one should keep in mind that while the improvements we find are the result of well understood physical effects, the precise values of the trimming parameters will change somewhat when the Monte Carlo tuning is adjusted to account for LHC data. Thus, while the parameters below will provide a reasonable guide to what should be used at the LHC, the exact values will need to be inferred from a iterative process of Monte Carlo tuning to standard candles.

6.4.1 Heavy Resonance Decays

The simplest test of a jet algorithm is how it reconstructs a heavy resonance decaying to the two jets. As in Sec. 6.2, we use the process $gg \to \phi \to gg$ where ϕ is a color octet scalar with $m_\phi = 500$ GeV.

The results of this reconstruction are presented in Table 6.2. Here we are interested primarily in two different comparisons: untrimmed algorithms versus those trimmed using an f_{cut} (so as to measure the full potential for improvement in reconstruction), and those trimmed using an N_{cut} to those using an f_{cut}. Now, the more parameter choices one optimizes in an algorithm the more that algorithm stands to gain from arbitrary statistical fluctuations. To guard against this and ensure that the first comparison above is fair, we fully optimize the anti-k_T (N) algorithm, using the resulting best choices of R_{sub} and R_0 as inputs to our optimization of anti-k_T (f), for which we only optimize a single parameter: f_{cut}. The result is a fair comparison of untrimmed algorithms to those trimmed with an f_{cut}, and a comparison of N_{cut} to f_{cut} trimming where N_{cut} trimming is given a statistical advantage.[17]

Several algorithms and trimming procedures are presented in Table 6.2. We have included untrimmed anti-k_T, anti-k_T with a cut on the momenta of k_T subjets (set relative to both the jet's p_T and the event's effective mass), anti-k_T with a fixed number of k_T subjets, and for comparison with previous techniques anti-k_T with two C/A subjets of half the seed jet radius (i.e. the filtering procedure of Ref. [95]). Both trimmed and untrimmed VR jets are also included. In Fig. 6.7, we display the reconstructed ϕ mass using both trimmed and untrimmed anti-k_T and VR algorithms.

We see that trimming of any sort is useful in reconstruction. However, the difference between trimming techniques is apparent. By using an algorithm with a p_T cut determined as a fraction of the original p_T (i.e. the samples whose trimming is parameterized by an f_{cut}) we are able to see significant gains beyond what is possible using a fixed number of subjets. This reflects the fact that the structure of the jet from a light parton is not known a-priori, unlike the jets from boosted heavy particles, so it is advantageous to trim with a direct subjet p_T cut. We further note that at this stage, the difference between using H and p_T to set Λ_{hard} makes only a small difference in reconstruction, reflecting the fact that for dijet events $p_T \approx H/2$. Below, we will see that the situation will change in more complicated event topologies.

Before continuing, we remark that in Fig. 6.7, the dijet invariant mass distribution

---

[17] For the VR algorithms we will take the anti-k_T optimized R_0, f_{cut}, and N_{cut} as inputs (R_0 will set R_{max}) and optimize the ρ parameter.

is systematically shifted to lower values through the effects of jet trimming. This is to be expected, given that the trimming procedure will necessarily result in some accidental removal of FSR. To understand the size of the effect, note that in Table 6.2 we find an optimized f_{cut} of around 3% when we cut on the subjet's p_T relative to that of the seed jet, and that the optimal N_{cut} for fixed-number cleaning is 5. Since the pattern of QCD radiation from a light parton ensures us that the subjets follow a strong p_T hierarchy, we should only expect one or two subjets to be slightly below the 3% p_T cut we have imposed. This is enough to account for the roughly 5% shift in M that we observe.

6.4.2 Longer Decay Chains

Next, we consider the production channel $gg \to X \to YY \to gggg$ where $m_X = 1$ TeV and $m_Y = 300$ GeV. This sample is qualitatively different from the dijet reconstruction in two ways: the final state is more crowded, and the final state jets can vary widely in p_T within the same event. The results from this reconstruction are presented in Table 6.3, and the resulting m_X and m_Y distributions are plotted in Fig. 6.8 and Fig. 6.9, respectively.

That the final state is crowded somewhat limits the improvements achievable from trimming. We saw before in Table 6.2 that trimming seemed to work well when the seed jets were allowed to grow much larger than the optimized untrimmed jets. Here, the untrimmed jets are optimized at $R_0 = 0.8$, so the trimmed jets cannot grow much larger without merging with each other and ruining the reconstruction. Despite this limitation, however, we see that valuable improvements are still possible.

More importantly, now we see that the choice of Λ_{hard} can make a significant difference in reconstruction. When Λ_{hard} is chosen to be the effective mass of the event, reconstruction is improved beyond the case where Λ_{hard} is the seed jet p_T (the improvement roughly doubles). This is because when we let the seed jet p_T

	Improvement	f_{cut}, N_{cut}	R_{sub}	R_0, ρ	Γ [GeV]	M [GeV]
anti-k_T	-	-	-	0.8^*	158	994
anti-k_T (N)	12%	5^*	0.2^*	1.0^*	115	969
anti-k_T (f, p_T)	10%	$3 \times 10^{-2*}$	0.2	1.0	108	941
anti-k_T (f, H)	19%	$5 \times 10^{-3*}$	0.2	1.0	100	944
VR	10%	-	-	150^* GeV	157	979
VR (N)	17%	5	0.2	275^* GeV	115	965
VR (f, p_T)	16%	3×10^{-2}	0.2	225^* GeV	112	938
VR (f, H)	22%	5×10^{-3}	0.2	300^* GeV	101	942
Filtering	6%	2	$R_0/2$	0.9^*	128	969

Table 6.3: Comparison of the 2 → 4 resonance reconstruction using trimmed and untrimmed algorithms. Reconstruction is performed by taking the invariant mass of the hardest four jets. The first column specifies the algorithm, the second lists the change in Δ over untrimmed anti-k_T (second row), the third lists the trimming parameters, the fourth contains the subjet radius, the fifth the seed jet parameters, the sixth the fitted width, and the seventh the fitted mass. For each algorithm we have optimized those parameters denoted by a *, while the rest have remained fixed.

determine the hard scale for each jet while using a fixed f_{cut}, the softer jets will see little trimming (because the minimum subjet p_T is soft), while for the same reason the harder jets will see too much trimming. The resolution, it seems, is to simply use a global p_T cutoff for each event when the signal jets are of different characteristic p_T scales.

6.4.3 Dijet Backgrounds

The improvements in signal reconstruction seen so far would be of little use if jet trimming significantly increased the background as well. After all, to see improvements in signal reconstruction we must let our seed jets cluster with a large radius, and it is possible that this could result in an unintended rise in the background distributions.

Fortunately, this does not seem to be the case. In Fig. 6.10 we present the background QCD dijet invariant mass distributions clustered using the parameters of Table 6.2 optimized for signal reconstruction. If anything, we see that the trimmed distributions are shifted to lower invariant mass values than the untrimmed distributions. This is especially useful in the case of the VR jet algorithm, which on its own can distort background distributions to higher values.[18] It is tempting to argue from this that trimming can also be useful in reducing the background, but one should be careful drawing such a conclusion as the signal position also shifts. The precise signal and background interplay, while intriguing, is therefore likely to be highly process dependent, and requires a dedicated study.

6.4.4 Jet Area

In Fig. 6.2, we argued that the overlap of ISR/MI with FSR was minimal, so even though the naive area of the jets employed in our analysis is quite large, there should not be significant sensitivity to the effects of ISR/MI/pileup that we set out to avoid. We can quantify this statement using the catchment area of a jet [126], allowing us to directly measure the sensitivity of the trimmed jet to uniform diffuse contamination. We find that while the jets we use in trimming start with large areas, after the jet trimming procedure is applied the active area decreases dramatically, as shown in Fig. 6.11. In fact, the active area after trimming is even less than that of the untrimmed jet which began with a smaller radius.

One caution, however, is that the catchment area only captures the sensitivity to soft contamination. Trimming cannot guard against a fluctuation of ISR/MI/pileup that yields a hard subjet above the f_{cut} threshold. In some ways, trimming accentuates such fluctuations, since the contamination cannot be averaged over a larger jet area and subtracted statistically using, e.g. the methods of Ref. [126]. Therefore, more detailed studies are needed to really understand such systematic biases.

---

[18] In Ref. [6] we had to impose a jet-quality cut to prevent this distortion. With jet trimming, it seems that such a cut is unnecessary.

6.5 Conclusions

In this paper, we have proposed jet trimming as a way to improve jet reconstruction by mitigating the spatial overlap between FSR and ISR/MI/pileup in hadronic collisions. This technique actively removes sources of contamination by exploiting the difference in scale between the hard emissions of FSR and the relatively soft emissions from ISR/MI/pileup. While prior efforts had been made along similar lines, those efforts focused on removing contamination from the jets of heavy boosted objects. We have shown that light parton jets benefit from methods that emphasize relative subjet p_T instead of the number of subjets.

We presented an explicit algorithm that implements jet trimming. Our algorithm begins with seed jets constructed through any means (here we employ anti-k_T and VR), which are then reclustered using an inclusive k_T algorithm and trimmed according to a subjet p_T cut set relative to some hard scale determined by the kinematics of the event. In two different kinematic configurations, we find large improvements in reconstruction efficiency from using trimmed jets. Moreover, unlike our previous VR algorithm [6], this improvement was obtained without a drastic increase in the catchment area of the jet.

Further study is necessary to understand how this jet trimming procedure would affect jet systematic errors in an actual experimental context. For example, jet energy scale systematics already require a correction from ISR/MI/pileup contamination, and exactly how a jet energy correction would be applied in the case of trimmed jets is unclear. However, by addressing ISR/MI/pileup contamination on a jet-by-jet basis, we expect that the systematic uncertainty associated with trimmed jets should not be any worse than for fixed-radius jets. Moreover, it would be interesting to see whether the systematic shift in the invariant mass peak from accidentally throwing away FSR subjets could be fixed through a simple jet energy rescaling.

Finally, while the improvement in reconstruction from trimming is already quite helpful, it is nowhere near the in-principle improvement we saw in Sec. 6.2. Perhaps further advances can be made through a better choice of the Λ_{hard} parameter or a different subjet finding procedure. Whether any jet trimming algorithm can ever hope to approach the theoretical limit in ISR/MI/pileup rejection is an important open question, but the gains already seen in a simple trimming algorithm recommend its use at the LHC.

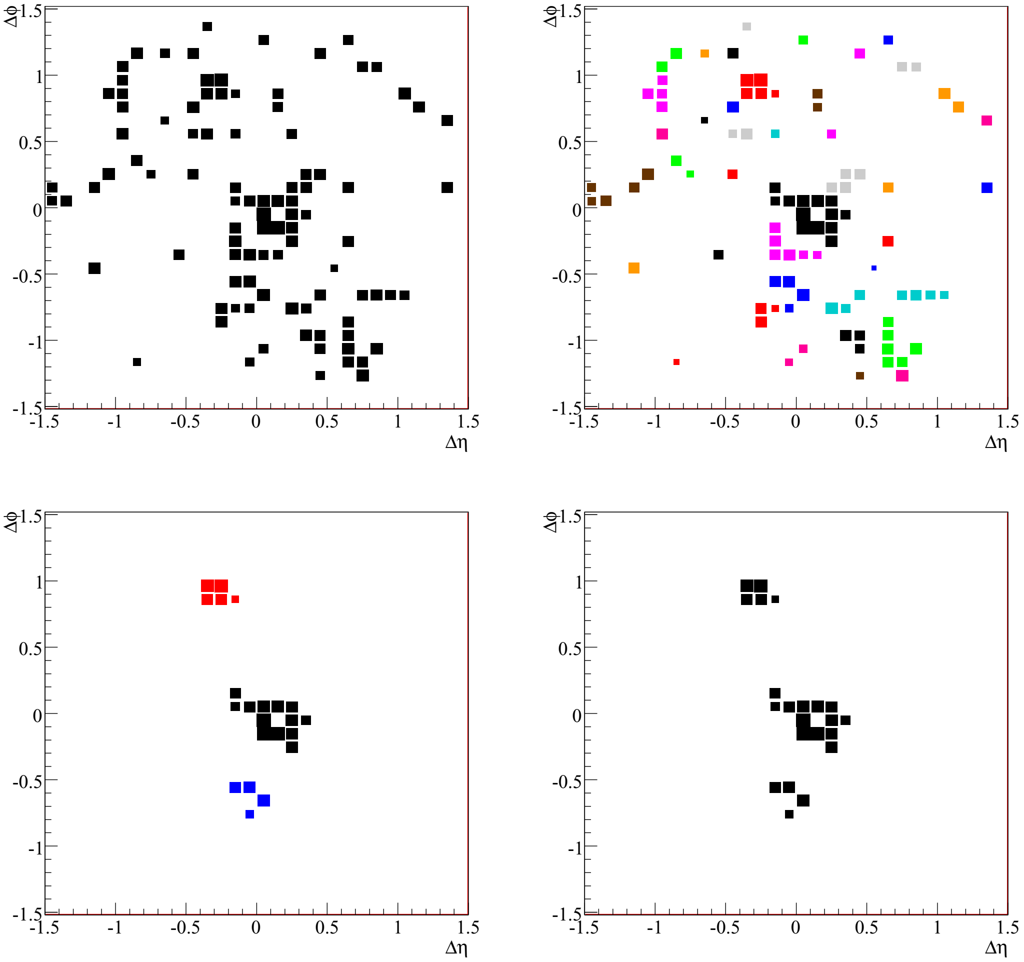

Figure 6.5: Step by step illustration of the jet trimming procedure. Proceeding from left to right, top to bottom, we show a jet as initially clustered (using anti-k_T with $R_0 = 1.5$), the constituent k_T subjets with $R_{\mathrm{sub}} = 0.2$, the subjets surviving the $p_{Ti} < f_{\mathrm{cut}} \cdot p_T$ cut (where $f_{\mathrm{cut}} = 0.03$), and the final trimmed jet. To make the figure easier to read, the area of each cell is proportional to the log of the cell's p_T.

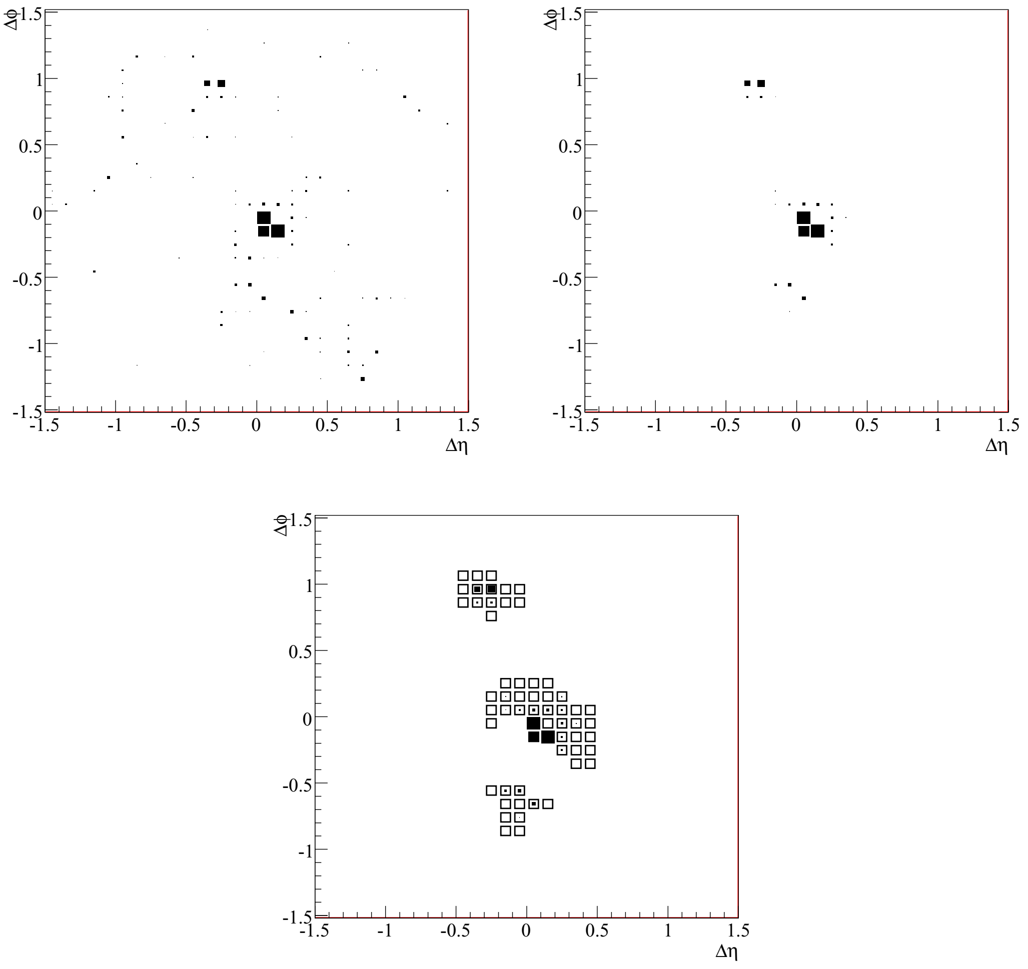

Figure 6.6: The jet of Fig. 6.5 before (top left) and after (top right) trimming using a linear scale where a cell's area is proportional to its p_T. Also shown in the lower panel is the catchment area of the jet [126], where the empty black squares indicate cells that would have been clustered in the final trimmed jet if all cells were given an infinitesimal amount of radiation. As we will discuss more in Sec. 6.4.4, the jet's area has been dramatically reduced, here to around 8% of its untrimmed value.

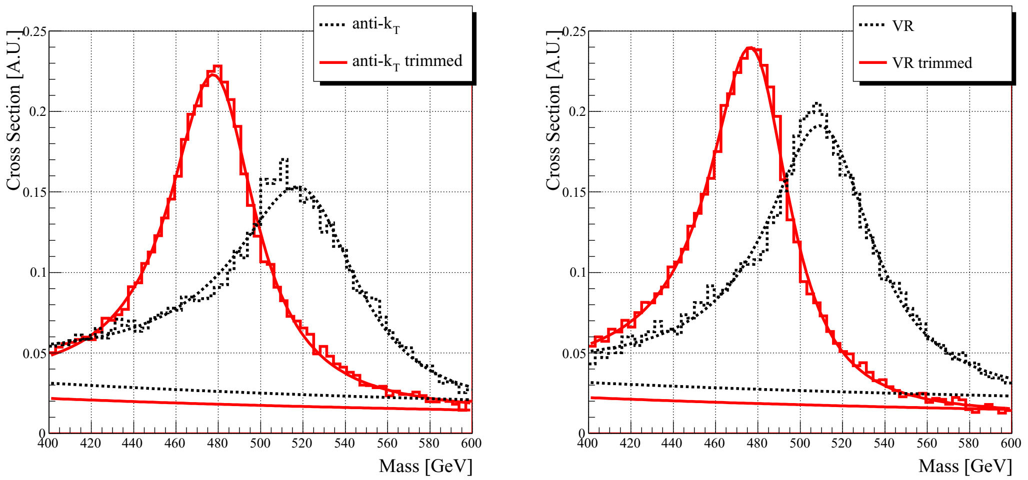

Figure 6.7: Dijet resonance reconstruction with and without trimming using the anti-k_T/VR and anti-k_T/VR (f, H) algorithms. The algorithm parameters are those that optimize the Δ measure of Eq. (6.8), as listed in Table 6.2. The upper curves are fitted to the sum of $S(m)$ and $B(m)$ from Eqs. (6.6) and (6.7), while the lower curves display the contribution of $B(m)$.

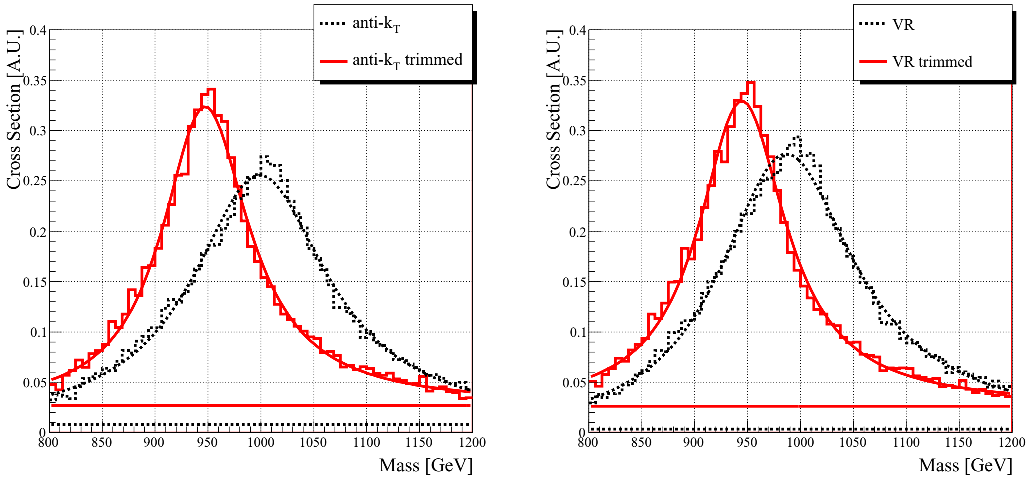

Figure 6.8: Reconstruction of the resonance $m_X = 1$ TeV in $gg \to X \to YY \to gggg$ with and without trimming using the anti-k_T/VR and anti-k_T/VR (f, H) algorithms. The algorithm parameters are those optimized to those that optimize the Δ measure of Eq. (6.8), as listed in Table 6.3. The upper curves are fitted to the sum of $S(m)$ and $B(m)$ from Eqns. (6.6) and (6.7), while the lower curves represent the contribution of $B(m)$.

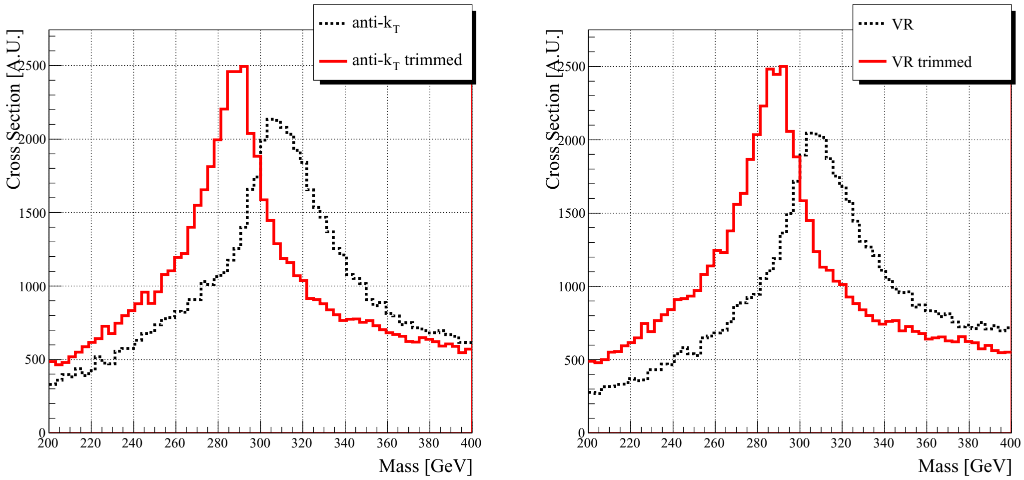

Figure 6.9: Reconstruction of the intermediate resonance mass $m_Y = 300$ GeV in the process $gg \to X \to YY \to gggg$ using the anti-k_T/VR and anti-k_T/VR (f,H) parameters of Table 6.3. These distributions are formed by taking the four hardest jets in each event, considering the two masses from every possible 2×2 partition of these jets, and plotting the masses from the most equitable partition (defined as the one for which $m_{\rm min}/m_{\rm max}$ is closest to one).

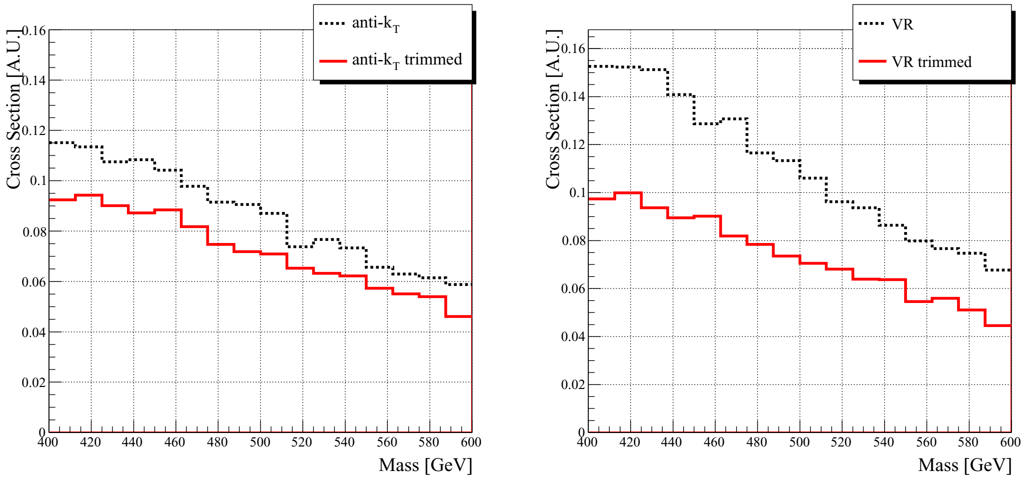

Figure 6.10: Standard model QCD dijet background reconstruction with and without trimming using the anti-k_T/VR and anti-k_T/VR (f, H) algorithms and the optimized signal parameters from Table 6.2.

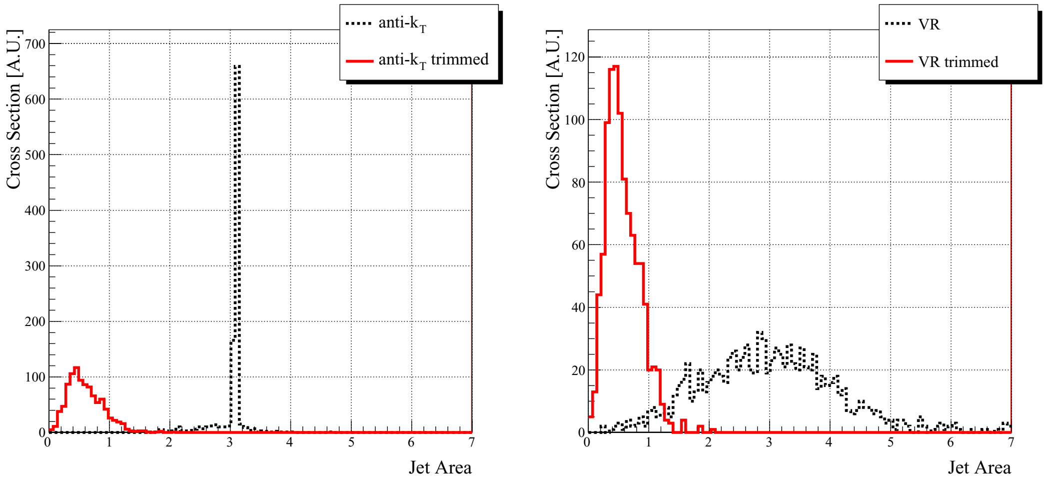

Figure 6.11: Jet area, defined as the area of calorimeter cells clustered into a jet if each cell contains at least an infinitesimal about of radiation, for anti-k_T vs. anti-$k_T(f, H)$ (left panel) and VR vs. VR(f, H) (right panel), using the optimized parameters from Table 6.2. The area of the untrimmed algorithm is roughly πR_0^2, as expected, while the trimmed jet's area is much smaller.

Chapter 7

Jets with Variable R

We introduce a new class of jet algorithms designed to return conical jets with a variable radius R. A specific example, in which R scales as $1/p_T$, proves particularly useful in capturing the kinematic features of a wide variety of hard scattering processes. We implement this scaling of R in a sequential recombination algorithm and test it by reconstructing resonance masses and kinematic endpoints. These test cases show 10 – 20% improvements in signal efficiency compared to fixed R algorithms. We also comment on cuts useful in reducing continuum jet backgrounds.[1]

7.1 Introduction

The high energy frontier of particle physics is probed by hadronic collisions where hard scattering events often result in colored partons. Because these partons undergo showering and hadronization, one cannot go directly from detector measurements to the four-momenta of the scattering. Instead, one must cluster hadrons into jets as an approximation to the short-distance kinematics.

As jets provide an essential window onto hard scattering processes, much recent

---

[1] The jet algorithms we describe have been implemented as plugins to the `FastJet` package [135, 119]. These plugins are available from the authors upon request.

work has focused on the procedures used to construct them: jet algorithms. Many fast, infrared/collinear safe jet algorithms have been developed [139, 91, 92, 93, 94, 140, 123]. These algorithms cluster hadrons through different mechanisms (via cones or sequential recombination) and in different orders (hard to soft, soft to hard, or by angle). To date, however, all jet algorithms used for hadronic collisions return jets of *constant* characteristic size R on the (y, ϕ) plane.[2]

In this paper, we modify existing jet algorithms to cluster with a *variable* effective cone size R. To see how this could be useful, consider a resonance at rest in the lab frame decaying into two partons. To first approximation, the shower of hadrons resulting from each parton will fall in a circular cone of fixed *angular* size regardless of the orientation of the decay with respect to the beam axis. However, a jet algorithm which uses a fixed cone size in (y, ϕ) will not reflect this behavior, as fixed R corresponds to variable angular size. As we will see, this can be remedied by letting the cone size of a jet vary as

$$R \propto \frac{1}{p_T}, \tag{7.1}$$

where p_T is the transverse momentum of the jet with respect to the beam axis.

Remarkably, this simple modification to the jet cone size finds applications beyond simple resonance decays, and can be useful in studying more complicated kinematic structures. The algorithms we present are trivially infrared/collinear safe and are appropriate for use at hadron colliders since Eq. (7.1) is invariant under boosts along the beam axis. Moreover, as we will discuss in Appendix C, the fact that jet radii become larger at lower p_T makes these algorithms especially robust against splittings from detector effects and different showering approximations.

This paper is organized as follows. In Section 7.2, we discuss sequential recombination jet algorithms, extensions to variable R, and the particularly useful case specified

---

[2] Here y and ϕ denote rapidity and azimuth, respectively, while the (y, ϕ)-distance between two particles is $(\Delta R)^2 = (\Delta y)^2 + (\Delta \phi)^2$. We will use R_{ij} to refer to the ΔR distance between objects i and j.

in Eq. (7.1) which we call "VR". In Section 7.3, we quantify the improvement in signal efficiency by using VR algorithms in three different event topologies: single resonance decay, multiple resonance decay, and three-body gluino decay. Section 7.4 contains a discussion of background shaping and jet quality cuts. Section 7.5 contains our conclusions. Discussions of effective jet radii and VR algorithm parameters can be found in the appendices.

7.2 New Recursive Jet Algorithms

7.2.1 Brief Review

Modern jet algorithms fall into two general categories: cone-based and sequential recombination. We focus on the latter recursive algorithms because their infrared/collinear safety is easier to prove, although much of the following discussion could be adapted to cone-based algorithms.

Sequential recombination algorithms begin with a set of four-momenta derived from detector calorimeter cells and then recursively combine pairs of momenta into jets. To do this, they take a list of initial four-momenta and assign each pair (i, j) a "jet-jet distance measure" d_{ij}, while each individual four-momenta is assigned a "jet-beam distance measure" d_{iB}. At each step, the smallest entry in the set of d_{ij} and d_{iB} is identified. If the smallest entry is a jet-jet measure, the two four-momenta are combined into one, their prior distance measures removed from the list, and a new entry with the sum four-vector is computed. If the smallest entry is a jet-beam measure, then the corresponding four-momenta is "merged with the beam" and set aside. The algorithm proceeds in this manner until either all four-momenta are merged with the beam (an inclusive algorithm) or a predetermined distance measure d_{cut} is reached (an exclusive algorithm). After clustering, an inclusive algorithm returns the four-momenta merged with the beam whose p_T is greater than some minimum value, while an exclusive algorithm returns the unmerged four-momenta (that is, those whose $d_{iB} > d_{\rm cut}$). Here we will focus on inclusive algorithms because they are in more widespread use and because not all algorithms have well-defined exclusive modes.[3]

It is possible to parameterize the most popular sequential recombination algorithms for use at hadron colliders via [123]

$$d_{ij} = \min\left[p_{Ti}^{2n}, p_{Tj}^{2n}\right] R_{ij}^2, \qquad d_{iB} = p_{Ti}^{2n}\, R_0^2, \tag{7.2}$$

where the values of n for particular algorithms are listed in Table 7.1, R_{ij} is the (y, ϕ) separation between the two four-momenta, and R_0 is a constant parameter that determines the characteristic jet size. Roughly, $n > 0$ clusters soft items first, $n = 0$ clusters by angle, and $n < 0$ clusters from hard particles outward. We will be particularly interested in algorithms with $n \leq 0$, because as emphasized in Ref. [123], such recursive jet algorithms act much like an idealized cone-based algorithm for sufficiently negative values of n.

Algorithm	n
k_T [91, 92]	1
Cambridge-Aachen [93, 94]	0
Anti-k_T [123]	-1

Table 7.1: Parameterization of popular sequential recombination algorithms according to Eq. (7.2).

At lepton colliders, Eq. (7.2) is usually modified by replacing p_{Ti} with the energy E_i, and R_{ij} with the arc length S_{ij} on the (θ, ϕ) sphere defined by $(\Delta S)^2 = (\Delta\theta)^2 + (\sin\theta\, \Delta\phi)^2$. This ΔS measure will be part of the inspiration for the jet algorithms presented in Section 7.2.3.

---

[3] For instance, the anti-k_T algorithm [123] assigns smaller d_{iB} to harder jets, so these would be merged with the beam and *not* identified as jets if the algorithm were run with a $d_{\rm cut}$.

7.2.2 Variable R Algorithms

We now generalize Eq. (7.2) so that

$$d_{ij} = \min\left[p_{Ti}^{2n}, p_{Tj}^{2n}\right] R_{ij}^2, \qquad d_{iB} = p_{Ti}^{2n} R_{\text{eff}}(p_{Ti})^2, \tag{7.3}$$

where $R_{\text{eff}}(p_{Ti})$ is a dimensionless number interpreted as an effective jet radius for $n \leq 0$. Since Eq. (7.3) is invariant to boosts along the beam axis, it is appropriate for use at hadron colliders. See Appendix C for more detail on the possible choices for R_{eff} and the restriction to $n \leq 0$.

To see why R_{eff} is an effective radius for $n \leq 0$, consider the clustering of two four-momenta i and j. These will only be clustered together if

$$d_{ij} < d_{iB}, d_{jB}. \tag{7.4}$$

Let $p_{Ti} > p_{Tj}$. As discussed in Appendix C, in order for R_{eff} to robustly define an effective radius, we must take $d_{iB} < d_{jB}$. Therefore, the four-momenta are clustered if

$$\frac{d_{ij}}{d_{iB}} = \frac{R_{ij}^2}{R_{\text{eff}}(p_{Ti})^2} < 1, \tag{7.5}$$

which requires the (y, ϕ) separation between i and j to be within an effective radius R_{eff}.

To our knowledge, all current algorithms at hadron colliders use a constant R_{eff}. Although we will only explore one new algorithm here, in which $R_{\text{eff}} \propto 1/p_T$, it is possible to invent new algorithms tailor-made to distinct processes. We leave such extensions to future work, though some guidelines for choosing R_{eff} appear in Appendix C. In principle, a momentum-dependent effective jet size could be implemented in a cone-based algorithm, though we expect that the process of finding stable cones (as is required in SIS-Cone [140]) would be much more complicated.

7.2.3 Introducing VR Algorithms

We now introduce a particular example of the variable R algorithms described above which we will denote as "VR". To motivate this setup, consider a resonance decaying in its center-of-mass frame. If the resonance decays to two jets, these jets will be naturally described by circles on the (θ, ϕ) sphere. This is the setup used to describe jets at e^+/e^- colliders where the center-of-mass frame *is* the lab frame. Unfortunately, the partonic center-of-mass frame at a hadron collider is not fixed, and to maintain boost invariance one must work with circles in (y, ϕ). This setup can present a "Goldilocks" problem in choosing jet radii. If one is forced to use a fixed (y, ϕ) radius, then the cones in the central region will be large in ΔS, while those in the forward region will be small. Getting the radius just right will necessarily involve a tradeoff.

Remarkably, the simplest application of the general jet algorithms described above can remedy this situation, allowing one to use boost invariant jets with a cone size reflecting their true size as measured in the resonance rest frame. This new VR algorithm works by letting the effective radius of a jet go as

$$\text{``VR''}: \quad R_{\text{eff}}(p_T) = \frac{\rho}{p_T}, \tag{7.6}$$

where ρ is a dimensionful constant.

To see why this captures the desired behavior, again consider the decay of a resonance into two partons which shower into jets. In the rest frame of the mother particle, the energy E of each jet is fixed by the mass of the resonance with $E = m_{\text{res.}}/2$. The resulting jets should have roughly the same characteristic angular size ΔS, therefore, the quantity $E\Delta S$ is approximately the same for both jets. As we will now show, fixed $E\Delta S$ is equivalent to Eq. (7.6) to first approximation.

First note that $E\Delta S$ is a quantity that is approximately invariant under both transverse and longitudinal boosts. Intuitively, for small angles and in a massless approximation, the invariant mass of four-momenta is equal to the geometric mean of their energies multiplied by their angular separation. Since invariant mass is a boost invariant quantity, so is $E\Delta S$. More formally, for small angles and in the limit where rapidity y and pseudorapidity η agree,

$$E\Delta S \approx p_T \Delta R, \tag{7.7}$$

where we have used the fact that $E \approx p_T \cosh \eta$ (true for small jet mass) and $\Delta S \approx \Delta R / \cosh \eta$ (see Appendix D). Since p_T and ΔR are invariant under boosts along the beam axis, so is $E\Delta S$ to first approximation. We emphasize that this is true even for boosts transverse to the beam axis; just define a new (y, ϕ) coordinate system along the boost axis and go through the same procedure to show that $E\Delta S$ is invariant. The correction to this argument from finite cluster masses is on the order of $m_{\text{cluster}}/E_{\text{cluster}}$.

Putting this all together, we want build a jet algorithm that captures the fact that the two jets have constant opening angle in their mother's rest frame. Since $E\Delta S$ is approximately boost invariant, this is equivalent to forming jets of constant $E\Delta S$ in any convenient frame. In particular, in the lab frame we can use Eq. (7.7) to swap $E\Delta S$ for $p_T\Delta R$. Therefore, to get jets of constant $E\Delta S$, we should choose R_{eff} to scale like $1/p_T$ as in Eq. (7.6). This defines the VR jet algorithms.

From this logic, we expect the parameter ρ to be proportional to the typical jet size measure $E\Delta S$, and thus proportional to the resonance mass $m_{\text{res.}}$. For a more detailed discussion of the valid parameter range for ρ, see Appendix D.

7.2.4 Event Topologies with VR-symmetry

The VR scaling of Eq. (7.6) is applicable whenever there is reason to expect all jets in an event to have the same $E\Delta S$ in some frame, and we call these events "VR-symmetric". This is certainly the case for a single resonance decay. Less obvious is that this is true for longer cascade decays; even if a cascade involves many intermediate states, it will still be VR-symmetric as long as all jets come from the decay of resonances with a common mass. VR-symmetry can even be satisfied when there is no actual reconstructable resonance. For example, the three-body gluino decay $\tilde{g} \to 2j + \tilde{\chi}_1^0$ would satisfy the requirement toward the kinematic endpoint. We will discuss these scenarios in more detail in the next section.

An important example without VR-symmetry is initial state radiation (ISR). Jets from ISR do not have a preferred mother rest frame and so the VR jet cone scaling is not appropriate. In the case of resonance production plus ISR, the hardest two jets will have the VR scaling, but the ISR will not, so in principle, a hybrid VR/fixed-cone algorithm could have better jet reconstruction performance.[4] While we will include ISR in our Monte Carlo simulations, we will only study the hardest jets in an event for which VR-symmetry is expected to apply.

Now we would like to address a few caveats to the VR derivation in Section 7.2.3. We derived our expression for R_{eff} in the small cone limit. In practice, one must account for corrections in going to finite-sized jets when choosing reasonable jet parameters (see Appendix D). Similarly, for low p_T the algorithm would return pathologically large jets, so one is forced to cut off the jet radius at some R_{max}, so that

$$R_{\text{eff}}(p_T) = \min\left[\frac{\rho}{p_T}, R_{\text{max}}\right]. \tag{7.8}$$

For small enough R_{max}, Eq. (7.8) effectively defines a kind of hybrid VR/fixed-cone algorithm as needed for events involving ISR, though in this paper we will not try to optimize the value of R_{max}.

---

[4] Strictly speaking, there is no invariant distinction between jets from a hard collision and jets from ISR. However, since ISR jets are generally softer than jets from the hard scattering, one implementation of a hybrid algorithm might involve an explicit p_T cutoff below which jets are clustered with a fixed cone, and above which VR is used.

As a secondary issue in the VR derivation, we implicitly assumed that jets will remain circular in R as we boost from the mother rest frame to the lab frame. While this is true if the boost is only along the beam axis (as is the case for single resonance production), for more complicated event topologies, the particular shape of a jet will depend on the orientation of the hard process, and will in general be non-circular. Our algorithm forms circular jets in (y, ϕ) so it will not capture the true jet shape in more complicated decays. However, unlike a fixed R algorithm, the VR algorithms do scale the overall jet size appropriately under boosts. Since jets are only conical in a statistical sense anyway, we do not expect shape distortions to reduce the efficacy of the VR algorithms.

We can implement Eq. (7.8) in any existing jet algorithm parameterized by Eq. (7.3). However, as discussed in Appendix C, it is only meaningful to define R_{eff} when $n \leq 0$. Therefore, it does not make sense to apply it to the k_T algorithm where $n = 1$. We will therefore combine it with anti-k_T [123] (denoted AKT) and Cambridge-Aachen [93, 94] (denoted CA), and compare the resulting algorithms, AKT-VR and CA-VR, with the original AKT and CA algorithms. A summary of the jet definitions used in our study appear in Table 7.2, and a sample lego plot showing the effects of the VR algorithm in reconstructing an event can be seen in Figure 7.1.

Shorthand	n	R_{eff}
AKT	-1	R_0
AKT-VR	-1	ρ/p_T
CA	0	R_0
CA-VR	0	ρ/p_T

Table 7.2: The four jet algorithms used in this study, as parameterized by Eq. (7.3). For the VR algorithms, we also impose a maximum jet radius as in Eq. (7.8).

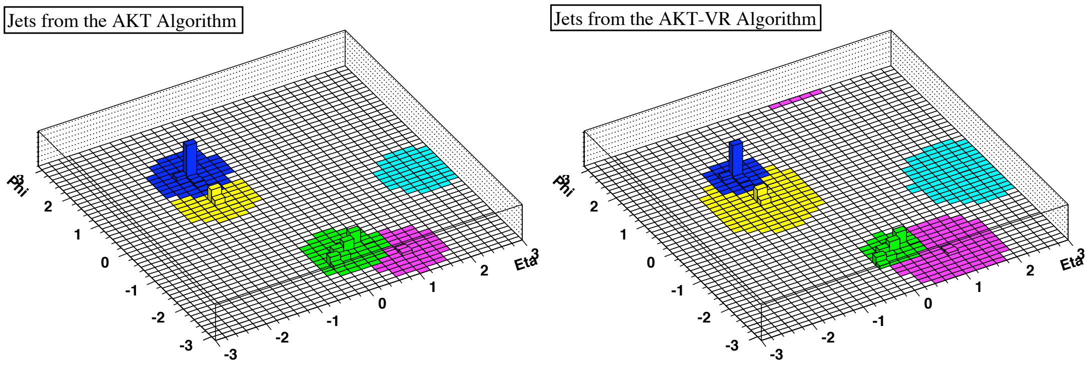

Figure 7.1: The same event reconstructed by anti-k_T (left) and its VR modification (right). Note that in going to the VR algorithm, the high-p_T jets (dark blue, green) have been reduced in size while softer jets (yellow, purple, light blue) have grown. In this example, only the two harder jets are expected to exhibit VR-symmetry, and the softer jets are saturating the $R_{\max} = 1.0$ constraint.

7.3 Jet Reconstruction Performance

Here we use Monte Carlo simulations to compare the AKT and CA algorithms with their VR cousins. We investigate three different kinematic scenarios to see how the algorithms perform with both large and small jets. We focus only on signal efficiency in this section, and turn to background rejection issues in Section 7.4.

Our signal and background samples have both been generated in `Pythia 6.4.14` [121], with parton-level signal events generated in `MadGraph 4.4.5` [120]. We use nominal LHC beam parameters (14 TeV proton-proton collisions). Final state hadrons are grouped into $\delta\eta \times \delta\phi = 0.1 \times 0.1$ calorimeter cells between $-3 < \eta < 3$ and assigned massless four-momenta based on the calorimeter energy. These calorimeter cells are the starting point for the recursive jet clustering.

We use the `FastJet 2.3.4` [135, 119] package for the AKT and CA algorithms, and we wrote new `FastJet` plugins for the AKT-VR and CA-VR algorithms. For each kinematic scenario, we scan over a range of jet parameters to optimize the jet algorithm performance. To keep the comparison fair, we limit the maximum effective R of the VR jet cones using $R_{\max}$ as in Eq. (7.8), and scan the R_0 parameter of the fixed cone algorithms from 0 to R_{max}. In the three cases below, we find a universal improvement in using the VR algorithms over their fixed R cousins.

7.3.1 Resonance Decays Without Background

The simplest test of a jet algorithm is resonance reconstruction without standard model background. We consider resonances with backgrounds in Section 7.4. Here we consider the scenario of a color-octet scalar X, of negligible width, in the process $gg \to X \to gg$.[5] We scan the jet parameters up to a maximum radius $R_{\text{max}} = 1.5$, and optimize the parameters to maximize the percentage of events reconstructed in a narrow mass window ($m_X \pm 25$ GeV) around the true resonance mass.[6] The results of this optimization are shown in Table 7.3 for four different values of m_X.

Algorithm	500 GeV	1 TeV	2 TeV	3 TeV
AKT → AKT-VR	18% $(0.9, 200)$	14% $(1.0, 450)$	10% $(1.2, 1000)$	8% $(1.3, 1500)$
CA → CA-VR	17% $(0.9, 175)$	14% $(1.0, 400)$	7% $(1.2, 1000)$	9% $(1.2, 1500)$

Table 7.3: Percentage increase in the number of events reconstructed in the mass window $m_X \pm 25$ GeV for the VR variant over the original algorithm. The numbers in parenthesis are the optimized parameters for the original and VR variant (R_0 and ρ, with ρ in GeV) respectively. We see that the effective $\Delta R \simeq \rho/m_X$ of the VR algorithms is comparable to the fixed ΔR.

The resonance invariant mass plots from this analysis can be seen in Figures 7.2 and 7.3. The results indicate a uniform improvement in going from the original algorithms to their VR variants: the reconstructed resonances are narrower and taller. The relatively large cone sizes found in the optimization should not be troubling as similar results were found in Ref. [132]. The optimized choices of ρ displayed in Table 7.3 also make intuitive sense. We expect most of these jets to have a p_T slightly below half the resonance mass, so for $\rho \approx m_X/2$, R_{eff} will be $\mathcal{O}(1)$, close to the

---

[5] The X couples to gluons via the operator $\text{Tr}(XG_{\mu\nu}G^{\mu\nu})$.

[6] The ±25 GeV mass window was chosen by hand to approximate the width of the reconstructed peaks after showering and hadronization. It is not related to the perturbative resonance width, which is zero, or calorimeter smearing, whose effects we have not included.

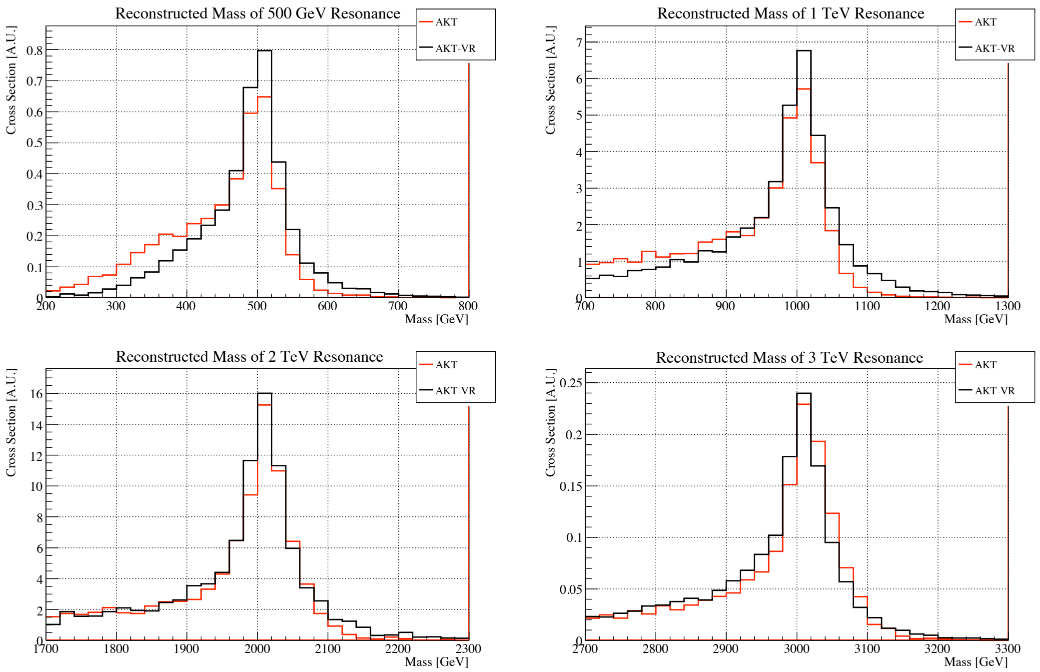

Figure 7.2: Invariant mass distributions for the $X \to gg$ resonance decay using the optimized AKT and AKT-VR parameters in Table 7.3. The distributions have the same normalization, and the y-axis is in arbitrary units (A.U.). The VR algorithms yield a better reconstruction, both in the height and width of the resonance.

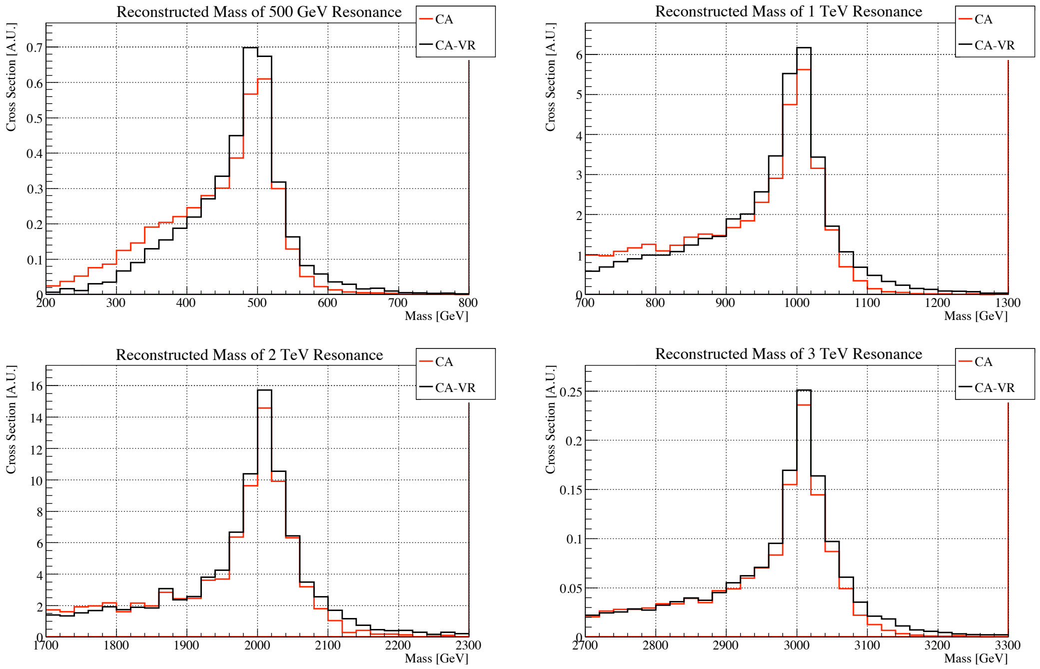

Figure 7.3: Same as Figure 7.2 but comparing the CA and CA-VR algorithms.

optimized value found for the fixed R algorithms. Note that the values of ρ are consistent with the discussion in Appendix D.

It is interesting that the improvements offered by the VR algorithms are greatest for small resonance masses. The reason is that signal degradation can come from out-of-cone corrections and contamination from the underlying event (including ISR). For larger resonance masses with high p_T jets, underlying event corrections are proportionally smaller, so one need only make the cone size sufficiently large to capture the bulk of the resonance signal. For smaller resonance masses with low p_T jets, the underlying event corrections are more important, and the VR algorithms do a better job balancing the need for large cones to capture the signal against the need for suppressing contamination.

As a side note, the AKT algorithm does perform better than the CA algorithm, but by only 1–5% in the cases considered. Thus, the improvement shown by the VR algorithms is greater than the difference between the two fixed cone algorithms.

7.3.2 Longer Decay Chains

The scenario considered above involved a simple event topology and relatively large jet cones. Moreover, the jets were only boosted along the beam axis, so we expect them to be approximately circular in (y, ϕ). Here we test a more complex scenario where the final state is more crowded (requiring smaller cones), and the final state jets can be boosted along a transverse axis. As discussed before, when jets are produced in a transversely boosted frame we expect the VR algorithms to capture their scaling, but not their exact shape. Here we will see that by accounting only for this scaling we are able to realize significant performance improvements.

We use two color-octet scalars, X and Y, again with negligible width, of mass $m_X = 3$ TeV and $m_Y = 500$ GeV, decaying to jets via $gg \to X \to YY \to gggg$. After clustering the jets, we optimize the algorithm parameters to maximize the number of

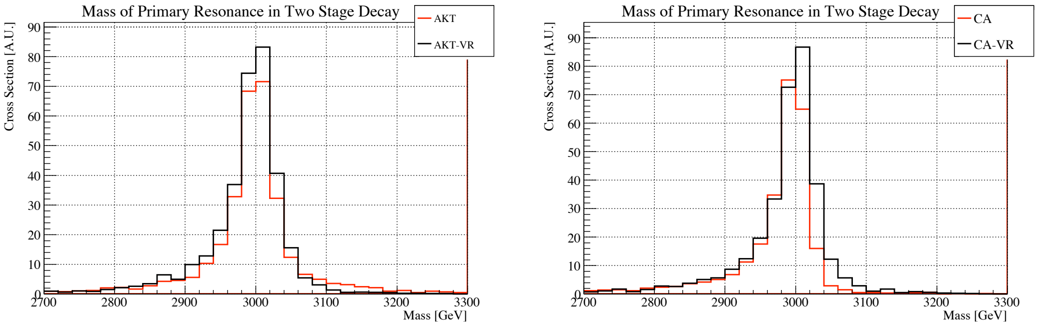

Figure 7.4: Invariant mass distributions of the heavy resonance X for the $X \to YY \to gggg$ cascade decay scenario using the optimized parameters in Table 7.4. The distributions have the same normalization, and the y-axis is in arbitrary units (A.U.). These plots are made after insisting that pairs of jets reconstruct the lighter resonance mass m_Y within 25 GeV.

events where two pairs of jets each reconstruct m_Y within 25 GeV of its true value, and all four jets reconstruct m_X within 50 GeV. Here we limit the maximum cone size to $R_{\max} = 1.0$. The results are shown in Table 7.4. We again see a universal improvement in reconstruction. The reconstructed distributions for m_X and m_Y can be seen in Figures 7.4 and 7.5, respectively.

Algorithm	$X \to YY$
AKT → AKT-VR	15% $(0.7, 450)$
CA → CA-VR	23% $(0.6, 450)$

Table 7.4: Percentage increase in the number of reconstructed events for the process $gg \to X \to YY \to gggg$. We insist that pairs of jets reconstruct $m_Y \pm 25$ GeV, and that four jets reconstruct $m_X \pm 50$ GeV. The numbers in parenthesis are the optimized parameters for the original and VR variant (R_0 and ρ, with ρ in GeV) respectively.

7.3.3 Three-Body Gluino Decay

As we remarked in Section 7.2.3, we expect the VR algorithms to improve jet reconstruction as long as there is some reference frame in which the jets have the

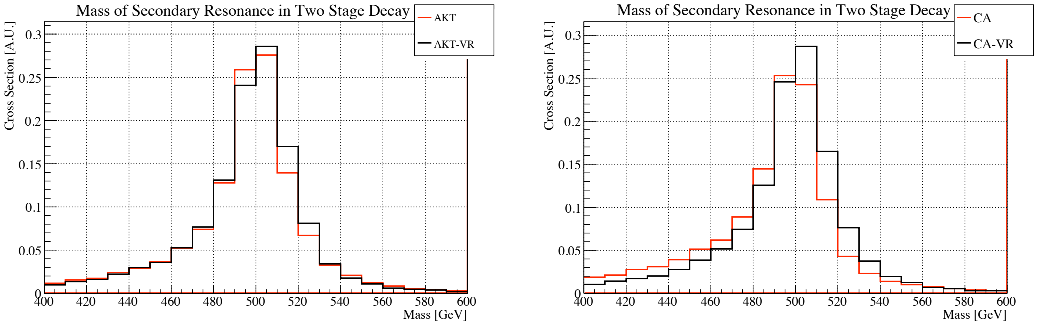

Figure 7.5: Same as Figure 7.4 but for the lighter resonance Y.

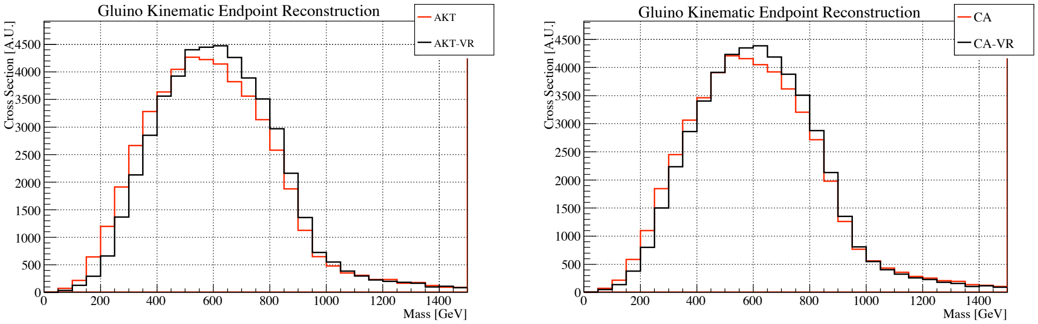

Figure 7.6: Invariant mass distributions of dijets in three-body gluino decay for the optimized parameters in Table 7.5. The distributions have the same normalization, and the y-axis is in arbitrary units (A.U.). For the chosen spectrum we expect to see an endpoint at 900 GeV. It can be seen that the VR algorithms fall more sharply near this endpoint than the fixed cone algorithms.

same energy and opening angle. Here, we demonstrate a useful application of this effect with a gluino decaying to a neutralino lightest supersymmetric particle (LSP), $\tilde{g} \to q+\bar{q}+\tilde{\chi}_1^0$. If the intermediate squark is on-shell, then we expect no such reference frame, as the "upper" and "lower" jets have different preferred mother frames. However, if the squark is off-shell, then the process is a three-body decay, and the gluino rest frame is a preferred frame for both jets. Moreover, we expect VR-symmetry to be enhanced near the kinematic endpoint where in the gluino rest frame, the two jets are back-to-back while the LSP is at rest. Since gluinos are typically produced with small transverse boosts in the lab frame, we do not expect large distortions of the jet shape.

To test our algorithm, we consider the associated production of gluinos with a neutralino LSP via $f\bar{f} \to \tilde{g} + \tilde{\chi}_1^0$ and use a spectrum where $m_{\tilde{g}} = 1$ TeV and $m_{\tilde{\chi}_1^0} =$ 100 GeV. We choose the associated production channel for demonstration purposes to eliminate the combinatorial confusion present in gluino pair production. To ensure a three-body decay, we have lifted the squarks out of the spectrum by placing them at 5 TeV. With this spectrum, we expect to see an endpoint in the dijet invariant mass distribution at 900 GeV. The more accurate a jet algorithm, the better it can reconstruct this endpoint. Therefore, we define the measure of reconstruction performance to be the *difference* in the number of events reconstructed in 100 GeV windows above and below 900 GeV. We have optimized this measure with $R_{\max} = 1.5$. The improvement of the VR variants is shown in Table 7.5 and Figure 7.6.

Algorithm	$\tilde{g} \to q + \bar{q} + \tilde{\chi}_1^0$
AKT → AKT-VR	14% $(1.2, 600)$
CA → CA-VR	7% $(1.3, 650)$

Table 7.5: Improvement, measured as the difference in the number of events reconstructed in 100 GeV bins on either side of the endpoint, in using VR algorithms to reconstruct three-body gluino decays. The numbers in parenthesis are the optimized parameters for the original and VR variant (R_0 and ρ, with ρ in GeV) respectively.

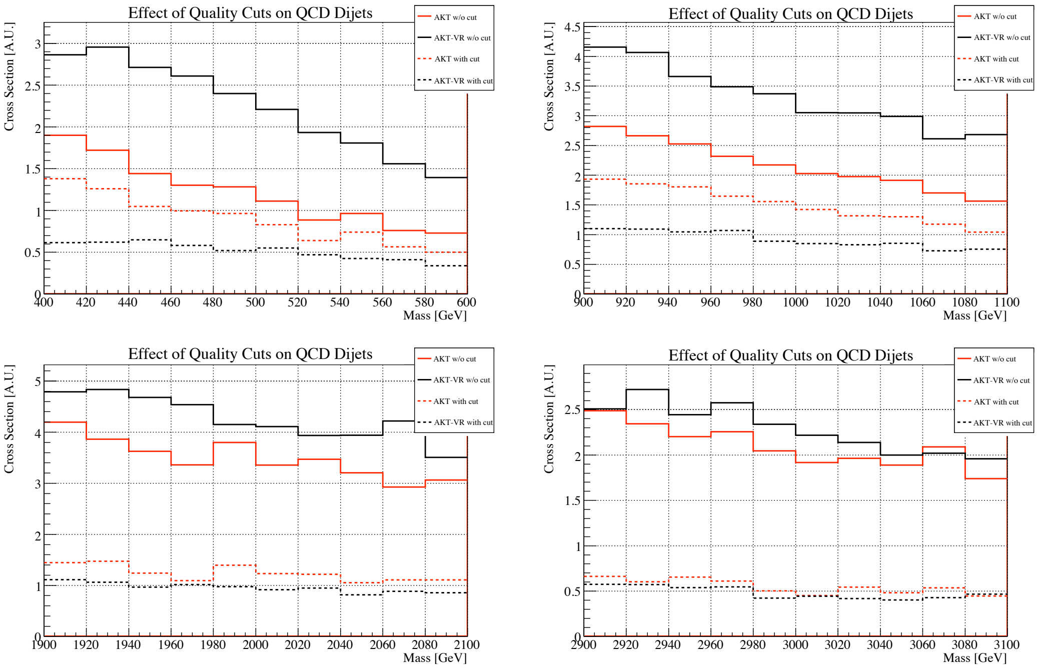

Figure 7.7: Invariant mass distributions of the QCD dijet background for the AKT and AKT-VR algorithms, plotted in windows corresponding to the four fiducial resonances. The distributions have the same normalization, and the y-axis is in arbitrary units (A.U.). The solid (dotted) lines show the background without (with) quality cuts. The red lines show the original algorithm, and the black lines show the VR modification. The results are qualitatively similar for CA and CA-VR.

7.4 Resonance Decays With Background

In the previous section, we showed that VR algorithms generically lead to improvements in signal reconstruction for events meeting our VR-symmetric criteria. It is natural to wonder how the VR algorithms will handle background events. The VR algorithms have a dimensionful parameter ρ, unlike their fixed cone counterparts, so some shaping of the background might take place. However, we will see that this is not the case when one imposes reasonable jet quality cuts.[7]

To understand the effect of the VR algorithms on background, we consider the color-octet resonances previously described in Section 7.3.1 on top of a background of QCD dijets. We optimize our algorithm parameters to maximize signal significance,

---

[7] These quality cuts were not used in our signal-only analysis.

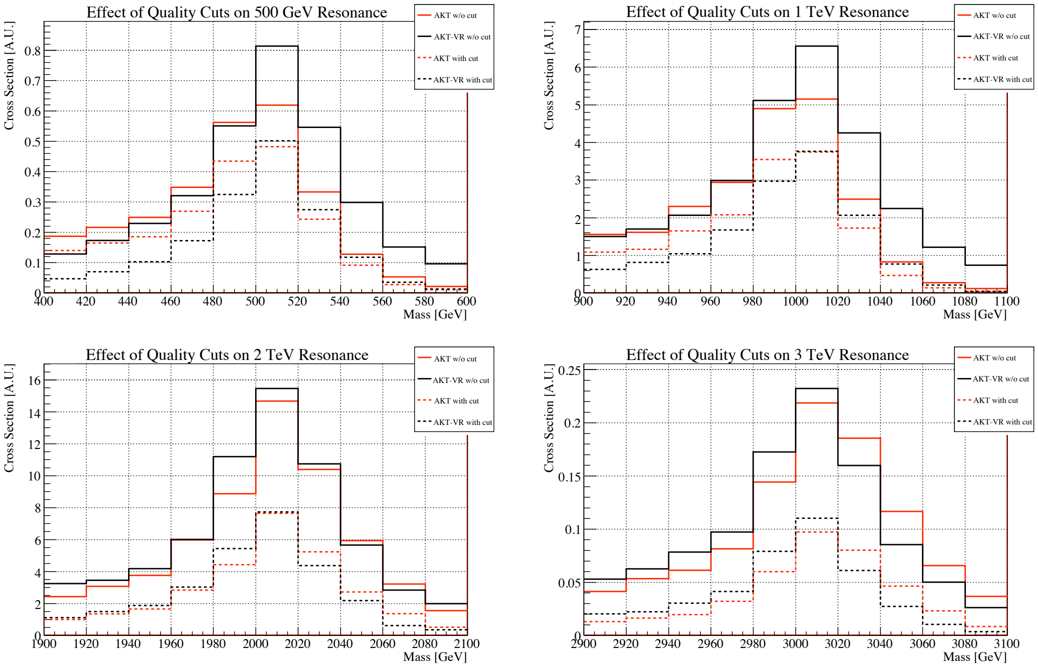

Figure 7.8: Same as Figure 7.7 but for the resonance signals.

defined as $S/\sqrt{B}$, where S and B are the signal and background cross sections, respectively, in a given mass window. In addition, we remove the enormous low-p_T QCD background by requiring the two hardest jets each satisfy $p_T > m_{\text{res.}}/4$.

Let us first consider the dijet background without any kind of quality cut, as shown by the solid-lined histograms in Figure 7.7. Here we see significant background shaping by the VR algorithms: they are taking low p_T jets from events with small dijet invariant mass, assigning the jets large cones, and thus pushing the events to a higher dijet invariant mass compared to the fixed cone algorithms. Because the QCD background exhibits a steeply falling distribution in invariant mass, this increases the normalization of the background in the mass windows shown in Figure 7.7. However, this problem is not particular to the VR algorithms, and fixed cone algorithms with large R_0 will inevitably increase the background to an analysis by having cones that swallow soft particles toward their edges.

Such contamination can be effectively controlled by jet quality cuts, which can take many different forms. For example, we could place cuts limiting jets to the central region of the detector. Another possibility would involve systematically subtracting a four-momentum related to the "catchment area" of a jet [126]. Here, we explore another approach by requiring the energy- and p_T-weighted jet centers approximately coincide. In practice, this means imposing

$$\Delta R(\vec{P}_E, \vec{P}_{p_T}) < \delta, \tag{7.9}$$

where $\vec{P}_E$ and $\vec{P}_{p_T}$ are the energy- and p_T-weighted jet centers defined by

$$\vec{P}_E = \sum_i E_i \, \hat{p}_i, \qquad \vec{P}_{p_T} = \sum_i p_{Ti} \, \hat{p}_i, \tag{7.10}$$

and $\hat{p}_i$ is the massless four-vector of unit length corresponding to the ith calorimeter cell.

It is reasonable to impose the jet quality standard of Eq. (7.9) because, as discussed in Ref. [141], we expect jets from a massless parton to have a small, hard central core. For our analysis we choose $\delta = (0.04, 0.025, 0.015, 0.01)$ for $m_X = (500 \text{ GeV}, 1 \text{ TeV}, 2 \text{ TeV}, 3 \text{ TeV})$. The result of imposing such a cut on the background is shown in Figure 7.7. These δ values were chosen by estimating the characteristic size of $\Delta R(\vec{P}_E, \vec{P}_{p_T})$ for each mass window. We see that this helps significantly in reducing background. If such a quality cut reduced the signal as much as the background it would be of no use, but as can be seen in Figure 7.8, these cuts have a milder effect on the signal than on background, since the signal jets do have hard central cores. One expects that the δ parameter could be optimized to increase the signal yield, but we will not pursue this possibility here.

Now we employ the quality cuts and present the improvement in $S/\sqrt{B}$ significance by using the VR algorithms. We consider a narrow mass window ($m_X \pm 25$ GeV) around the resonance as in the signal-only study from Section 7.3.1. The results are shown in Table 7.6, and we again see a universal improvement in going to VR. The jet parameters are comparable to the ones seen in the signal-only study of Table 7.3.

Algorithm	500 GeV	1 TeV	2 TeV	3 TeV
AKT → AKT-VR	19% $(0.9, 225)$	23% $(0.9, 450)$	18% $(1.2, 1000)$	21% $(1.3, 1500)$
CA → CA-VR	10% $(0.8, 200)$	18% $(0.9, 450)$	15% $(1.2, 1000)$	18% $(1.3, 1500)$

Table 7.6: Percentage increase in $S/\sqrt{B}$ significance for resonance reconstruction over background within a *fixed* mass window $m_X \pm 25$ GeV. The numbers in parenthesis are the optimized parameters for the original and VR variant (R_0 and ρ, with ρ in GeV) respectively.

While accurate mass reconstruction is important for measuring the properties of a hadronic resonance, for discovery of a resonance one simply wants to increase $S/\sqrt{B}$. Thus, we also consider a floating mass window, of variable size around m_X, chosen to maximize $S/\sqrt{B}$ for each jet parameter. That is, we define a mass window from $m_X - \delta m_-$ to $m_X + \delta m_+$, and optimize $S/\sqrt{B}$ by simultaneously varying the jet algorithm parameters and $\delta m_\pm$. Results for this study are shown in Table 7.7, with the optimized mass windows in Table 7.8. The improvement in going from non-VR to VR algorithms is similar to before, with small discrepancies in the results for $m_X = 500$ GeV and $m_X = 3$ TeV clustered with AKT. However, the discrepancies are due primarily to shortcomings in the optimization procedure rather than physical effects. For $m_X = 500$ GeV, the window that optimizes $S/\sqrt{B}$ for the non-VR algorithms is quite large and skewed to lower masses ($400 \leftrightarrow 515$ GeV for AKT, compared to $470 \leftrightarrow 540$ GeV for AKT-VR). Similarly, the optimized window for $m_X = 3$ TeV with AKT is skewed toward higher masses. A more thorough treatment of background and collider effects would likely prevent optimization with such skewed windows and restore some of the gains seen in Table 7.6.

Algorithm	500 GeV	1 TeV	2 TeV	3 TeV
AKT → AKT-VR	10% $(0.6, 225)$	21% $(0.9, 500)$	14% $(1.2, 1000)$	8% $(1.4, 1600)$
CA → CA-VR	3% $(0.6, 200)$	16% $(0.8, 450)$	11% $(1.2, 1000)$	13% $(1.4, 1700)$

Table 7.7: Percentage increase in $S/\sqrt{B}$ significance for resonance reconstruction over background in a *variable* mass window. The numbers in parenthesis are the optimized parameters for the original and VR variant (R_0 and ρ, with ρ in GeV) respectively.

Algorithm	500 GeV	1 TeV	2 TeV	3 TeV
AKT	400 ↔ 515	945 ↔ 1035	1975 ↔ 2055	2985 ↔ 3065
AKT-VR	470 ↔ 540	975 ↔ 1045	1965 ↔ 2045	2985 ↔ 3045
CA	400 ↔ 515	945 ↔ 1025	1965 ↔ 2055	2985 ↔ 3055
CA-VR	455 ↔ 530	965 ↔ 1035	1965 ↔ 2045	2985 ↔ 3045

Table 7.8: Optimized mass windows for the results in Table 7.7. All values are in GeV.

7.5 Conclusion

We have constructed a new class of jet algorithms in which jet radii R become functions of jet p_T. Although we have only explored the simplest new algorithm in this class, the rules described in Appendix C should provide a well-defined sandbox in which more complicated variants can be explored. Surely undiscovered algorithms exist within this framework that can further improve jet-based analyses at hadron colliders.

In this paper, we focused on the simplest variable R algorithm, denoted VR, in which R scales as $1/p_T$. Remarkably, this scaling captures the physical size of jets for many diverse processes. To test this algorithm, we developed a sequential-recombination implementation using the `FastJet` [135, 119] package, extending the Cambridge-Aachen [93, 94] and anti-k_T [123] algorithms to VR variants. In the analysis of single/multiple resonance decays we routinely saw 10 – 20% increases in signal efficiency when using the VR algorithms. A similar improvement appears in reconstructing the kinematic endpoint in three-body gluino decay.

In order to use the VR algorithms in the presence of a significant continuum jet background, we needed to impose jet quality cuts. We emphasize that these cuts are useful in and of themselves, and have strong physical motivation, since jets from hard partons have different substructure compared to jets formed from soft radiation. After quality cuts are imposed, the VR algorithms outperform their fixed cone cousins by 10 – 20% in statistical significance.

Given our success in developing a jet algorithm for VR-symmetric event topologies, one could imagine developing more powerful "designer" jet algorithms to improve signal acceptance or background rejection for specific physics scenarios. The original anti-k_T algorithm emphasizes the utility of recursive jet algorithms, since it aims to return effective cone jets in an infrared/collinear safe manner, allowing for simpler theoretical calculations and easier experimental calibration [123]. The AKT-VR variant emphasizes the flexibility of recursive jet algorithms to adapt to different event topologies. One suspects that by including additional global event data (or even jet substructure [90, 95, 96, 107, 108] data) in the definitions of d_{ij} and d_{iB}, one could better extract information about specific hard scattering processes despite the complicated hadronic environment.

Chapter 8

Conclusion

Here we will review the motivations for attempting to understand physics at the TeV scale. We will also summarize the results presented in this thesis, highlighting how they make progress toward this goal.

As we have discussed, the Standard Model of particle physics has proved remarkably robust. Despite a relatively simple field content, it has been able to explain nearly all the data in particle physics for the past 40 years. Yet, what is perhaps the most important element of the model, the Higgs boson, has eluded us. Fortunately, the Tevatron is closing in on the Higgs, and if it fails to find it the LHC almost certainly will (that is, if it exists). Still, the discovery of a Higgs would not answer all of our questions about the TeV scale. We do not know why the Higgs is stable at the electroweak scale when no symmetry of the Standard Model protects its mass. If electroweak symmetry is not broken by a SM Higgs, then it remains to be understood what subtleties allow for new physics states, yet pose no conflicts with electroweak precision data. Furthermore, the identity of dark matter has yet to be uncovered, and its connection, if any, to the physics behind whatever sets the electroweak/TeV-scale remains a mystery.

Phenomenology adopts a bottom-up approach to tackling these mysteries. Through a combination of model building and the development of clever measurement techniques, it is hoped that the field can deduce the answers to the above questions from the results of experiments coming online over the next few years. If all goes as planned, the upcoming decade promises to be a wonderfully exciting time, filled with a rich interplay as TeV-physics begins to manifest itself at different experiments [142]. This thesis, in preparation for the TeV-era, attempts to touch on the main topics of interest at this scale (electroweak symmetry breaking, dark matter) in the various capacities of phenomenological study (model building, new measurement techniques).

The thesis began, in chapter 2, with an exercise in model building. In this chapter we saw that little Higgs models, in which the Higgs particle is the pseudo-Goldstone of a symmetry group with special properties, can be easily endowed with a $\mathbb{Z}_2$ parity, making some particles in the theory classically stable and natural candidates for dark matter. However, just as the axial anomaly in QCD renders the neutral pion unstable, quantum anomalies from UV fermions can destabilize the dark matter candidates of little Higgs models. Fortunately, if the UV fermions of a little Higgs theory are chosen in the correct number and with the correct group structure, then the quantum anomalies can be removed, stabilizing any potential dark matter candidates. Chapter 2 discussed the rules necessary to achieve this stability, and discusses general features of models which incorporate them.

Chapter 3 also discussed dark matter, but with a focus on its signatures at direct detection experiments. Beginning with a model of TeV-scale dark matter coupled inelastically to SM particles via a GeV-scale hidden sector, the scenario discussed in this chapter adds a DM Yukawa coupling to the same gauge singlet used in the NMSSM. This setup has the virtue of naturally explaining why dark matter has the same scale as the electroweak sector of the SM. Remarkably, this scenario gives a very distinct recoil spectrum showing features of both elastic and inelastic scattering. If such a spectrum was eventually measured at a direct detection experiment it would be a smoking gun signature for such a model.

At this point, the thesis shifts gears and presents results with more of an emphasis on collider phenomenology. Chapter 4 introduces a new measurement sensitive to the Higgs/weak gauge-boson coupling. The primary virtue of the proposed measurement is its insensitivity to experimental and theoretical uncertainties. Through such a measurement, one might detect subtle shifts in the Higgs couplings signaling the effects of new physics, and perhaps giving clues to the mechanism behind electroweak symmetry breaking.

Chapter 5 continued to focus on collider measurements relevant to electroweak symmetry breaking. In this chapter a measurement sensitive to the polarization of the top quark was proposed. Because the top quark has a special place in most models of new physics beyond the SM, a measurement of its coupling (in particular, the handedness of its coupling) would provide a clue to the nature of electroweak symmetry breaking.

Finally, chapters 6 and 7 dealt with jet algorithms. Jet algorithms are systematic procedures for taking collider data and grouping all of the measured hadronic radiation into a set of final states one can compare with calculations of feynman amplitudes. While these algorithms certainly aid in the search for new physics at colliders, they serve a more general role, affecting all measurements of hard scattering processes with hadronic final states. The two algorithms proposed here are designed to improve event reconstruction. That is, they seek to more accurately reconstruct the parton momenta giving rise to the measured final states. To accomplish this, they adopt two complimentary approaches. Chapter 6 made use of the natural hierarchy of radiation scales in a collider event to separate out the radiation of a hard scattering that one is interested in from other, softer, sources which can contaminated it. Chapter 7, on the other hand, adjusts the size of jets on a jet-by-jet basis to better account for pathologies in the geometry used to describe events at hadron colliders.

It is demonstrated in the text that each of these techniques is capable of improving event reconstruction on its own, and when combined, the resulting reconstruction is even better.

Appendix A

Distinguishing anomalous vertices through spin measurements

For models without T-parity, the LTP decays quickly to two gauge bosons with a lifetime of order 10^{-15}s [143]. Such a decay would not leave a displaced vertex. A measurement of the life-time is therefore very difficult without a precise determination of the width which may be smaller than the experimental resolution even for the normal vertex. However, it is possible to distinguish this anomalous vertex from a normal three gauge-boson vertex through a spin measurement. If reconstruction of A_A is possible, one can form the distribution of the outgoing gauge-bosons, A_V, about the axis of polarization. Since A_A carries unit spin, we expect either $\cos^2\theta$ or $\sin^2\theta$ distributions, depending on the initial polarization of A_A, where θ is the angle between the outgoing bosons and the axis of polarization. For a normal three gauge-boson vertex we expect a $\sin^2\theta$ ($\cos^2\theta$) distribution if A_A is transversely (longitudinally) polarized. For the anomalous vertex it is precisely the opposite behavior as is easily seen by angular momentum conservation in the rest frame of A_A. This is summarized in Table A.1. The initial polarization of A_A can be established to be longitudinal if it is the product of a heavy fermion decay for example. Such measurements should help unravel the anomalous nature of the vertex.

A_A polarization	$\frac{d\Gamma_{A\to VV}}{d\cos\theta}$	
	Regular	Anomalous
Transverse	$\sin^2\theta$	$\cos^2\theta$
Longitudinal	$\cos^2\theta$	$\sin^2\theta$

Table A.1: The angular distribution of the two outgoing SM gauge-boson about the polarization axis in the rest frame of the heavy vector-boson is a good discriminant between the regular three gauge-boson vertex and the anomalous one.

Appendix B

WZW terms for general G/H chiral Lagrangians

In this section we will review the motivation for the WZW term (following [144]) and give a prescription for computing it in the general G/H case as detailed in [45]. We will make an effort to keep it as explicit as possible by including normalization factors, factors of i, and dispensing with the language of differential forms.

WZW terms can be thought about as coming from the requirement of anomaly matching as given by 't Hooft. Begin by considering a global symmetry G that is linearly realized by colored fermions far in the UV. Here, one could imagine trying to weakly gauge G if there was an additional uncolored spectator sector keeping G anomaly free. As one goes from the UV into the IR and the colored group becomes confining, the condensate breaks G down to H. The theory's degrees of freedom change and G/H is realized non-linearly by Goldstones. Yet, as the fundamental theory preserves gauge symmetry, so should the low energy effective theory. The Goldstones must reproduce the anomaly of the confined quarks to cancel the contribution to the anomaly from the spectator sector. *Therefore, WZW terms are added to a Lagrangian in order to reproduce the quarks' anomalies in the Goldstone sector.*

Before we write down the anomaly terms we should note a distinction that arises when dealing with anomalies. To calculate an anomaly one must make a choice of regularization that determines which currents exhibit the anomaly. Regularizing a theory so that all currents exhibit an anomaly in the same way leads to the so called *symmetric* anomaly. Regularizing so that the unbroken subgroup H is anomaly free leads to the *covariant* anomaly. In this paper we are interested in the case where H is an anomaly-free vector subgroup of G. To keep H anomaly free and unbroken we will be interested in the covariant anomaly. We hope that the following will be useful for anyone attempting to compute the actual anomalous vertices and note that the distinction between the *symmetric* and *covariant* anomalies does lead to a numerical difference in the coefficients of such vertices.

B.1 Computation

Chu, Ho, and Zumino [45] give a prescription for calculating the WZW term in general G/H theories subject to the following conditions: H is anomaly free, reductive, and $\pi_4(G/H) = 0$. Their formalism is more than what is required for the simple case of chiral symmetry breaking models, but it would be useful in studying more general models. They calculate the WZW term to be

$$\mathcal{L}_{\mathrm{WZW}}(\pi) = -i\int_0^1 \pi_a G_a(\pi, A_t)dt \quad + \quad B(0) - B(1) \tag{B-1}$$

where the B terms are outside the integral sign and

$$A_{t\mu} = e^{-it\pi}A_\mu e^{it\pi} - i(\partial_\mu e^{-it\pi})e^{it\pi} \tag{B-2}$$

$$G_a(\pi, A) = \frac{i}{24\pi^2}\epsilon^{\mu\nu\rho\sigma}\,\mathrm{Tr}\left[T_a\Big(\partial_\mu A_\nu \partial_\rho A_\sigma - \frac{i}{2}\partial_\mu A_\nu A_\rho A_\sigma + \frac{i}{2}A_\mu \partial_\nu A_\rho A_\sigma - \frac{i}{2}A_\mu A_\nu \partial_\rho A_\sigma\Big)\right] \tag{B-3}$$

$$B(t) = \frac{1}{48\pi^2}\epsilon^{\mu\nu\rho\sigma}\,\mathrm{Tr}\left[\frac{1}{2}\Big(A^h_{t\mu}A_{t\nu} - A_{t\mu}A^h_{t\nu}\Big)\Big(F_{t\mu\nu} + F^h_{t\mu\nu}\Big) + iA_{t\mu}A^h_{t\nu}A^h_{t\rho}A^h_{t\sigma} + iA^h_{t\mu}A_{t\nu}A_{t\rho}A_{t\sigma} + \frac{i}{2}A^h_{t\mu}A_{t\nu}A^h_{t\rho}A_{t\sigma}\right] \tag{B-4}$$

Above we have defined A^h to be the restriction of A to Lie(H), F^h to be the field strength tensor formed from A^h, and T_a to be a group generator normalized so that $\mathrm{Tr}(T_a T_b) = \delta_{ab}$. In the case of chiral symmetry breaking models it is convenient to write

$$T = \begin{pmatrix} t_1 & 0 \\ 0 & t_2 \end{pmatrix} \tag{B-5}$$

where t_1 and t_2 are elements of the Lie algebra transforming left handed Weyl spinors under the two product groups.

B.2 Parity in models with chiral symmetry

In this paper we are interested in the case of chiral symmetry breaking where one Weyl fermion transforms in the N of an SU(N) and the other transforms in the $\bar{N}$. The appropriate generators in this case are

$$T^V = \begin{pmatrix} t & 0 \\ 0 & -t^* \end{pmatrix},\ T^A = \begin{pmatrix} t & 0 \\ 0 & t^* \end{pmatrix} \tag{B-6}$$

for vector and axial generators, respectively. Consider the parity on these generators that takes

$$T^V \rightarrow T^V,\ T^A \rightarrow -T^A \tag{B-7}$$

The WZW term of a chiral symmetry breaking model is odd under this parity. To show this, take all the terms in $\mathcal{L}_{\mathrm{WZW}}$ and divide them into parity even and odd parts. First consider the terms in G_a from eqn. B-3. Here the generator T_a is in $\mathrm{Lie}\, K$, so the remaining generators must contain an odd number of T^A for a given term to be of even parity. If one makes use of this, combined with the hermiticity of the lie algebra generators, the cyclic properties of the trace, and the antisymmetry of the epsilon symbol one can show that the even terms in G_a vanish for models of chiral symmetry breaking. The proof that Eq. B-4 is odd under this parity proceeds in exactly the same way.

Appendix C

Effective Jet Radii

It is important for jet algorithms to be infrared/collinear safe, since this ensures insensitivity to detector effects and is necessary for meaningful higher order calculations [145]. Since variable R algorithms are extensions of the jet parameterization from Eq. (7.2), it is easy to check that they inherit infrared/collinear safety from standard recursive jet algorithms. However, the purpose of variable R algorithms is to define jets with an effective radius R_{eff}, and infrared/collinear safety alone is insufficient to guarantee a reasonable notion of jet radius. Therefore, we will impose a stronger condition, requiring our algorithms to be "collinear robust".

We focus our attention on jet algorithms with $n \leq 0$, because these algorithms allow for an intuitive definition of an effective jet radius. To talk about an effective jet radius (as opposed to simply a characteristic jet size), the jets must be approximately circular, and the only way to achieve this with a sequential recombination algorithm is to start with a central core and add on to it. This is achieved for $n \leq 0$ because clustering begins with the hardest transverse momentum.[1] The k_T algorithm does not satisfy this condition, since the algorithm clusters from soft objects to hard ones, and the final shape of a k_T jet is only determined in the last few stages of clustering.

---

[1] For the marginal case where $n = 0$ (so clustering is by angle), this still works because the hard center of a jet sees a high concentration of radiation at small angular separation. Strictly speaking, though, jets formed with $n = 0$ will have irregular borders.

As a result, k_T jets assume non-circular shapes, and the notion of an effective radius is obscured.

Said another way, the R_0 parameter plays a very different role in the k_T and the anti-k_T jet algorithms. While R_0 does control the effective size of a jet in both cases, in the k_T algorithm R_0 determines whether a *soft* object should be merged with surrounding radiation, whereas in anti-k_T, R_0 determines whether a *hard* object should be merged with surrounding radiation. In extending R_0 to $R_{\text{eff}}(p_T)$, we wish the R_{eff} size to determine the characteristic radius of a jet based on the p_T of the hard central core.

It is useful to consider three degrees of collinear robustness. The weakest of these demands that the clustering of two four-momenta is controlled by the effective jet radius of the one with harder p_T. This ensures that the hardest jets in an event have well-defined jet radii, and non-circular effects only appear at lower p_T. Consider two four-vectors i and j, with $p_{Ti} > p_{Tj}$. For these two four-vectors to be clustered together, they must satisfy both $d_{ij} < d_{iB}$ and $d_{ij} < d_{jB}$. For $n \leq 0$, the first inequality yields

$$\frac{d_{ij}}{d_{iB}} = \frac{R_{ij}^2}{R_{\text{eff}}(p_{Ti})} < 1, \tag{B-1}$$

and R_{eff} defines an effective radius as desired. To make sure that the second inequality does not affect the clustering and ruin the interpretation of an effective radius, we require $d_{iB} \leq d_{jB}$, which implies

$$p_{Ti}^n R_{\text{eff}}(p_{Ti}) \leq p_{Tj}^n R_{\text{eff}}(p_{Tj}). \tag{B-2}$$

This is the requirement for a minimal degree of collinear robustness, and is satisfied by both the fixed cone and VR ($R \propto 1/p_T$) algorithms.

A stronger version of collinear robustness is that the jet algorithm should be insensitive the resolution of the calorimeter. Even if Eq. (B-2) is satisfied, it is possible for the jets formed with a fine calorimeter resolution to be different from the jets formed with a coarser resolution. This can happen, for example, when $n = -1$ and $R_{\text{eff}} \propto p_T$, where the effective jet radius can become comparable to the calorimeter resolution, and a coarse calorimeter can form a single jet out of two four-momenta that would not otherwise be clustered using R_{eff}. To guard against this pathology, one can impose

$$R_{\text{eff}}(p_T) \gg R_{\text{calorimeter}} \tag{B-3}$$

for all values of p_T. For the VR algorithm, this constraint only applies for very high p_T jets, and in practice is never needed for typical beam energies and calorimeter resolutions.

The strongest version of collinear robustness requires that a jet algorithm should be insensitive to *macroscopic* splittings within the jet radius. This ensures that reasonable rearrangements of a jet's substructure do not cause the jet to be reconstructed differently.[2] This requires that two four-vectors p_i and p_j should be clustered together if they lie with the effective radius defined by the *sum* four-vector $p_i + p_j$. Again assuming that $p_{Ti} > p_{Tj}$, the desired condition is that $d_{ij} < d_{iB}$ whenever $R_{ij} < R_{\text{eff}}(p_{T(i+j)})$, which implies a "shrinking cone" requirement

$$R_{\text{eff}}(p_{Ti}) \geq R_{\text{eff}}(p_{T(i+j)}). \tag{B-4}$$

This is satisfied by the VR (and fixed cone) algorithms, since $R_{\text{eff}}(p_T)$ is monotonically decreasing (or constant) as p_T increases. Note that Eq. (B-4) implies both Eq. (B-3) and Eq. (B-2).

We emphasize that these requirements of collinear robustness are not necessary for the theoretical consistency of the variable R algorithms. From the point of view of perturbative infrared/collinear safety, there is no singularity associated with finite

---

[2] By "reasonable rearrangement", we have in mind situations where an input four-momenta is broken down into smaller pieces within the original effective jet radius.

angle splittings. However, without some version of collinear robustness, the effective jet radii would be difficult to understand, since the jet algorithm would be overly sensitive to the precise four-vectors used in the reconstruction. The shrinking cone requirement of Eq. (B-4) is the conceptually simplest way to enforce collinear robustness, since it does not require defining an $R_{\text{calorimeter}}$ and is independent of the precise choice of n.

Appendix D

Valid VR Parameter Range

Here we discuss the operational range of the jet algorithms discussed in Section 7.2.3. We are interested in the range of ρ for which the VR algorithms will correctly reflect the true jet shape. Note that the following results are only for guidance in choosing the value of ρ, and not a strict set of rules.

In deriving the VR algorithms, we made use of the fact that for approximately massless four vectors, distances in ΔS were linearly related to distances in ΔR via

$$\Delta R \approx \Delta S \cosh \eta. \tag{B-1}$$

Recalling the definition of pseudorapidity η in terms of the polar angle θ

$$\cosh \eta = \frac{1}{\sin \theta}, \qquad \left| \frac{d\theta}{d\eta} \right| = \sin \theta, \tag{B-2}$$

it is easy to see that locally,

$$dS^2 \equiv d\theta^2 + \sin^2 \theta \, d\phi^2 = \sin^2 \theta \, (d\eta^2 + d\phi^2) = \sin^2 \theta \, dR^2. \tag{B-3}$$

which is equivalent to Eq. (B-1).

The approximation in Eq. (B-1) is valid as long as

$$\left|\frac{d\theta}{d\eta}\right| \gtrsim \frac{1}{2}\Delta\eta\left|\frac{d^2\theta}{d\eta^2}\right|, \tag{B-4}$$

which conservatively implies (taking $\Delta\phi \to 0$)

$$\Delta R \lesssim 2\left|\frac{d\theta}{d\eta}\right| \Big/ \left|\frac{d^2\theta}{d\eta^2}\right| = \frac{2}{\cos\theta}. \tag{B-5}$$

For the VR variants we are considering with $R = \rho/p_T$, distortions in the jet shape in going from ΔS to ΔR will be sufficiently small when

$$\rho \lesssim \frac{2p_T}{\cos\theta}. \tag{B-6}$$

As a general rule of thumb then, we expect the VR algorithms to correctly reproduce the size of jets as long as $\rho \lesssim 2p_T$ for most events reconstructed. Because one must use a cutoff on R_{eff} to remove spuriously large cones, events which violate this condition are not necessarily grossly incorrect; they will be reconstructed as if by the CA or AKT algorithms working with $R_{\max}$.

Appendix E

Angular Distributions in Decays of Polarized Tops

Here we collect some results on the energy and angular distributions of daughter partons in polarized top decay. To arrive at these results we assume the standard model top decay $t \to Wb$ with subsequent W decay $W \to \bar{d}u$, and work at leading order in the narrow width approximation for both t and W. Then, the squared matrix element for a polarized top can be written

$$|\mathcal{M}|^2 \propto (t_\pm \cdot d)(b \cdot u) \tag{B-1}$$

where d, b, and u denote the momentum four-vectors of the respective partons, and $t_\pm \equiv p_t \pm m_t S$ contains information about the top polarization through the spin four-vector S. In the top rest frame, the spin four-vector takes the form $S^\mu = (0, \hat{s})$, where $\hat{s}$ is a unit vector defining the axis of polarization. In the narrow width approximation, and further taking $m_b = 0$, the energy of the b quark is fixed at $E_b = (m_t^2 - m_W^2)/2m_t$ in the top rest frame. The full differential decay rate then depends nontrivially on two quantities, which we can take to be the down-quark energy in the top rest frame, E_d and the angle of the down quark with respect to the top spin axis, $\cos\theta_d$. The

Parton	b	W	d	u	j
κ	-0.4	0.4	1.0	-0.3	0.5

Table E.1: Tree level values for the spin analyzing power κ of various top daughters in top decay. The object j is defined in the text.

differential decay rate can be written

$$\frac{1}{\Gamma}\frac{d\Gamma}{dE_d d\cos\theta_d} = \frac{12m_t^3}{m_t^6 + 2m_W^6 - 3m_W^4 m_t^2}\, E_d(m_t - 2E_d)(1 + \mathcal{P}_t \cos\theta_d) \tag{B-2}$$

where $\mathcal{P}_t$ is the top polarization, $-1 \leq \mathcal{P}_t \leq 1$ with $\mathcal{P}_t = 1, -1$ corresponding to right and left handed tops, respectively.

These results can be generalized to study the angular distribution of any given daughter parton i in the top rest frame by writing [146]

$$\frac{1}{\Gamma}\frac{d\Gamma}{d\cos\theta_i} = \frac{1}{2}(1 + \mathcal{P}_t \kappa_i \cos\theta_i), \tag{B-3}$$

where κ_i is the *spin analyzing power* of the parton i, and $\cos\theta_i$ is the angle that parton makes with respect to the top spin axis in the top rest frame. The values of κ_i for various choices of i are listed in Tab. E.1. The d, which corresponds to the lepton in leptonic top decays, is maximally correlated with the top spin, with $\kappa_d = 1$. In addition to the partonic b, W, u, and d, we also consider an object j, defined to be the softer of the two light quark jets in the top rest frame. As the d tends to be softer than the u in the top rest frame, this jet is the d-jet approximately 60% of the time [147, 148].

Appendix F

Scattering Amplitudes for Longitudinal Gauge Bosons and Partial Wave Unitarity

For completeness, we will here review the high energy behavior of longitudinal gauge boson scattering. This will demonstrate why we expect the increase in the scattering amplitudes for non-SM Higgs couplings. It will also help us establish the partial wave unitarity bound for longitudinal gauge boson scattering, which is of practical importance for our simulation. We will make use of the Goldstone equivalence theorem, which says that the scattering behavior of the longitudinal gauge bosons is the same as that of the eaten Goldstones, up to corrections of order $\mathcal{O}(m_W/E)$. Note that while we will only explicitly calculate the behavior of $W_L^+W_L^- \to W_L^+W_L^-$, the other longitudinal gauge boson scattering processes are similar.

We begin with the Lagrangian for the SM Higgs doublet with the additional dimension-6 operator we wish to study:

$$\mathcal{L} = \frac{1}{4}\operatorname{Tr}\left(\partial\mathcal{H}^\dagger\partial\mathcal{H} + \mu^2\mathcal{H}^\dagger\mathcal{H}\right) - \frac{\lambda}{16}\operatorname{Tr}\left(\mathcal{H}^\dagger\mathcal{H}\right)^2 + \frac{c_H}{32f^2}\left[\partial\operatorname{Tr}\left(\mathcal{H}^\dagger\mathcal{H}\right)\partial\operatorname{Tr}\left(\mathcal{H}^\dagger\mathcal{H}\right)\right] \tag{B-1}$$

where $\mathcal{H} = \phi\cdot\sigma$ for real fields ϕ_i ($i = 0 \leftrightarrow 3$) and $\sigma = (1, \vec{\sigma})$. The SM Higgs potential corresponds to $c_H = 0$. Expanding around the minima $\langle\phi_0\rangle = \mu/\sqrt{\lambda}$ one finds new derivative interactions proportional to c_H. Those relevant to $\phi_+\phi_- \to \phi_+\phi_-$ scattering at lowest order are:

$$\mathcal{L} \supset -v\lambda h\phi_+\phi_- - \frac{\lambda}{2}\phi_+^2\phi_-^2 + \frac{c_H}{2f^2}\left(\phi_+^2(\partial\phi_-)^2 + \phi_+\phi_-\partial\phi_+\partial\phi_- + 2v\phi_+\partial\phi_-\partial h\right) + \text{h.c.} \tag{B-2}$$

where we have denoted the shifted ϕ_0 field by h and written $\phi_{1,2}$ in terms of their charge eigenstates $\phi_\pm$. Also, note that there is an additional kinetic term for h:

$$\mathcal{L} \supset \frac{c_H v^2}{2f^2}(\partial h)^2 \tag{B-3}$$

so that in going to canonical normalization we must insert a factor of $N = 1/\sqrt{1 + c_H v^2/f^2}$ for every h encountered at a vertex. The tree level amplitude becomes

$$\mathcal{M}(\phi_+\phi_- \to \phi_+\phi_-) = -4i\lambda + i\frac{c_H}{f^2}s - \frac{iN^2}{(s - m_h^2)}\left(2\lambda v + \frac{c_H v}{2f^2}s\right)^2 + (s \leftrightarrow t) \tag{B-4}$$

where $m_h = \sqrt{2\lambda}v$. Working in the limit $s, t \gg m_h^2$ we find

$$\mathcal{M}(\phi_+\phi_- \to \phi_+\phi_-) \approx i\frac{c_H}{f^2}\left(1 - N^2\frac{c_H v^2}{4f^2}\right)(s + t) \tag{B-5}$$

which shows the E^2 growth in the amplitude that we expect. In this limit, the $J = 0$

partial wave is:

$$a_0 = \frac{1}{16\pi s}\int_{-s}^{0}\frac{c_H}{f^2}\left(1 - N^2\frac{c_H v^2}{4f^2}\right)(s+t)\,dt = \frac{c_H s}{32\pi f^2}\left(1 - N^2\frac{c_H v^2}{4f^2}\right) \tag{B-6}$$

Partial wave unitarity is violated when $|\mathrm{Re}(a_I)| \geq 1/2$, so the unitarity bound is saturated when

$$s_{\max} = \frac{16\pi v^2}{c_H\xi\left(1 - c_H\xi N^2/4\right)} \tag{B-7}$$

To stay clear of this limit, we limit ourselves to studying events for which $s \leq 2$ TeV (corresponding to $|c_H\xi| \leq 0.6$).

We note that one may gain further intuition into the longitudinal gauge boson system by considering the parameterization

$$\mathcal{H} = (v+h)\,e^{i\vec{\pi}\cdot\vec{\sigma}/v} \tag{B-8}$$

Here we have shifted our field definitions so that the π transform non-linearly. In this language, the relevant terms in the Lagrangian become

$$\mathcal{L} \supset \frac{\sqrt{\lambda}}{\mu}h\partial\pi_+\partial\pi_- + \frac{\lambda}{6\mu^2}\left(\pi_+^2(\partial\pi_-)^2 - \pi_+\pi_-\partial\pi_+\partial\pi_-\right) + \text{h.c.} \tag{B-9}$$

As before, the kinetic term of h is shifted, so we must add a factor of N at every point we encounter an h at a vertex. Note, however, that in this case all of the operators come with $\partial\pi$ terms. Computed in this way, the amplitude $\mathcal{M}(\pi_+\pi_- \to \pi_+\pi_-)$ shows the same behavior as Eq. (B-4), as it must, but this is the result of a *non-cancelation* of derivatives between the four-point operator and the h-exchange in the t & s-channels, rather than because of a new vertex.

Using these results we can compare the scattering in the Higgsless case to that of the case where the Higgs has anomalous couplings. To consider the Higgsless case we set $c_H = 0$ in Eq. (B-4) and consider the $\sqrt{s} \ll m_h$ limit using $m_h = \sqrt{2\lambda}v$. We find

$$\sigma_{\text{no-higgs}} \propto |\mathcal{M}|^2 = \frac{4}{v^4}(s+t)^2 \tag{B-10}$$

wheras for the case of a light Higgs with anomalous couplings we find from Eq. (B-5)

$$\sigma_{\text{anom-higgs}} \propto |\mathcal{M}|^2 = \frac{(c_H \xi)^2}{v^4}(s+t)^2 \tag{B-11}$$

under the assumption

$$\frac{c_H \xi}{2} \gg \frac{m_h^2}{s} \tag{B-12}$$

This is how we arrived at Eq. (4.3). For $m_h \sim 100$ GeV this is true for scattering at the TeV scale as long as $c_H \xi \gtrsim 1/10$. At lower values of the anomalous coupling the dominant effect comes from interference effects proportional to $s+t$ instead of $(s+t)^2$. Thus smaller values of the anomalous couplings have a qualitatively different energy behavior that of larger values, making them especially difficult to resolve.

Appendix G

Overview of Jet Algorithms

While a comprehensive review of jet algorithms is beyond the scope of this work (see [125] for a recent review), here we will provide a short overview so the reader can quickly gain intuition into subjet techniques.

Jet algorithms can roughly be divided into two categories: cone algorithms, which function as cookie-cutters to stamp out jets from calorimeter cells, and sequential recombination algorithms, which build up a jet by merging four-momenta one by one in a prescribed order. Here we will focus on recombination algorithms.

Each of these algorithms functions by defining a distance measure between every pair of four-momenta and for each four-momenta individually:

$$d_{ij} = \min(p_{Ti}^{2n}, p_{Tj}^{2n}) \left(\frac{R_{ij}}{R_0}\right)^2, \; d_{iB} = p_{Tj}^{2n} \tag{B-1}$$

for jets i and j. If the smallest distance measure at a given stage in clustering is between two four-momenta they are merged, otherwise the four-momenta with the smallest d_{iB} is declared a jet and removed from the queue.

The different sequential recombination algorithms are distinguished by value of n appearing in Eq. (B-1). These values determine the clustering order, whether one clusters beginning with hard four-momenta, soft four-momenta, or by angle (see

Algortithm	n	Approximate clustering order
k_T	1	soft→ hard
C/A	0	near→far (in y-ϕ)
anti-k_T	-1	hard→ soft

Table G.1: Parameterization and approximate behavior of sequential recombination jet algorithms.

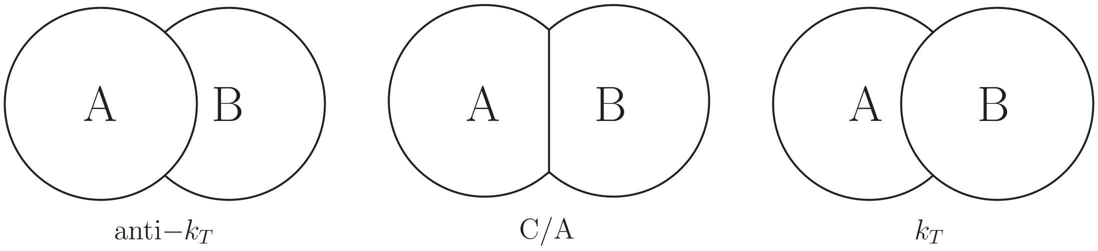

Figure G.1: Approximate clustering behavior of jets for the different sequential recombination algorithms assuming $p_T^A > p_T^B$. Note that while we have shown the jets as being circular, the k_T jets can behave in a non-circular, wandering way.

Table G.1 and Fig. G.1). For the subjet analysis at hand, where reconstructing the softer subjet is essential, we therefore use the k_T algorithm which begins by clustering softer jets, preventing them from being cannibalized by the harder subjet.

Appendix H

Gauge Mediation in a Model of Dark Matter

In this scenario we have studied, the singlet S sees SUSY-breaking from the SM and couples to Ψ/Ψ_c. Therefore, in analogy to scenarios of gauge-mediation, S can be thought of as a SUSY-breaking sprurion and Ψ/Ψ_c a messenger multiplet. One finds that the dark gauge group will mediate SUSY-breaking to all states charged under the it, inducing a soft mass for the scalars and for the dark gaugino.

One finds [149] that the dark Higgses see a soft mass

$$m^2 \approx 4M_s^2 \left(\frac{g_d^2}{16\pi^2}\right)^2 = \frac{\alpha_d^2}{4\pi^2} M_s^2 \tag{B-1}$$

and the gaugino mass term becomes

$$M \approx \frac{g_d^2}{8\pi^2} M_s = 2\alpha_d M_s, \tag{B-2}$$

where

$$M_s = \left|\frac{\langle F_S\rangle}{\langle S\rangle}\right|. \tag{B-3}$$

Bibliography

[1] Pliny the Elder, *The Natural History.* Taylor and Francis, Red Lion Court, Fleet Street, London, 1855.

[2] D. Krohn and I. Yavin, *Anomalies in Fermionic UV Completions of Little Higgs Models*, *JHEP* **06** (2008) 092, [`0803.4202`].

[3] T. Han, D. Krohn, L.-T. Wang, and W. Zhu, *New Physics Signals in Longitudinal Gauge Boson Scattering at the LHC*, *JHEP* **03** (2010) 082, [`0911.3656`].

[4] D. Krohn, J. Shelton, and L.-T. Wang, *Measuring the Polarization of Boosted Hadronic Tops*, `0909.3855`.

[5] D. Krohn, J. Thaler, and L.-T. Wang, *Jet Trimming*, *JHEP* **02** (2010) 084, [`0912.1342`].

[6] D. Krohn, J. Thaler, and L.-T. Wang, *Jets with Variable R*, *JHEP* **06** (2009) 059, [`0903.0392`].

[7] S. L. Glashow, *Partial Symmetries of Weak Interactions*, *Nucl. Phys.* **22** (1961) 579–588.

[8] S. Weinberg, *A Model of Leptons*, *Phys. Rev. Lett.* **19** (1967) 1264–1266.

[9] A. Salam and J. C. Ward, *Electromagnetic and weak interactions*, *Phys. Lett.* **13** (1964) 168–171.

[10] F. Englert and R. Brout, *Broken Symmetry and the Mass of Gauge Vector Mesons*, *Phys. Rev. Lett.* **13** (1964) 321–322.

[11] P. W. Higgs, *Broken symmetries, massless particles and gauge fields*, *Phys. Lett.* **12** (1964) 132–133.

[12] G. S. Guralnik, C. R. Hagen, and T. W. B. Kibble, *Global Conservation Laws and Massless Particles*, *Phys. Rev. Lett.* **13** (1964) 585–587.

[13] **Super-Kamiokande** Collaboration, Y. Fukuda *et al.*, *Evidence for oscillation of atmospheric neutrinos*, *Phys. Rev. Lett.* **81** (1998) 1562–1567, [`hep-ex/9807003`].

[14] **Particle Data Group** Collaboration, S. Eidelman *et al.*, *Review of particle physics*, *Phys. Lett.* **B592** (2004) 1.

[15] S. Dimopoulos and H. Georgi, *Softly Broken Supersymmetry and SU(5)*, *Nucl. Phys.* **B193** (1981) 150.

[16] S. Weinberg, *Approximate symmetries and pseudoGoldstone bosons*, *Phys. Rev. Lett.* **29** (1972) 1698–1701.

[17] H. Georgi and A. Pais, *Vacuum Symmetry and the PseudoGoldstone Phenomenon*, *Phys. Rev.* **D12** (1975) 508.

[18] H. Georgi and A. Pais, *Calculability and Naturalness in Gauge Theories*, *Phys. Rev.* **D10** (1974) 539.

[19] S. Weinberg, *Implications of Dynamical Symmetry Breaking*, *Phys. Rev.* **D13** (1976) 974–996.

[20] L. Susskind, *Dynamics of Spontaneous Symmetry Breaking in the Weinberg-Salam Theory*, *Phys. Rev.* **D20** (1979) 2619–2625.

[21] W. Buchmuller and D. Wyler, *Effective Lagrangian Analysis of New Interactions and Flavor Conservation*, *Nucl. Phys.* **B268** (1986) 621.

[22] R. Barbieri and A. Strumia, *What is the limit on the Higgs mass?*, *Phys. Lett.* **B462** (1999) 144–149, [`hep-ph/9905281`].

[23] N. Arkani-Hamed, A. G. Cohen, and H. Georgi, *Electroweak symmetry breaking from dimensional deconstruction*, *Phys. Lett.* **B513** (2001) 232–240, [`hep-ph/0105239`].

[24] N. Arkani-Hamed, A. G. Cohen, and H. Georgi, *(De)constructing dimensions*, *Phys. Rev. Lett.* **86** (2001) 4757–4761, [`hep-th/0104005`].

[25] D. Tucker-Smith and N. Weiner, *Inelastic dark matter*, *Phys. Rev.* **D64** (2001) 043502, [`hep-ph/0101138`].

[26] S. Chang, G. D. Kribs, D. Tucker-Smith, and N. Weiner, *Inelastic Dark Matter in Light of DAMA/LIBRA*, *Phys. Rev.* **D79** (2009) 043513, [`0807.2250`].

[27] N. Arkani-Hamed, D. P. Finkbeiner, T. R. Slatyer, and N. Weiner, *A Theory of Dark Matter*, *Phys. Rev.* **D79** (2009) 015014, [`0810.0713`].

[28] N. Arkani-Hamed and N. Weiner, *LHC Signals for a SuperUnified Theory of Dark Matter*, *JHEP* **12** (2008) 104, [`0810.0714`].

[29] H.-C. Cheng and I. Low, *Little hierarchy, little Higgses, and a little symmetry*, *JHEP* **08** (2004) 061, [`hep-ph/0405243`].

[30] H.-C. Cheng and I. Low, *TeV symmetry and the little hierarchy problem*, *JHEP* **09** (2003) 051, [`hep-ph/0308199`].

[31] C. T. Hill and R. J. Hill, *T-parity violation by anomalies*, *Phys. Rev.* **D76** (2007) 115014, [`arXiv:0705.0697 [hep-ph]`].

[32] C. T. Hill and R. J. Hill, *Topological Physics of Little Higgs Bosons*, *Phys. Rev.* **D75** (2007) 115009, [`hep-ph/0701044`].

[33] J. Wess and B. Zumino, *Consequences of anomalous Ward identities*, *Phys. Lett.* **B37** (1971) 95.

[34] E. Witten, *Global Aspects of Current Algebra*, *Nucl. Phys.* **B223** (1983) 422–432.

[35] N. Arkani-Hamed *et al.*, *The minimal moose for a little Higgs*, *JHEP* **08** (2002) 021, [`hep-ph/0206020`].

[36] C. Csaki, J. Heinonen, M. Perelstein, and C. Spethmann, *A Weakly Coupled Ultraviolet Completion of the Littlest Higgs with T-parity*, `0804.0622`.

[37] S. Chang and J. G. Wacker, *Little Higgs and custodial SU(2)*, *Phys. Rev.* **D69** (2004) 035002, [`hep-ph/0303001`].

[38] H.-C. Cheng, J. Thaler, and L.-T. Wang, *Little M-theory*, *JHEP* **09** (2006) 003, [`hep-ph/0607205`].

[39] P. Batra and Z. Chacko, *Symmetry Breaking Patterns for the Little Higgs from Strong Dynamics*, `arXiv:0710.0333 [hep-ph]`.

[40] J. Preskill and S. Weinberg, *'Decoupling' Constraints on Massless Composite Particles*, *Phys. Rev.* **D24** (1981) 1059.

[41] B. Holdom, *Raising the Sideways Scale*, *Phys. Rev.* **D24** (1981) 1441.

[42] K. Lane, *A case study in dimensional deconstruction*, *Phys. Rev.* **D65** (2002) 115001, [`hep-ph/0202093`].

[43] T. Gregoire and J. G. Wacker, *Deconstructing six dimensional gauge theories with strongly coupled moose meshes*, `hep-ph/0207164`.

[44] N. Arkani-Hamed, A. G. Cohen, E. Katz, and A. E. Nelson, *The littlest Higgs*, *JHEP* **07** (2002) 034, [`hep-ph/0206021`].

[45] C.-S. Chu, P.-M. Ho, and B. Zumino, *Non-Abelian Anomalies and Effective Actions for a Homogeneous Space G/H*, *Nucl. Phys.* **B475** (1996) 484–504, [`hep-th/9602093`].

[46] G. Jungman, M. Kamionkowski, and K. Griest, *Supersymmetric dark matter*, *Phys. Rept.* **267** (1996) 195–373, [`hep-ph/9506380`].

[47] G. Bertone, D. Hooper, and J. Silk, *Particle dark matter: Evidence, candidates and constraints*, *Phys. Rept.* **405** (2005) 279–390, [`hep-ph/0404175`].

[48] D. P. Finkbeiner and N. Weiner, *Exciting Dark Matter and the INTEGRAL/SPI 511 keV signal*, *Phys. Rev.* **D76** (2007) 083519, [`astro-ph/0702587`].

[49] M. Pospelov and A. Ritz, *Astrophysical Signatures of Secluded Dark Matter*, *Phys. Lett.* **B671** (2009) 391–397, [`0810.1502`].

[50] M. Baumgart, C. Cheung, J. T. Ruderman, L.-T. Wang, and I. Yavin, *Non-Abelian Dark Sectors and Their Collider Signatures*, *JHEP* **04** (2009) 014, [`0901.0283`].

[51] C. Cheung, J. T. Ruderman, L.-T. Wang, and I. Yavin, *Kinetic Mixing as the Origin of Light Dark Scales*, *Phys. Rev.* **D80** (2009) 035008, [`0902.3246`].

[52] J. Fan, J. Thaler, and L.-T. Wang, *Dark matter from dynamical SUSY breaking*, `1004.0008`.

[53] Y. Nomura and J. Thaler, *Dark Matter through the Axion Portal*, *Phys. Rev.* **D79** (2009) 075008, [`0810.5397`].

[54] C. P. Burgess, M. Pospelov, and T. ter Veldhuis, *The minimal model of nonbaryonic dark matter: A singlet scalar*, *Nucl. Phys.* **B619** (2001) 709–728, [`hep-ph/0011335`].

[55] J. March-Russell, S. M. West, D. Cumberbatch, and D. Hooper, *Heavy Dark Matter Through the Higgs Portal*, *JHEP* **07** (2008) 058, [`0801.3440`].

[56] C. Arina, F.-X. Josse-Michaux, and N. Sahu, *A Tight Connection Between Direct and Indirect Detection of Dark Matter through Higgs Portal Couplings to a Hidden Sector*, `1004.3953`.

[57] M. Farina, D. Pappadopulo, and A. Strumia, *CDMS stands for Constrained Dark Matter Singlet*, `0912.5038`.

[58] H. P. Nilles, M. Srednicki, and D. Wyler, *Weak Interaction Breakdown Induced by Supergravity*, *Phys. Lett.* **B120** (1983) 346.

[59] J. M. Frere, D. R. T. Jones, and S. Raby, *Fermion Masses and Induction of the Weak Scale by Supergravity*, *Nucl. Phys.* **B222** (1983) 11.

[60] J. P. Derendinger and C. A. Savoy, *Quantum Effects and SU(2) x U(1) Breaking in Supergravity Gauge Theories*, *Nucl. Phys.* **B237** (1984) 307.

[61] B. A. Dobrescu, G. L. Landsberg, and K. T. Matchev, *Higgs boson decays to CP-odd scalars at the Tevatron and beyond*, *Phys. Rev.* **D63** (2001) 075003, [`hep-ph/0005308`].

[62] B. A. Dobrescu and K. T. Matchev, *Light axion within the next-to-minimal supersymmetric standard model*, *JHEP* **09** (2000) 031, [`hep-ph/0008192`].

[63] R. Dermisek and J. F. Gunion, *Escaping the large fine tuning and little hierarchy problems in the next to minimal supersymmetric model and h -¿ a a decays*, *Phys. Rev. Lett.* **95** (2005) 041801, [`hep-ph/0502105`].

[64] R. Dermisek and J. F. Gunion, *Consistency of LEP event excesses with an h –¿ a a decay scenario and low-fine-tuning NMSSM models*, *Phys. Rev.* **D73** (2006) 111701, [`hep-ph/0510322`].

[65] S. Chang, P. J. Fox, and N. Weiner, *Naturalness and Higgs decays in the MSSM with a singlet*, *JHEP* **08** (2006) 068, [`hep-ph/0511250`].

[66] R. Barbieri, L. J. Hall, A. Y. Papaioannou, D. Pappadopulo, and V. S. Rychkov, *An alternative NMSSM phenomenology with manifest perturbative unification*, *JHEP* **03** (2008) 005, [`0712.2903`].

[67] L. J. Hall and T. Watari, *Electroweak supersymmetry with an approximate U(1)(PQ)*, *Phys. Rev.* **D70** (2004) 115001, [`hep-ph/0405109`].

[68] D. J. Miller, S. Moretti, and R. Nevzorov, *Higgs bosons in the NMSSM with exact and slightly broken PQ-symmetry*, `hep-ph/0501139`.

[69] J. D. Lewin and P. F. Smith, *Review of mathematics, numerical factors, and corrections for dark matter experiments based on elastic nuclear recoil*, *Astropart. Phys.* **6** (1996) 87–112.

[70] R. H. Helm, *Inelastic and Elastic Scattering of 187-Mev Electrons from Selected Even-Even Nuclei*, *Phys. Rev.* **104** (1956) 1466–1475.

[71] C. Savage, K. Freese, and P. Gondolo, *Annual Modulation of Dark Matter in the Presence of Streams*, *Phys. Rev.* **D74** (2006) 043531, [`astro-ph/0607121`].

[72] J. Giedt, A. W. Thomas, and R. D. Young, *Dark matter, the CMSSM and lattice QCD*, *Phys. Rev. Lett.* **103** (2009) 201802, [`0907.4177`].

[73] *Precision electroweak measurements on the Z resonance*, *Phys. Rept.* **427** (2006) 257, [`hep-ex/0509008`]. The **ALEPH** Collaboration, the **DELPHI** Collaboration, the **L3** Collaboration, the **OPAL** Collaboration, the **SLD**

Collaboration, the **LEP** Electroweak Working Group, the **SLD** electroweak, heavy flavour groups.

[74] R. Barbieri, A. Pomarol, R. Rattazzi, and A. Strumia, *Electroweak symmetry breaking after LEP-1 and LEP-2*, *Nucl. Phys.* **B703** (2004) 127–146, [`hep-ph/0405040`].

[75] R. Contino, Y. Nomura, and A. Pomarol, *Higgs as a holographic pseudo-Goldstone boson*, *Nucl. Phys.* **B671** (2003) 148–174, [`hep-ph/0306259`].

[76] C. N. Leung, S. T. Love, and S. Rao, *Low-Energy Manifestations of a New Interaction Scale: Operator Analysis*, *Z. Phys.* **C31** (1986) 433.

[77] J. Wudka, *Electroweak effective Lagrangians*, *Int. J. Mod. Phys.* **A9** (1994) 2301–2362, [`hep-ph/9406205`].

[78] K. Hagiwara, S. Ishihara, R. Szalapski, and D. Zeppenfeld, *Low-energy constraints on electroweak three gauge boson couplings*, *Phys. Lett.* **B283** (1992) 353–359.

[79] K. Hagiwara, S. Ishihara, R. Szalapski, and D. Zeppenfeld, *Low-energy effects of new interactions in the electroweak boson sector*, *Phys. Rev.* **D48** (1993) 2182–2203.

[80] **Particle Data Group** Collaboration, K. Hagiwara *et al.*, *Review of particle physics*, *Phys. Rev.* **D66** (2002) 010001.

[81] V. Barger, T. Han, P. Langacker, B. McElrath, and P. Zerwas, *Effects of genuine dimension-six Higgs operators*, *Phys. Rev.* **D67** (2003) 115001, [`hep-ph/0301097`].

[82] G. F. Giudice, C. Grojean, A. Pomarol, and R. Rattazzi, *The Strongly-Interacting Light Higgs*, *JHEP* **06** (2007) 045, [`hep-ph/0703164`].

[83] D. A. Dicus and V. S. Mathur, *Upper bounds on the values of masses in unified gauge theories*, *Phys. Rev.* **D7** (1973) 3111–3114.

[84] B. W. Lee, C. Quigg, and H. B. Thacker, *Weak Interactions at Very High-Energies: The Role of the Higgs Boson Mass*, *Phys. Rev.* **D16** (1977) 1519.

[85] M. J. G. Veltman, *Second Threshold in Weak Interactions*, *Acta Phys. Polon.* **B8** (1977) 475.

[86] M. S. Chanowitz and M. K. Gaillard, *The TeV Physics of Strongly Interacting W's and Z's*, *Nucl. Phys.* **B261** (1985) 379.

[87] I. Low, R. Rattazzi, and A. Vichi, *Theoretical Constraints on the Higgs Effective Couplings*, `0907.5413`.

[88] R. Barbieri, B. Bellazzini, V. S. Rychkov, and A. Varagnolo, *The Higgs boson from an extended symmetry*, *Phys. Rev.* **D76** (2007) 115008, [`0706.0432`].

[89] M. E. Peskin and T. Takeuchi, *A New constraint on a strongly interacting Higgs sector*, *Phys. Rev. Lett.* **65** (1990) 964–967.

[90] J. M. Butterworth, B. E. Cox, and J. R. Forshaw, *W W scattering at the LHC*, *Phys. Rev.* **D65** (2002) 096014, [`hep-ph/0201098`].

[91] S. Catani, Y. L. Dokshitzer, M. H. Seymour, and B. R. Webber, *Longitudinally invariant K(t) clustering algorithms for hadron hadron collisions*, *Nucl. Phys.* **B406** (1993) 187–224.

[92] S. D. Ellis and D. E. Soper, *Successive combination jet algorithm for hadron collisions*, *Phys. Rev.* **D48** (1993) 3160–3166, [`hep-ph/9305266`].

[93] Y. L. Dokshitzer, G. D. Leder, S. Moretti, and B. R. Webber, *Better Jet Clustering Algorithms*, *JHEP* **08** (1997) 001, [`hep-ph/9707323`].

[94] M. Wobisch and T. Wengler, *Hadronization corrections to jet cross sections in deep- inelastic scattering*, `hep-ph/9907280`.

[95] J. M. Butterworth, A. R. Davison, M. Rubin, and G. P. Salam, *Jet substructure as a new Higgs search channel at the LHC*, *Phys. Rev. Lett.* **100** (2008) 242001, [`0802.2470`].

[96] J. Thaler and L.-T. Wang, *Strategies to Identify Boosted Tops*, *JHEP* **07** (2008) 092, [`0806.0023`].

[97] K. Agashe, A. Delgado, M. J. May, and R. Sundrum, *RS1, custodial isospin and precision tests*, *JHEP* **08** (2003) 050, [`hep-ph/0308036`].

[98] G. L. Kane, G. A. Ladinsky, and C. P. Yuan, *Using the top quark for testing standard model polarization and CP predictions*, *Phys. Rev.* **D45** (1992) 124–141.

[99] K. Agashe, A. Belyaev, T. Krupovnickas, G. Perez, and J. Virzi, *LHC signals from warped extra dimensions*, *Phys. Rev.* **D77** (2008) 015003, [`hep-ph/0612015`].

[100] B. Lillie, L. Randall, and L.-T. Wang, *The Bulk RS KK-gluon at the LHC*, *JHEP* **09** (2007) 074, [`hep-ph/0701166`].

[101] V. Barger, T. Han, and D. G. E. Walker, *Top Quark Pairs at High Invariant Mass: A Model- Independent Discriminator of New Physics at the LHC*, *Phys. Rev. Lett.* **100** (2008) 031801, [`hep-ph/0612016`].

[102] A. L. Fitzpatrick, J. Kaplan, L. Randall, and L.-T. Wang, *Searching for the Kaluza-Klein Graviton in Bulk RS Models*, *JHEP* **09** (2007) 013, [`hep-ph/0701150`].

[103] W. Skiba and D. Tucker-Smith, *Using jet mass to discover vector quarks at the LHC*, *Phys. Rev.* **D75** (2007) 115010, [`hep-ph/0701247`].

[104] U. Baur and L. H. Orr, *High p_T Top Quarks at the Large Hadron Collider*, *Phys. Rev.* **D76** (2007) 094012, [`0707.2066`].

[105] R. Frederix and F. Maltoni, *Top pair invariant mass distribution: a window on new physics*, *JHEP* **01** (2009) 047, [`0712.2355`].

[106] U. Baur and L. H. Orr, *Searching for $t\bar{t}$ Resonances at the Large Hadron Collider*, *Phys. Rev.* **D77** (2008) 114001, [`0803.1160`].

[107] D. E. Kaplan, K. Rehermann, M. D. Schwartz, and B. Tweedie, *Top Tagging: A Method for Identifying Boosted Hadronically Decaying Top Quarks*, *Phys. Rev. Lett.* **101** (2008) 142001, [`0806.0848`].

[108] L. G. Almeida *et al.*, *Substructure of high-p_T Jets at the LHC*, `0807.0234`.

[109] L. G. Almeida, S. J. Lee, G. Perez, I. Sung, and J. Virzi, *Top Jets at the LHC*, *Phys. Rev.* **D79** (2009) 074012, [`0810.0934`].

[110] Y. Bai and Z. Han, *Top-antitop and Top-top Resonances in the Dilepton Channel at the CERN LHC*, *JHEP* **04** (2009) 056, [`0809.4487`].

[111] T. C. Collaboration, *A cambridge-aachen (c-a) based jet algorithm for boosted top-jet tagging*, Tech. Rep. CMS PAS JME-09-001, Jul, 2007.

[112] G. Brooijmans, *High p_t hadronic top quark identification*, Tech. Rep. ATL-COM-PHYS-2008-001, ATLAS, Feb, 2008.

[113] S. D. Ellis, C. K. Vermilion, and J. R. Walsh, *Techniques for improved heavy particle searches with jet substructure*, `0903.5081`.

[114] J. Shelton, *Polarized tops from new physics: signals and observables*, *Phys. Rev.* **D79** (2009) 014032, [`0811.0569`].

[115] M. Perelstein and A. Weiler, *Polarized Tops from Stop Decays at the LHC*, *JHEP* **03** (2009) 141, [`0811.1024`].

[116] L. March, E. Ros, and B. Salvacha, *Search for kaluza-klein excitations of the gluon in models with extra dimensions*, Tech. Rep. ATL-PHYS-PUB-2006-002. ATL-COM-PHYS-2005-032, CERN, Geneva, Jul, 2005.

[117] S. Gonzlez de la Hoz, L. March, and E. Ros, *Search for hadronic decays of* z_H *and* w_H *in the little higgs model*, Tech. Rep. ATL-PHYS-PUB-2006-003. ATL-COM-PHYS-2005-001, CERN, Geneva, 2005.

[118] M. Lehmacher, *b-Tagging Algorithms and their Performance at ATLAS*, `0809.4896`.

[119] M. Cacciari, G. Salam, and G. Soyez, "FastJet." http://fastjet.fr/.

[120] F. Maltoni and T. Stelzer, *MadEvent: Automatic event generation with MadGraph*, *JHEP* **02** (2003) 027, [`hep-ph/0208156`].

[121] T. Sjostrand, S. Mrenna, and P. Skands, *PYTHIA 6.4 physics and manual*, *JHEP* **05** (2006) 026, [`hep-ph/0603175`].

[122] M. Bahr *et al.*, *Herwig++ Physics and Manual*, *Eur. Phys. J.* **C58** (2008) 639–707, [`0803.0883`].

[123] M. Cacciari, G. P. Salam, and G. Soyez, *The anti-*k_t *jet clustering algorithm*, *JHEP* **04** (2008) 063, [`0802.1189`].

[124] S. D. Ellis, J. Huston, K. Hatakeyama, P. Loch, and M. Tonnesmann, *Jets in hadron-hadron collisions*, *Prog. Part. Nucl. Phys.* **60** (2008) 484–551, [`0712.2447`].

[125] G. P. Salam, *Towards Jetography*, `0906.1833`.

[126] M. Cacciari, G. P. Salam, and G. Soyez, *The Catchment Area of Jets*, *JHEP* **04** (2008) 005, [`0802.1188`].

[127] M. H. Seymour, *Searches for new particles using cone and cluster jet algorithms: A Comparative study*, *Z. Phys.* **C62** (1994) 127–138.

[128] T. Plehn, G. P. Salam, and M. Spannowsky, *Fat Jets for a Light Higgs*, `0910.5472`.

[129] S. D. Ellis, C. K. Vermilion, and J. R. Walsh, *Recombination Algorithms and Jet Substructure: Pruning as a Tool for Heavy Particle Searches*, `0912.0033`.

[130] J. M. Butterworth, J. R. Ellis, and A. R. Raklev, *Reconstructing sparticle mass spectra using hadronic decays*, *JHEP* **05** (2007) 033, [`hep-ph/0702150`].

[131] J. M. Butterworth, J. R. Ellis, A. R. Raklev, and G. P. Salam, *Discovering baryon-number violating neutralino decays at the LHC*, `0906.0728`.

[132] M. Cacciari, J. Rojo, G. P. Salam, and G. Soyez, *Quantifying the performance of jet definitions for kinematic reconstruction at the LHC*, *JHEP* **12** (2008) 032, [`0810.1304`].

[133] **CDF** Collaboration, R. D. Field, *The underlying event in hard scattering processes*, `hep-ph/0201192`.

[134] **CDF** Collaboration, R. Field and R. C. Group, *PYTHIA tune A, HERWIG, and JIMMY in Run 2 at CDF*, `hep-ph/0510198`.

[135] M. Cacciari and G. P. Salam, *Dispelling the N**3 myth for the k(t) jet-finder*, *Phys. Lett.* **B641** (2006) 57–61, [`hep-ph/0512210`].

[136] B. Andersson, *The Lund model*, *Camb. Monogr. Part. Phys. Nucl. Phys. Cosmol.* **7** (1997) 1–471.

[137] **ALEPH** Collaboration, R. Barate *et al.*, *Studies of quantum chromodynamics with the ALEPH detector*, *Phys. Rept.* **294** (1998) 1–165.

[138] C. K. Vermilion, "FastPrune." http://bit.ly/pruning.

[139] S. Catani, Y. L. Dokshitzer, M. Olsson, G. Turnock, and B. R. Webber, *New clustering algorithm for multi - jet cross-sections in e+ e- annihilation*, *Phys. Lett.* **B269** (1991) 432–438.

[140] G. P. Salam and G. Soyez, *A practical Seedless Infrared-Safe Cone jet algorithm*, *JHEP* **05** (2007) 086, [`0704.0292`].

[141] M. Dasgupta, L. Magnea, and G. P. Salam, *Non-perturbative QCD effects in jets at hadron colliders*, *JHEP* **02** (2008) 055, [`0712.3014`].

[142] E. A. Baltz, M. Battaglia, M. E. Peskin, and T. Wizansky, *Determination of dark matter properties at high-energy colliders*, *Phys. Rev.* **D74** (2006) 103521, [`hep-ph/0602187`].

[143] V. Barger, W.-Y. Keung, and Y. Gao, *T-Anomaly Induced LHC Signals*, *Phys. Lett.* **B655** (2007) 228–235, [`arXiv:0707.3648 [hep-ph]`].

[144] S. Weinberg, *The quantum theory of fields. Vol. 2: Modern applications*, . Cambridge, UK: Univ. Pr. (1996) 489 p.

[145] G. Sterman and S. Weinberg, *Jets from Quantum Chromodynamics*, *Phys. Rev. Lett.* **39** (1977) 1436.

[146] M. Jezabek and J. H. Kuhn, *Lepton Spectra from Heavy Quark Decay*, *Nucl. Phys.* **B320** (1989) 20.

[147] M. Jezabek, *Top quark physics*, *Nucl. Phys. Proc. Suppl.* **37B** (1994) 197, [`hep-ph/9406411`].

[148] A. Brandenburg, Z. G. Si, and P. Uwer, *QCD-corrected spin analysing power of jets in decays of polarized top quarks*, *Phys. Lett.* **B539** (2002) 235–241, [`hep-ph/0205023`].

[149] G. F. Giudice and R. Rattazzi, *Theories with gauge-mediated supersymmetry breaking*, *Phys. Rept.* **322** (1999) 419–499, [`hep-ph/9801271`].